Optimization of magnetic field sources for weakly conducting media in Lorentz force velocimetry

Dissertation
zur Erlangung des akademischen Grades
Doktoringenieur
(Dr.-Ing.)

vorgelegt der
Fakultät für Elektrotechnik und Informationstechnik
Technischen Universität Ilmenau
von
Džulia Terzijska

Datum der Einreichung: 27. November 2015
Datum der wissenschaftlichen Aussprache: 24. Februar 2016

Gutachter:
1. PD Dr.-Ing. habil. Ulrich Lüdtke
2. apl. Prof. Dr.-Ing. habil. Christian Karcher
3. Prof. Dr. Alban Pothérat

urn:nbn:de:gbv:ilm1-2016000446

Erklärung

Ich versichere, dass ich die vorliegende Arbeit ohne unzulässige Hilfe Dritter und ohne Benutzung anderer als der angegebenen Hilfsmittel angefertigt habe. Die aus anderen Quellen direkt oder indirekt übernommenen Daten und Konzepte sind unter Angabe der Quelle gekennzeichnet.

Bei der Auswahl und Auswertung folgenden Materials haben mir die nachstehend aufgeführten Personen in der jeweils beschriebenen Weise unentgeltlich geholfen:

1. Thomas Boeck

Weitere Personen waren an der inhaltlich-materiellen Erstellung der vorliegenden Arbeit nicht beteiligt. Insbesondere habe ich hierfür nicht die entgeltliche Hilfe von Vermittlungs- bzw. Beratungsdiensten (Promotionsberater oder anderer Personen) in Anspruch genommen. Niemand hat von mir unmittelbar oder mittelbar geldwerte Leistungen für Arbeiten erhalten, die im Zusammenhang mit dem Inhalte der vorgelegten Dissertation stehen.

Die Arbeit wurde bisher weder im In- noch im Ausland in gleicher oder ähnlicher Form einer Prüfungsbehörde vorgelegt.

Ich bin darauf hingewiesen worden, dass die Unrichtigkeit der vorstehenden Erklärung als Täuschungsversuch angesehen wird und den erfolglosen Abbruch des Promotionsverfahrens zu Folge hat.

Ilmenau, den 27.11.2015

Dzulia Terzijska

Danksagung

Ich bedanke mich zuallererst bei meinem Betreuer Ulrich Lüdtke, der immer Zeit für mich hatte. Von ihm konnte ich während meiner Promotion viel lernen und mich fachlich und persönlich weiter entwickeln.

Darüber hinaus bedanke ich mich beim ganzen Fachgebiet Elektrowärme und den Kollegen im Haus M, mit denen ich nicht nur während der Arbeitszeit eine schöne Zeit verbracht habe.

Ganz lieben Dank gilt Ninh Tran, Henning Schwanbeck, der sich oft mit meinen PC Problemen rumschlagen musste, Gabriele Eichfelder, die mir geduldig die mathematische Seite der Optimierung erklärt hat, Thomas Boeck, der mich auf die Asymptotische Approximation aufmerksam gemacht hat, Margherita Porcelli und Alban Pothérat, die mich während meiner Auslandsaufenthalte betreut haben.

Zusammenfassung

Diese Arbeit beschreibt die theoretische und numerische Optimierung der neuartigen kontaktlosen Messmethode Lorentzkraftanemometrie (LKA). Die LKA basiert auf der Messung der Lorentzkraft, die auf ein Magnetsystem nahe einem elektrisch leitfähigen Medium wirkt. Flüssigkeiten mit einer niedrigen Leitfähigkeit von einigen S/m stellen eine besondere Herausforderung dar. Hier ist die Lorentzkraft relativ klein verglichen mit Messungen an flüssig Metallen, deren Leitfähigkeit 10^6 Größenordnungen größer ist. Äußere Störungen haben einen viel größeren Einfluss auf die Messungen und es ist unerlässlich die Qualität des Signals für die Anwendung in der Industrie zu verbessern. Eine Möglichkeit dieses Ziel zu erreichen, die Optimierung des Magnetsystems, steht im Focus dieser Arbeit.

Um Kenntnisse in die optimale fundamentale Form des magnetischen Feldes zu erhalten wird ein Aufbau von Dipolen untersucht. Unter bestimmten Bedingungen ist die analytische Lösung dieses Problem möglich. Komplexere Dipolanordnungen werden numerisch mit Simulationssoftware basierend auf der finiten Elemente Methode (FEM) optimiert. Die Orientierung der magnetischen Momente und die Positionen der Dipole gehören zur möglichen Menge der Entscheidungsvariablen. Ihr Einfluss wird in unterschiedlichen Dipolproblemen untersucht um auf mögliche Design-Lösungen für ein praktisches Magnetsystem zu schlussfolgern.

Die Eignung mehrerer Optimierungsalgorithmen wird getestet und verglichen. Hohe Anforderungen werden an die Algorithmen gesellt. Die Zielfunktion hat eine sehr komplexe globale Landschaft mit vielen lokalen Extrema, so dass das Auffinden der globalen Maxima schwierig ist. Ein weiteres Hindernis sind die teuren Funktionsauswertungen die durch die FEM-Modelle zur Verfügung gestellt werden. Es werden nur die Eingabeparameter angegeben mit denen das Softwareprogramm die Zielfunction berechnet. Diese Art von Problemen können als Blackbox Probleme evaluiert werden, die besonders schwer zu optimieren sind.

Die Kenntnisse die durch die verschiedenen Dipolprobleme gewonnen wurden, werden angewendet um ein realistische Magnetsystem für die Anwendung in der LKA numerisch zu optimieren und zu analysieren.

Abstract

This thesis aims at theoretically and numerically investigating the optimization of the novel non-contact measurement method called Lorentz force velocimetry (LFV). LVF is based on the measurements of the Lorentz force acting on a magnet system close to electrically conducting media. Fluids with a low electric conductivity in the range of a few S/m present a special challenge. The Lorentz force is relatively small compared to measurements with liquid metals which have a conductivity that is 10^6 higher. Therefore disturbances have a high influence on the measurements and it is essential to improve the quality of the signal for industrial application. One possibility to reach this goal is the optimization of the magnet system.

To provide insights into the optimal fundamental form of the magnetic field a setup of dipoles is considered analytically with the appropriate conditions. More complex dipole arrangements are optimized numerically with finite element (FEM) software. The orientation of the magnetic moments and the positions of the dipoles belong to the feasible set of decision variables. The rate of their influence is investigated in different setups to infer possible design solutions for a practical magnet system.

The suitability of a variety of optimization algorithms is tested and compared. High demands are made to the algorithms. The objective function has a very complex landscape with a great number of local extrema, making the location of global maxima difficult. Another hindrance are the expensive function evaluations provided by the FEM models, where only the input parameters are given to the software program for the calculation of the objective function. These kind of problems can pose as possible black box problems which are especially difficult to optimize.

The knowledge gained by the different dipole problems is then applied to numerically optimize and analyze a realistic magnet system for the application in LFV.

Contents

1 Introduction **1**
- 1.1 Motivation . . . 2
- 1.2 Aims and Objectives . . . 3
- 1.3 Thesis Overview . . . 4

2 Theory of Lorentz Force Velocimetry for Weakly Conducting Fluids **5**
- 2.1 Basic Principles . . . 5
- 2.2 Governing Equations . . . 7
  - 2.2.1 Maxwell's Equations . . . 7
  - 2.2.2 Quasi-static Approximation . . . 9
  - 2.2.3 Magnetic Reynolds Number . . . 10
  - 2.2.4 Potential Functions . . . 11
  - 2.2.5 Boundary Conditions . . . 12
  - 2.2.6 Solid Body Approximation . . . 13
- 2.3 Lorentz Force Velocimetry . . . 14

3 Numerical Models **17**
- 3.1 PROMETHEUS . . . 17
- 3.2 COMSOL . . . 18
- 3.3 Mesh Study . . . 20

4 Dipoles - Analytic Approximation **26**
- 4.1 Analytic Lorentz Force . . . 27
- 4.2 Verification of Numerical FEM Model . . . 28

5 Optimization **33**
- 5.1 Introduction . . . 33
- 5.2 Formulation of the Problem . . . 34
  - 5.2.1 Analytic Optimization . . . 35
  - 5.2.2 Nelder-Mead Simplex Direct Search . . . 36
  - 5.2.3 Gradient-Ascent Method . . . 38
  - 5.2.4 Non-linear Optimization by Mesh Adaptive Direct Search . . . 38
- 5.3 Defining the Geometric Setup and Optimization Variables . . . 39

6 Results **42**
6.1 Completely Analytic Solution 42
6.2 Numerical Analytic Solution 47
6.3 Numerical FEM Solution 62
6.4 PROMETHEUS - Multi-Dipole-Ring Problems 67
6.5 COMSOL - Realistic Magnet System 76

7 Summary and Outlook **84**
7.1 Summary 84
7.2 Outlook 85

A Analytic Expression for the Lorentz Force **87**

Chapter 1

Introduction

The interaction between moving, electrically conductive media and a magnetic field is a highly complex field of theoretical physics. Many scientists have conducted research into this field. Einstein's special theory of relativity [14] was derived from a thought experiment, where the medium was a solid object. Faraday tried to measure the velocity of the Thames river and developed the basic principle for today's electromagnetic flow meters [54]. The flow meter uses closed electrical currents, i.e. eddy currents as measurement parameter. Eddy currents arise when an electrically conductive medium moves through a static magnetic field or when the electric medium is at rest, but the magnetic field changes in time. The eddy currents depend on the motion and conductivity of a medium which is under the influence of a magnetic field. They oppose their source, thus having a breaking effect on the medium. This was studied in detail by the Dutch mathematician and physicist Hendrik Antoon Lorentz in 1892 [34]. The breaking effect and the resulting force was named after him. The Lorentz force is the force a moving charge experiences in a magnetic and/or electric field.

The effect of eddy currents can be used in a wide range of practical applications. Most prominent is possibly induction heating [49]. At the TU Ilmenau a strong focus is on the Lorentz force as a measurement tool for the movement of conducting media, mainly liquids. As such, a whole research training group[1] undertakes experimental and numerical studies on liquid metals and salt water. A branch group studies defects in solid bodies. The fluid groups use Lorentz forces to measure the flow rate of the respective liquid. This measurement technique was termed Lorentz force velocimetry (LFV) [60].

LFV is a contactless technique to measure and analyze physical properties of moving media. The working principle is as follows (fig. 2.1) a magnet system generates a time independent and inhomogeneous magnetic field which acts on a moving conductor. The charges inside the conductor experience a Lorentz force that is perpendicular to their motion. Thus, they are deflected from their original path and form loops because of the spatially inhomogenious magnetic field. These loops, the

[1] TU Ilmenau: https://www.tu-ilmenau.de/lorentz-force/ (Homepage of the DFG-Graduiertenkollegs „Elektromagnetische Strömungsmessung und Wirbelstromprüfung mittels Lorentzkraft“)

eddy currents, produce a secondary magnetic field (Lenz's law [32]). The interaction of the eddy currents and the magnetic field gives rise to the Lorentz force which opposes the fluids motion. Consistent with Newton's 3rd law [41] an opposite but equal force acts on the magnet system, pulling them along the direction of the flow. This influence on the magnets can be measured for example by optical methods through deflection or by force compensation balance systems [64].

1.1 Motivation

For measurement in liquids of different properties, different flow meters need to be used. The criteria which determine the type of applicable flow meter are for example opacity, conductivity and corrosivity. For example: ultrasound doppler velocity (UDV) measurement methods can be used for the non-contact measurement of velocity profiles of transparent liquids [58], thus conductivity and corrosivity of the liquid do not matter; turbine-flow meters [5] are inserted into the fluid which needs to be non-corrosive; conducting and non-corrosive fluids can be measured by magnetic flow meters [63] which require direct contact. The meters in these applications are well developed and sophisticated, but the measurement of one specific type of fluid remains challenging, i.e. conductive, opaque (UDV not applicable) and corrosive/extremely hot fluids or fluids where direct contact with the measurement tool is not desired. Examples of these fluids are liquid metals, molten salt and other electrolytes, which can be very hot and corrosive or where contact is undesired. A selection of possible fields of application are the steel industry (molten metals), the food and beverage industry (milk, liquid eggs, beer, lemonades), the chemical industry (acids, alkaloids) or in water supply/waste-water treatment (chlorine dioxide solution, waste-water).

Since Faraday did his initial experiment at the river Thames, flow meters have been further advanced. Electromagnetic flow meters (EMFs) belong to the most common types of flow meters, next to positive displacement and differential pressure flow meters [57]. They combine the subjects of classical electromagnetism and fluid dynamics, belonging to the field of magnetohydrodynamics. The principle of an EMF is as follows: A conductive fluid fills a pipe completely. The fluid is under the influence of a magnetic field created by magnetic coils. Because the fluid is electrically conducting, this gives rise to a potential difference proportional to the velocity component of the fluid velocity, that is perpendicular to the flux lines of the magnetic field. The potential difference is measured by two electrodes which are diametrically and perpendicular to the pipe and in direct contact with with the fluid [54].

The required direct contact to the process liquid is a major drawback to the EMF. The material of the electrodes needs to permit good electrical contact with the measurement fluid and adequately resist corrosion. Also the connection between the flow meter and pipe must adhere to specific standards. For example: the food, beverage and pharmaceutical industries use super heated steam and chemical processes for cleaning and sterilization which the EMF must withstand [28].

The standard EMF with electrodes is not suitable for very weakly conducting fluids ($\sigma < 5\mu S/m$, although manufacturers recommend consultation if $\sigma < 30\mu S/m$). Here, a no-electrode EMF can be used. Instead of electrodes large-area capacitor plates are put on the outside of the pipe making the chemical compatibility between electrode and fluid redundant. Nevertheless, these EMFs can be very sensitive to vibrations [28].

The EMFs mentioned above are only suitable for fully filled pipes. In the case of partially filled pipes, additional equipment measures the filling level and additional pairs of horizontal electrodes have to be added at a lower level. The risk remains, that the fluid level drops below the lowest pair of electrodes canceling the signal [28].

For these fluids LFV is a very well suited method, but more research needs to be done for an effective and efficient implementation in industry. One special branch is the measurement of weakly conducting fluids. These produce only a relatively weak Lorentz force, which increases the influence of external disturbances, making the detection of the measurement signal difficult and ambiguous [64].

The measurement of the Lorentz force suffers because of the low conductivity. Compared with liquid metals the conductivity is approximately $10^6 S/m$ smaller. Thus, the measured force is in the range of μN. This greatly increases the influence of external disturbances, like vibrations, deformations of the housing caused by temperature, electromagnetic objects, etc. [12].

The source of the primary magnetic field consist of permanent magnets. Other sources are possible like coils [64], but experimental setups show that they have undesirable characteristics. They are heavy, need cooling during continuous operation and electric bondings are necessary. High temperature super conductors [66] are currently under investigation for the application in LFV since they generate very high magnetic fields.

1.2 Aims and Objectives

The goal is to improve measurement quality of the above described LFV for weakly conducting fluids. The force to noise ratio can be increased in two ways. First by shielding the magnet system. This lessens unwanted electromagnetic impact, but other influences like vibrations and expansionary changes remain. This will be the subject of future research. Second is the increase the Lorentz force F by optimizing the primary magnetic field. This is a very promising approach since the Lorentz force depends quadratically on the magnetic flux density B [60]:

$$F \sim \sigma v B^2,$$

where σ is the electrical conductivity and v the velocity of the fluid (fig. 2.1). Thus a doubling of the magnetic flux density will produce a four times higher Lorentz force. By maximizing the force to noise aspect ratio, the measurements will be of a higher quality and better suitable for industrial application.

The optimization of the magnetic field will be made under two aspects. One is a spatial approach, which investigates a configuration consisting of segmented magnetic rings surrounding a pipe. This will be done with three dimensional (3D) finite

element (FEM) simulation. The second is of a more theoretical nature. Point dipoles are put at relatively large distances around the cylinder (asymptotic approximation). Analytical expressions for the Lorentz force, its derivative and hessian matrix can be calculated, which help in the location of global/local maxima and while the maximum can only be derived analytically for selected cases, the Lorentz force can be optimized numerically.

To accomplish the proposed aims, the following steps are addressed in this thesis:

- Theoretical description of the physics of general LFV.
- Study of simplified academic setups gives insight for practical solutions.
- 3D FEM based simulations apply theoretical findings and provide possible practical applications.

1.3 Thesis Overview

The above stated steps and goals are presented in different chapters of this work. Chapter 2 explains the theory of LFV. In chapter 3 the numerical simulation software programs are presented. Chapter 4 develops the approximations for the analytical model and verifies the numerical model. Chapter 5 formulates the optimization problem and describes the optimization process with its methods and tools. Chapter 6 discusses the mathematical study and optimization of the different problems. Chapter 7 summarized the results and provides outlook for further work in LFV for weakly conductive fluids.

Chapter 2

Theory of Lorentz Force Velocimetry for Weakly Conducting Fluids

This chapter addresses the functional (chapter 2.1) and theoretical (chapter 2.2) principles of the contactless electromagnetic flow measurement technique LFV specifically for weakly conducting fluids. This method has been successfully applied to liquid metals even under industrial conditions [65], but it needs to be further refined for the application to weakly conducting fluids.

The technique is named Lorentz force velocimetry, since it measures the Lorentz force[1] which acts on the magnet system surrounding the fluid under observation.

2.1 Basic Principles

LVF is based on the principle of induction [24]. Fig. 2.1 shows the working principle. A process fluid with an electrical conductivity σ passes through a magnetic field $\vec{B}$ created by some kind of field source. According to Faraday's law the magnetic flux density induces eddy currents $\vec{J}$ in the fluid. As long as the working fluid is contained in an isolated pipe or channel the eddy currents form closed loops and generate a secondary magnetic flux density. The direction of the eddy currents is dictated by Lenz'law [32], it stipulates that the secondary magnetic field opposes the polarity of the primary magnetic field.

The interaction of eddy currents and magnetic flux density gives rise to the Lorentz force $\vec{F}$, which is oriented in a way that opposes the motion of the fluid, thus braking it. Newtons 3rd law [41] "lex tertia" or actio = reactio, also known as interaction principle, states that forces exist in pairs. The force pairs have the same magnitude but are opposite in sign. Applying this to the LFV setup gives: the magnetic field distribution that exerts the Lorentz force on the fluid (actio) and an opposing force that acts on the field source (reactio). This opposing force represents

[1] Actually, the Lorentz force acts on the fluid and a counter force, which is of equal magnitude but opposite in sign (Newton's 3rd law [41]), acts on the magnet system.

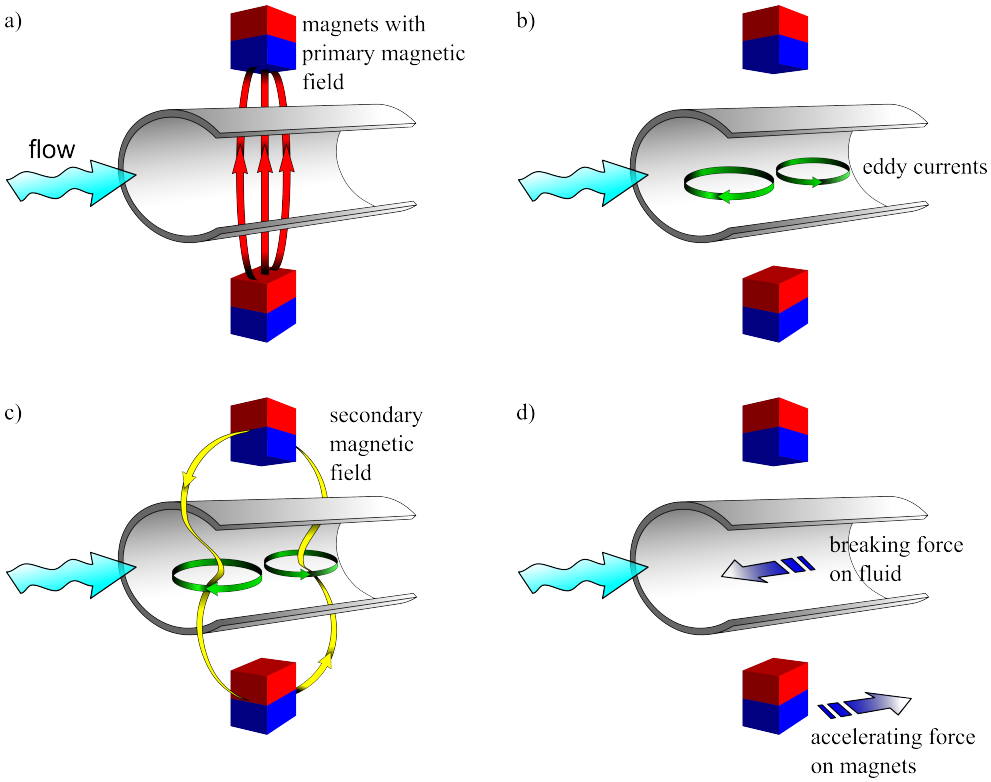

Figure 2.1: Working principle of Lorentz force velocimetry. Magnets create a primary magnetic field which acts on a moving electrically conducting fluid and gives rise to eddy currents. The interaction between magnetic field and eddy currents produce the Lorentz force, which breaks the fluid. An equal but opposite force pulls the magnets along the fluids direction.

the Lorentz force, since it has the same magnitude only the sign is opposite. The influence of the opposing force on the field distribution can be measured.

For these measurements, a steady, time-independent magnetic field is necessary. Currently a system of permanent magnets is used for experimental evaluations. The magnet system is emitter and receiver at the same time, since it creates the primary magnetic field and is exposed to the counter force.

Since the focus here is on weakly conducting fluids, beneficial assumptions and simplifications to the theory can be made. The effects of the eddy currents on the field source are neglected as are the influence of the Lorentz force on the fluid motion. These two effects must not be left out when liquid metals are concerned [61]. The fluid obeys Ohm's law and its electrical conductivity is isotropic and constant, i.e. unaffected by the magnetic flux density and the velocity profile. Also thermoelectric effects [48] are neglected. Furthermore, the fluid is nonmagnetic and has the permeability of Vacuum. This way, the fluid can only affect the magnet system because of its motion and electrical conductivity σ.

2.2 Governing Equations

The investigations in this work pertain to Lorentz force velocimetry for weakly conducting media. The used geometric and material parameters refer to an experimental saltwater channel [12]. However, a pipe is used here, instead of a square duct with a cross section of $50mm \times 50mm$. A pipe with radius $R = 25mm$ contains the working fluid with electrical conductivity $\sigma = 4S/m$. The pipe's axis aligns with the z-axis and its length L depends on the dipole configuration (fig. 2.3).

Dipoles are used for the analytic investigation and can represent realistic, possible magnet configurations. They are placed at a distance h from the surface of the conductive medium. The dipole moment is $m = 3.5Am^2$.

The following sections introduce the governing equations and the appropriate simplifications and boundary conditions for LFV. With these the problem can be solved via FEM simulations or even analytically with some additional simplifications [43], [8], [26].

2.2.1 Maxwell's Equations

Maxwell's equations [24](p3, p15) are the basis for every electromagnetic phenomenon. They can be divided into a microscopic and macroscopic formulation. With the microscopic formulation every atom of a medium needs to be considered and magnetic properties cannot be derived without additional knowledge of quantum mechanics. For macroscopic media, it is almost impossible to solve the microscopic Maxwell's equations. It is also not necessary, since the macroscopic Maxwell's equations need only the mean values of fields and sources over a volume which is large compared to a single atom or molecule. The macroscopic Maxwell's equations are:

Gauss's law for magnetism:

$$\nabla \cdot \vec{B} = 0 \tag{2.1}$$

Gauss's law:

$$\nabla \cdot \vec{D} = \rho \tag{2.2}$$

Maxwell-Faraday equation:

$$\nabla \times \vec{E} = -\frac{\partial \vec{B}}{\partial t} \tag{2.3}$$

Ampère's circuital law:

$$\nabla \times \vec{H} = \vec{J} + \frac{\partial \vec{D}}{\partial t} \tag{2.4}$$

where t is the time, $\vec{E}$ is the electric field vector, $\vec{B}$ is the magnetic flux density vector, ρ is the charge carrier density and $\vec{J}$ is the current density. Additional fields are the displacement field $\vec{D}$ and the magnetizing field $\vec{H}$. The constitutive relations link the vector fields together:

$$\vec{D} = \epsilon_0 \epsilon_r \vec{E} \qquad \vec{B} = \mu_0 \mu_r \vec{H} \tag{2.5}$$

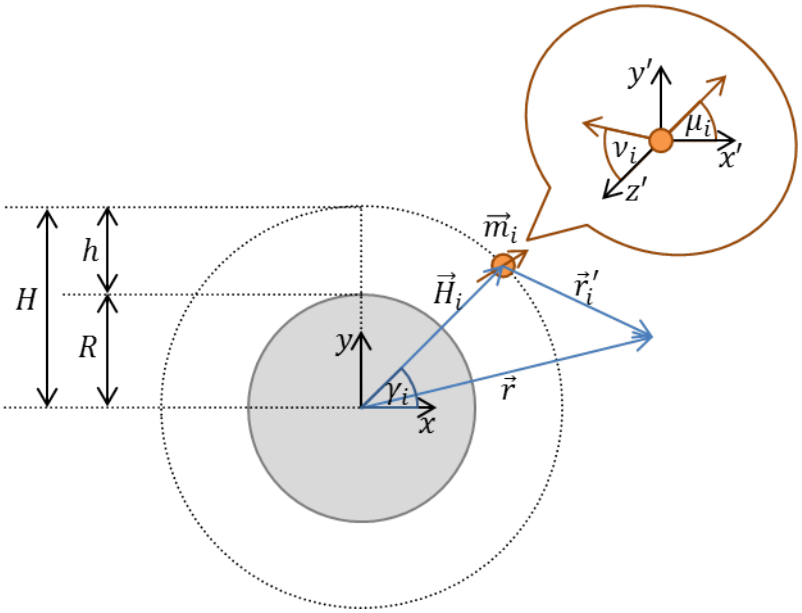

Figure 2.2: xy plane of the dipole problem setup. The position of the dipoles $\vec{m}_i$ is fixed to a specific distance $\vec{H}_i$ in the $z = 0$ plane. The orientation of the magnetic moments are given by the spherical coordinates μ_i and ν_i. The magnetic field created by $\vec{m}_i$ at $\vec{r'}_i$ is expressed with eq. 4.1.

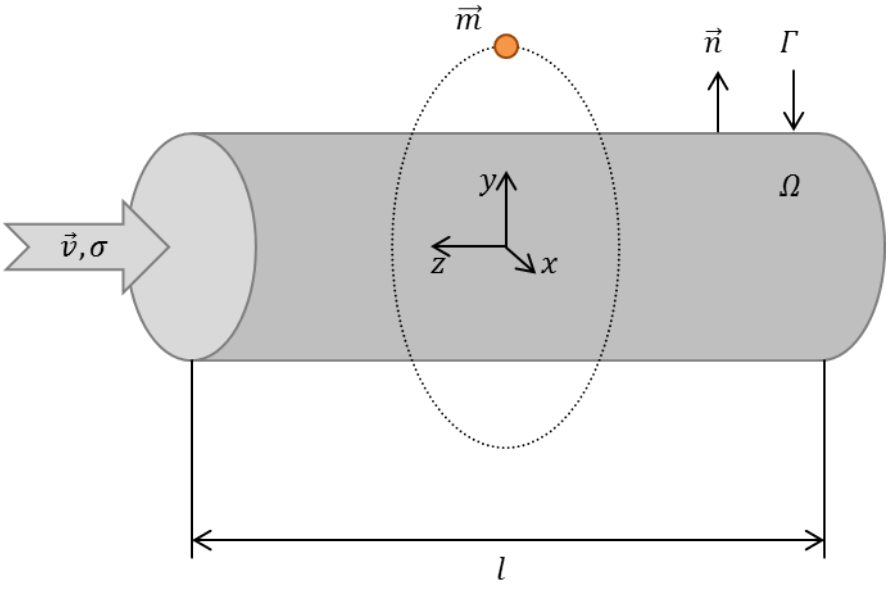

Figure 2.3: 3D setup of the cylinder surrounded by a dipole. The cylinder domain Ω with boundary Γ and normal vector to the surface $\vec{n}$ moves with a velocity $\vec{v}$ and has an electrical conductivity σ.

$\epsilon_0 = 8.8 \cdot 10^{-12} F/m$ is the permittivity and $\mu_0 = 4\pi \cdot 10^{-7} H/m$ the permeability of free space.

The physical properties σ, μ_r and ϵ_r are usually second-order tensors and depend on the temperature T, i.e. $\sigma = \sigma(\vec{E}, T)$, $\mu_r = \mu_r(\vec{E}, T)$ and $\epsilon_r = \epsilon_r(\vec{E}, T)$ [7]. Since the optimization aspect dominates this thesis, all materials are assumed to be isotropic and independent of other factors like temperature or field values, meaning that these quantities are scalar and constant. Furthermore, the electric permittivity of the working fluid is set to one, the relative permeability is about one for diamagnetic and paramagnetic materials which are in the focus here [25].

The magnetic flux density ($\vec{B}$) produced by the permanent magnets or magnetic point dipoles induce eddy currents ($\vec{J}$) in the electrically conducting (σ) and moving ($\vec{v}$) fluid (fig. 2.1):

$$\vec{J} = \sigma(\vec{E} + \vec{v} \times \vec{B}). \tag{2.6}$$

The eddy currents are solenoidal, since the walls of the pipe under consideration are insulating. Thus, the current is conserved inside the working liquid:

$$\nabla \cdot \vec{J} = 0. \tag{2.7}$$

These equations together with the following approximations build the framework for LFV for weakly conducting media and enable an analytic and computational investigation of different setups.

2.2.2 Quasi-static Approximation

A very important simplification that is utilized is the quasi-static approximation, where the displacement current can be discarded. The quasi-static approximation holds when the velocity in the applications are very small compared to the speed of light c, then the magnetic field changes relatively slowly with time. The finite velocity of light with which electromagnetic waves travel is disregarded, instead it is assumed that the electromagnetic field moves instantaneously. This is a good approximation when the system under observation is small compared to the electromagnetic wavelength, which corresponds to the dominating time scale of the problem.

A scale analysis shows the dependencies of the appropriate terms. For this characteristic values are needed for the relevant parameters, i.e. B and E are a typical scales for the magnetic and electric field respectively, v is a typical fluid velocity, τ a typical time scale and L a typical length scale, meaning that $v = L/\tau$. Then Maxwell-Faraday's equation (eq. 2.3) requires that:

$$\frac{E}{L} \sim \frac{B}{\tau} \Rightarrow \frac{E}{B} \sim \frac{L}{\tau} = v.$$

The same procedure can be applied to determine the ratio between displacement current and total current (eq. 2.4):

$$\frac{|\partial \vec{D}/\partial t|}{|\nabla \times \vec{H}|} \sim \frac{D/\tau}{B/\mu_0 L} = \epsilon_0 \mu_0 \frac{EL}{B\tau} \sim \frac{L^2}{c^2 \tau^2} = \frac{v^2}{c^2}.$$

Thus, the displacement current $\partial\vec{D}/\partial t$ can be neglected in Ampère's circuit law (eq. 2.4), for small velocities $v^2 \ll c^2$:

Ampère's circuital law (eq. 2.4) then becomes:

$$\nabla \times \vec{H} = \vec{J}. \tag{2.8}$$

2.2.3 Magnetic Reynolds Number

As mentioned above the influence of the secondary magnetic field created by the induced currents on the primary magnetic field is neglected. This decision is supported by the value of the magnetic Reynolds number R_m [24]. It is a nondimensional parameter that presents the ratio of induced (or secondary $\vec{B}_s$) to applied (or primary $\vec{B}_p$) magnetic field and depends only on the characteristics of the process fluid, i.e. its size L, velocity v, electric conductivity σ and relative permeability μ_0:

$$R_m = \frac{|\vec{B}_s|}{|\vec{B}_p|} = \mu_0 \sigma v L.$$

Special attention needs to be put on the size parameter L. This geometric quantity depends on the setup and needs to be determined for every single application. Here, it is the diameter of the pipe R (fig. 2.3).

The magnetic Reynolds number can be derived via the induction equation with the diffusive term. For its derivation, the rotation of Ampère's circuital law (eq. 2.8) is taken:

$$\nabla \times (\nabla \times \vec{H}) = \nabla \times \vec{J}.$$

Then Ohm's law (eq. 2.6) and the constitutive relation for the magnetic field (eq. 2.5), assuming that μ_0 and σ are constant, are inserted:

$$\frac{1}{\mu_0} \nabla \times (\nabla \times \vec{B}) = \sigma \nabla \times (\vec{E} + \vec{v} \times \vec{B}) = \sigma(\nabla \times \vec{E} + \nabla \times (\vec{v} \times \vec{B})).$$

Considering the product rule:

$$\nabla \times (\nabla \times \vec{B}) = \nabla(\nabla \cdot \vec{B}) - \Delta \vec{B},$$

the fact that $\vec{B}$ is divergence free (eq. 2.1) and Maxwell-Faradays equation (eq. 2.3):

$$-\frac{1}{\mu_0} \Delta \vec{B} = \sigma(-\frac{\partial \vec{B}}{\partial t} + \nabla \times (\vec{v} \times \vec{B})).$$

Rearranging gives the magnetic induction equation:

$$\frac{\partial \vec{B}}{\partial t} = \frac{1}{\mu_0 \sigma} \Delta \vec{B} + \nabla \times (\vec{v} \times \vec{B}). \tag{2.9}$$

The quantity $1/\mu_0\sigma$ is the magnetic diffusivity. This equation characterizes the development of the magnetic flux density. It depends on the induction and diffusive

term (first and second terms on the right hand side, respectively). The induction term depends on the velocity field $\vec{v}$ and is the only one that can produce a field. Without the presence of a velocity field $\vec{v}$ the diffusive term lets the field decay.

The magnetic Reynolds number can be derived with this equation when the necessary parameters are replaced with the product between the characteristic values (chapter 2.2.2) and nondimensional quantities denoted by the * symbol, then $\vec{B} = B\vec{B}^*$, $\vec{v} = v\vec{v}^*$, $t = \tau t^*$ and $\nabla = \nabla^*/L$.

Then the induction equation (eq. 2.9) becomes:

$$\frac{B}{\tau}\frac{\partial \vec{B}^*}{\partial t^*} = \frac{vB}{L}\nabla^* \times (\vec{v}^* \times \vec{B}^*) + \frac{1}{\mu_0 \sigma}\frac{B}{L^2}\Delta^* \vec{B}^*.$$

Rewriting this equation and using $v = L/\tau$:

$$\frac{\partial \vec{B}^*}{\partial t^*} = \nabla^* \times (\vec{v}^* \times \vec{B}^*) + \frac{1}{\mu_0 \sigma v L}\Delta \vec{B}^*.$$

The prefactor of the diffusive term is the inverse of the dimensionless magnetic Reynolds number:

$$R_m = \mu_0 \sigma v L.$$

It is the magnetic analogue of the Reynolds number in fluid dynamics and indicates the relative strength of the inductive/convective and diffusive terms of a magnetic fluid via the induction equation:

$$\frac{|\nabla \times (\vec{v} \times \vec{B})|}{|\frac{1}{\mu_0 \sigma}\Delta \vec{B}|} \sim \frac{vB/L}{\frac{1}{\mu_0 \sigma}B/L^2} = \mu_0 \sigma v L.$$

If $R_m \ll 1$ then the secondary magnetic field is small compared to the primary field and can be neglected. The overall effect of the magnetic field on the fluid amounts to an extra dampening term in the Navier-Stokes equations. The fluid velocity has little influence on the the magnetic field, since the induced magnetic field is negligible compared with the primary magnetic field. This approximation immensely simplifies the problem.

If $R_m \gg 1$ then the perturbation of the primary magnetic field is significant and has to be taken into account. The magnetic field is strongly influenced by the fluid velocity. The advection of the magnetic field by the fluid velocity can generate Alvén waves, an important phenomenon in magnetohydrodynamics [11].

2.2.4 Potential Functions

The magnetic flux density can be expressed by the magnetic vector potential $\vec{A}$. Since the divergence of the magnetic field is zero (eq. 2.1), the magnetic field can be expressed by the rotation of an arbitrary vector field:

$$\vec{B} = \nabla \times \vec{A}. \tag{2.10}$$

Since only static vector fields are consider, all time derivation $\frac{\partial}{\partial t} = 0$. Thus, in eq. 2.3 the rotation of the electric field is equal to zero. When the rotation of a vector field is zero then it is possible to express the vector field with a gradient field since the divergence of a rotation $(\nabla \cdot \nabla\times)$ of a vector field is zero. In this case:

$$\vec{E} = -\nabla\phi \tag{2.11}$$

and ϕ is the electric scalar potential.

In general, if the time dependence is considered, the partial time derivative of the magnetic vector potential needs to be included. $\vec{A}$ replaces $\vec{B}$ in eq. 2.3 and the integration gives the following expression for the electric field:

$$\vec{E} = -\nabla\phi - \frac{\partial\vec{A}}{\partial t}.$$

$\vec{B}$ and $\vec{E}$ are not uniquely defined by $\vec{A}$ and ϕ. An gradient of an arbitrary scalar field $\nabla\xi$ can be added to the vector potential and the time derivative of an arbitrary scalar field $\partial_t\xi$ can be subtracted from the scalar potential without changing the field. This gauge transformation holds for any scalar function ξ:

$$\vec{A} \to \vec{A}' = \vec{A} + \nabla\xi$$
$$\phi \to \phi' = \phi - \frac{\partial\xi}{\partial t}.$$

The fields are invariant if they are not changed by the gauge transformation, i.e. $\vec{B} = \vec{B}'$ and $\vec{E} = \vec{E}'$:

$$\vec{B}' = \nabla \times \vec{A}' = \nabla \times \vec{A} + \nabla \times \nabla\xi = \nabla \times \vec{A} = \vec{B}$$
$$\vec{E}' = -\nabla\phi' - \frac{\partial\vec{A}'}{\partial t} = -\nabla\phi + \nabla\frac{\partial\vec{\xi}}{\partial t} - \frac{\partial\vec{A}}{\partial t} - \frac{\partial}{\partial t}\nabla\vec{\xi} = -\nabla\phi - \frac{\partial\vec{A}}{\partial t} = \vec{E}.$$

Therefore Maxwell's equations (eq. 2.1-2.4) have a gauge symmetry.

2.2.5 Boundary Conditions

It is necessary to know the appropriate boundary conditions [47] for the modeling of the different regions, i.e. the conductor, air and magnets. This is especially important for the FEM simulations where symmetry reduces the computation domain and saves time.

There are three types of boundary conditions. Initial conditions also belong to this group, but are ignored here since there is no time dependence.

First are the boundary conditions that confine a parameter to a specific domain, for example the eddy current. As mentioned above the eddy currents are confined to the conductor. Since there are no sources or sinks the eddy current field is divergence free (eq. 2.7) and forms closed loops. The conductor walls are non-conducting. Thus, there is no current flow into the wall, meaning the normal component of the eddy

current density J_n and the normal derivative of the electric scalar potential $\partial\phi/\partial n$ vanish, $\vec{n}$ is the normal vector to the surface of the pipe (fig. 2.1).

Second are the boundary conditions that change a parameter when it crosses domain boundaries, also called interface conditions. This is the case, when the magnetic and electric fields cross the interface of two media with different physical properties, i.e. electrical permittivity and magnetic permeability. Here the vector field are not differentiable and the following conditions are needed, where $\vec{n}_{ab}$ is a normal vector from medium a to medium b and ρ_s is the surface charge of the interface.

For the electric $\vec{E}$ and displacement field $\vec{D}$:

$$\vec{n}_{ab} \times (\vec{E}_b - \vec{E}_a) = 0 \qquad (\vec{D}_b - \vec{D}_a) \cdot \vec{n}_{ab} = \rho_s.$$

The tangential component of the electric field E_t and the normal component of the displacement current D_n are continuous across the interface.

For the magnetic flux density $\vec{B}$ and the magnetic field strength $\vec{H}$:

$$(\vec{B}_b - \vec{B}_a) \cdot \vec{n}_{ab} = 0 \qquad \vec{n}_{ab} \times (\vec{H}_b - \vec{H}_a) = \vec{J}_s$$

with the surface current density $\vec{J}_s$ of the interface. The normal component of the magnetic flux density B_n and the tangential component of the magnetic field intensity H_t are continuous across the interface.

For the eddy current density $\vec{J}$:

$$(\vec{J}_b - \vec{J}_a) \cdot \vec{n}_{ab} = 0.$$

Last are the symmetry boundary conditions. These can immensely reduce computational resources and time. Symmetry planes always mirror the geometry exactly, while the vector fields are either symmetric or antisymmetric relative to the symmetry plane. The magnetic field is mirrored exactly if the magnetic field has only a tangential component in the symmetry plane. As a result the current can only flow normal to the symmetry plane. Thus, this symmetry plane is parallel to $\vec{B}$ and perpendicular to $\vec{J}$. The opposite case is if the symmetry plane is parallel to the current flow and perpendicular to the magnetic field. In the mirror plane the currents have only a tangential component while the magnetic field is normal to it.

These boundary conditions simplify an electromagnetic model and reduce the size of FEM models. Especially for simulation purposes it is a significant reduction of computational requirements and time.

2.2.6 Solid Body Approximation

LFV is a measurement method especially targeted for liquids. However the simulation of liquids is computationally complex and time consuming since the full Navier-Stokes equations are involved. It is unfeasible to consider the fluid flow in an optimization procedure. Time is one of the most important aspects in optimization. In order to reduce, it a model is usually simplified as much as possible. One very

useful and extremely effective approach is to replace the highly complex fluid flow with a solid body velocity profile. Meaning that a plug flow profile is used instead of the laminar or turbulent velocity distribution for the process medium. The error of this assumption is relatively low, especially for turbulent flows, while the simulation time is significantly decreased. This approximation is also called solid body approximation since the plug profile has the same velocity distribution at every point like a solid body [1].

The corresponding boundary conditions for this assumption are specified in the next section.

2.3 Lorentz Force Velocimetry

The setup of LFV is arbitrary. In order to simplify the problem the process fluid is contained in a pipe with radius R. Consequently, cylindrical coordinates can be used whenever properties depend on the radial component $\vec{r}$. Additionally, the pipe's axis aligns with the z-axis (fig. 2.3), meaning that there is only a z-component of the velocity, because of the solid body approximation (chapter 2.2.6):

$$\vec{v} = (v_x, v_y, v_z) = (0, 0, v_z). \tag{2.12}$$

The Lorentz force $\vec{F}$ develops in the domain Ω, i.e. the conductor, because of the interaction of eddy currents and magnetic flux density (fig. 2.1):

$$\vec{F} = \int_{\Omega} \vec{J} \times \vec{B} d\Omega. \tag{2.13}$$

Expanding the cross product in the integral:

$$(\vec{J} \times \vec{B}) = \begin{pmatrix} J_y B_z - J_z B_y \\ J_z B_x - J_x B_z \\ J_x B_y - J_y B_x \end{pmatrix}.$$

Since the movement of the process fluid is restricted to the z-direction, only the z-component of the Lorentz force is of interest:

$$F_z = \int_{\Omega} (J_x B_y - J_y B_x) d\Omega. \tag{2.14}$$

The principle of LFV bases on Ohm's law. When a conductive medium with an electrical conductivity σ moves with a velocity $\vec{v}$ through the magnetic flux density $\vec{B}$ then eddy currents $\vec{J}$ are induced in the conductor (fig. 2.1):

$$\vec{J} = \sigma(-\nabla\phi + \vec{v} \times \vec{B}). \tag{2.15}$$

The $\vec{v} \times \vec{B}$ term reduces to:

$$\vec{v} \times \vec{B} = \begin{pmatrix} v_y B_z - v_z B_y \\ v_z B_x - v_x B_z \\ v_x B_y - v_y B_x \end{pmatrix} = \begin{pmatrix} -v_z B_y \\ v_z B_x \\ 0 \end{pmatrix}. \tag{2.16}$$

Thus, the x, y and z-components of (eq. 2.6) are:

$$\begin{pmatrix} J_x \\ J_y \\ J_z \end{pmatrix} = \sigma \begin{pmatrix} -\partial_x\phi + v_y B_z - v_z B_y \\ -\partial_y\phi + v_z B_x - v_x B_z \\ -\partial_z\phi + v_x B_y - v_y B_x \end{pmatrix} = \sigma \begin{pmatrix} -\partial_x\phi - v_z B_y \\ -\partial_y\phi + v_z B_x \\ -\partial_z\phi \end{pmatrix}. \tag{2.17}$$

The boundary conditions for the electric potential ϕ can be inferred from the boundary conditions for the eddy currents. The currents are confined to the process fluid, i.e. the region Ω. Thus, the normal component of the eddy current vector $J_n = 0$ on the surface Γ (fig. 2.3) and with the radial unit vector $\vec{e_r}$:

$$\vec{J} \cdot \vec{e_r} = 0 \text{ on } \Gamma \text{ at } r = R \;\Rightarrow \partial_r\phi = \vec{e_r} \cdot (\vec{v} \times \vec{B}) \text{ on } \Gamma. \tag{2.18}$$

The unit vector $\vec{e_r}$ in cartesian coordinates is $\vec{e_r} = \vec{e_x}\cos\beta + \vec{e_y}\sin\beta$. β is the polar angle and $\cos\beta = x/r$, $\sin\beta = y/r$. Inserting this and eq. 2.16 into eq. 2.18:

$$\begin{aligned} \partial_r\phi = \vec{e_r} \cdot (\vec{v} \times \vec{B}) &= (\vec{e_x}\frac{x}{r} + \vec{e_y}\frac{y}{r}) \cdot \begin{pmatrix} -v_z B_y \\ v_z B_x \\ 0 \end{pmatrix} \\ &= -\frac{x}{r} v_z B_y + \frac{y}{r} v_z B_x = v_z(-B_y\cos\beta + B_x\sin\beta). \end{aligned} \tag{2.19}$$

Inserting eq. 2.6 and eq. 2.11 into the law of current conservation (eq. 2.7) and assuming that σ is constant gives:

$$\begin{aligned} \nabla \cdot \vec{J} = \nabla \cdot (\sigma(-\nabla\phi + \vec{v} \times \vec{B})) = \sigma(-\nabla \cdot \nabla\phi + \nabla \cdot \vec{v} \times \vec{B}) = 0 \\ \Rightarrow \Delta\phi = \nabla \cdot (\vec{v} \times \vec{B}). \end{aligned} \tag{2.20}$$

Applying the product rule on the right hand side of eq. 2.20:

$$\Delta\phi = \nabla \cdot (\vec{v} \times \vec{B}) = \vec{B} \cdot (\nabla \times \vec{v}) - \vec{v} \cdot (\nabla \times \vec{B}). \tag{2.21}$$

The velocity of the fluid is $\vec{v} = v_z\vec{e_z}$. Furthermore, the solid body approximation is used, meaning that instead of having a parabolic or turbulent velocity profile, the process liquid has a plug like profile moves as if it would be a solid body. This approximation has been employed before [1] where it was also shown that the error this simplification brings is negligible. Thus, v_z is constant and:

$$\nabla \times \vec{v} = 0.$$

The magnetic dipole field is an irrotational vector field and the secondary magnetic field created by the eddy currents is neglected, resulting in:

$$\nabla \times \vec{B} = 0.$$

Inserting this into eq. 2.21:

$$\Delta\phi = 0. \tag{2.22}$$

Because of the assumptions of a kinematic problem ($\vec{v}$ is given) and neglecting the secondary magnetic flux density, the Lorentz force (eq. 2.13) can be calculated when $\vec{B}$ and the electric potential (eq. 2.6) are known, together with the boundary conditions (eq. 2.18).

Complex magnetic flux density sources (elaborate magnet systems) are only solvable via computationally heavy and time consuming FEM simulations. The only way to derive analytic solutions is for rather simple arrangements, for example when dipoles are considered as source for the magnetic flux density. This will be done in chapter 4.

Chapter 3

Numerical Models

Numerical simulations contribute significantly to the cost and time efficient design and optimization of technical applications. They help to understand the physical interactions in fundamental research and make prototype design less risky.

For the development of Lorentz force flowmeters knowledge of the interaction between magnet system and measurement fluid are vital for a successful setup. Most important is the prediction of the force and torque with which the fluid acts on the magnet system. The necessary data is obtained by numerically solving the governing equations. The validity of these complex simulations are verified by analytic problems with known solutions [6], [51].

Two FEM codes are available here, the in-house code PROMETHEUS [35] and the commercial software COMSOL Multiphysics [10]. In this chapter both codes are introduced and their advantages and disadvantages stated.

3.1 PROMETHEUS

For the academic problem with dipoles the in-house code PROMETHEUS [35] is used. The advantage of independent software programs is that it is license-free. PROMETHEUS was developed at the Technische Universität Ilmenau in the group of Electro-Thermal Energy conversion. It is used in science and industry alike [35]. It is still being worked on and further extended. For this work the code was translated from Pascal to C, in order to enable parallel computing on the cluster of the computation center using Open MPI [17]. This significantly reduces computational time and is especially favorable in optimization processes, when many parameter are used or a lot of iterations have to be made to archive good statistical results. Furthermore, a gradient ascent method was implemented for optimization purposes (chapter 5.2.3).

PROMETHEUS considers linear and non-linear material properties, boundary conditions and the coupling of different fields (magnetic, electric, thermal). It is able to solve steady and non-steady-state potential and temperature fields and quasi-stationary electromagnetic fields in 1D, 2D and 3D and 2D calculation of mechanical tension fields. It automatically generates meshes in 2D and 3D using a macro-element concept [69]. It is possible to postprocess the resulting data to a

limited extend via POST4. For a more sophisticated post processing, vtk [52] files where generated, enabling the use of the open-source data analysis and visualization application PARAVIEW [22].

Here, PROMETHEUS solves the FEM calculations based on the electric scalar potential (ϕ - formulation). Inserting Ohm's law (eq. 2.1) into the divergence-free character of the eddy currents (eq. 2.7) gives:

$$\nabla \cdot \left[\sigma \left(-\nabla\phi + \vec{v} \times \vec{B}\right)\right] = 0 \tag{3.1}$$

with the boundary condition $\partial_n \phi = \vec{n} \cdot \left(\vec{v} \times \vec{B}\right)$.

Thus, one equation describes the dipole problem with one unknown ϕ. The material parameters σ and $\mu_0\mu_r$ are constant and predefined.

PROMETHEUS solves the differential equation (eq. 3.1) with the FEM [69], [46]. The method of finite elements was developed in the 60s and is one of the most important numerical techniques for finding approximate solutions of differential equations in engineering and physics. The entire problem domain is subdivided into finite elements. The more complex equation over the large domain is approximated using variational methods by minimizing an error function in the finite elements. The electric potential function is substituted by its respective value at each node and multiplied by a form function. The form function is 1 at the relevant node and 0 at all other nodes, leading to a sparse band matrix. PROMETHEUS uses the Galerkin method of weighted residuals to solve the partial differential equations [9]. Since the functions are approximated in each element, the partial differential equations are no longer exactly fulfilled. The residual between exact and approximated formulation depends on the location (x,y,z). The Galerkin method minimizes the residuals in the solution domain. Ideally, the integral of the residuals over the domain should vanish. The resulting system of equations is solved by an incomplete Cholesky conjugate gradient method [50].

PROMETHEUS has the particular feature to use so called macro-elements which are built by a special preprocessing program. A macro-element is a certain geometric entity which is constructed of finite elements. They are defined by the coordinates, the subdivisions along edges and the ratio of segmentation if they are non-equidistant. Here prisms are used. Spatial functions can be applied to the surfaces of the macro-elements in order to deform them, i.e. the cylinder used here is made of curved macro-elements. Each macro-element is assigned to a specific domain, which contains material properties. Boundary and symmetry conditions can be applied on the surface of the macro-elements. It is possible to build very sophisticated geometric entities based on this rather simple macro-element method.

A gradient-ascent method [55] was implemented for optimization (section 5.2.3.

3.2 COMSOL

COMSOL Multiphysics [10] is a commercial software. It simulates physical processes based on differential equations discretized on finite elements. COMSOL is able to couple different physical modules which enables multiphysics analysis. In this work

the partial differential equations (PDE) module is used for the dipole setups and the AC/DC module is used for setups with realistic magnet systems which are not possible to simulate with PROMETHEUS.

PDE Module

The setup for the PDE module is sketched in fig. 2.3. The surface Γ whose normal unit vector is $\vec{n}$ encompasses the domain Ω of the cylinder. The dipole(s) outside of Ω create the magnetic field $\vec{B}$ inside the pipe. The cylinder moves with the given velocity $\vec{v}$ (eq. 2.12). The electric potential ϕ is solved with the following differential equation for a constant conductivity σ:

$$\nabla \cdot \vec{J} = \nabla \cdot (-\nabla\phi + \gamma) = 0$$

with:

$$\gamma = \vec{v} \times \vec{B}$$

resulting in:

$$\Delta\phi = \nabla \cdot \vec{v} \times \vec{B}.$$

The boundary conditions specify zero flux across Γ:

$$\begin{aligned} -\vec{n} \cdot (-\nabla\phi + \gamma) &= 0 \\ \Leftrightarrow \vec{n} \cdot \nabla\phi &= \vec{n} \cdot \gamma \\ \Rightarrow \partial_n\phi|_\Gamma &= \vec{n} \cdot (\vec{v} \times \vec{B})|_\Gamma. \end{aligned}$$

The problem is steady stationary and as such there is no change in time:

$$\partial_t\phi = 0 \text{ in } \Omega.$$

A pointwise constraint for the potential $\phi = 0$ is used on the ends of the cylinder in order to ensure uniqueness. Every value of potential is measured with respect to that zero.

AC/DC Module

The PDE modules is only suited for simple setups like the dipole formulation. For more complex realistic magnet systems without an analytic expression for the magnetic flux density the AC/DC module is used. It simulates electromagnetic processes based on Maxwell's equations (chapter 2). The AC/DC module is further subdivided into physics interfaces, which cover different types of electromagnetic field simulations. They solve for the physical quantities ϕ, the electric scalar potential, $\vec{A}$, the magnetic vector potential and ψ, the magnetic scalar potential (tb. 3.1). The appropriate interface needs to be chosen depending on the type of electromagnetic problem, i.e. electro-/magnetostatic, electric currents in conductive media or low-frequency simulation. The available study type and variables depend on the selected interface. The number of variables determines how many degrees of freedom are solved. The most complex AC/DC physics interface is mef (magnetic and

physics interface	dependent variables	field components	applicable domain
mef (magnetic and electric fields)	ϕ, $\vec{A}$	$\vec{B}$,$\vec{E}$,$\vec{A}$,$\vec{J}$	conductor
mfnc (magnetic fields, no currents)	ψ	$\vec{B}$	air

Table 3.1: Summary of the physics interfaces of COMSOL Multiphysics, which are used for the simulations.

electric fields). It solves for ϕ and $\vec{A}$, i.e. there are four variables at every grid point leading to a high number of DoF which puts heavy demands on computational time and effort. Every individual problem should be analyzed to determine if a simpler interface, one with less dependent variables, can be applied.

The problem here involves stationary magnetic fields produced by permanent magnets in a non-conductive air domain and a moving conductor. The magnetic field induces eddy currents in the conductor. The appropriate interface for the conductor is mef. However, the air domain is non-conductive, meaning that no eddy currents develop. Here it is possible to use the physics interface mfnc (magnetic fields, no currents). mfnc has only one dependent variable, the magnetic scalar potential ψ. The coupling of these interfaces at the domain boundary Γ reduces the number of DoF, since only one variable, ψ, is solved on the nodes of the air domain. The mef interface simulates the field components of the magnetic and electric field, the magnetic potential and the current density. The mfnc interface only simulates the field components of the magnetic field. The two interfaces are coupled at the boundary surface Γ, i.e. the surface of the conductor, where the magnetic field of the mfnc interface goes over into the magnetic field of the mef interface.

COMSOL and PROMETHEUS solve the same differential equations for this specific case but internally COMSOL uses quadratic shape functions for each element, while PROMETHEUS uses linear shape functions.

3.3 Mesh Study

[8] studied mesh convergence for a dipole very close to the cylinder. They used a ratio of $h/R = 0.005$, i.e. when $R = 25mm$ then $h = 0.125mm$. This is the opposite case of the asymptotic approximation. The finite radius and curved surface of the cylinder become insignificant, approaching the case of a dipole close to a translating halfspace. The analytic solution for a single dipole is [43]:

$$F_a = -\frac{1}{512\pi}\frac{\mu_0^2\sigma v}{h^3}(2m_x^2 + m_y^2 + 4m_z^2). \tag{3.2}$$

Because is not possible to simulate an infinitely long moving object, its length l needs to be sufficient to eliminate effects due to finite length. l is varied depending on the distance h and different meshes are used in the computations to verify mesh convergence in representative cases. A systematic variation of the length shows

ζ_f in mm	ζ_c in mm	number of elements	F_n/F_0	ΔF in %
2.00	8.00	2448	3.0010^8	1.5110^4
1.00	4.00	32760	3.6610^7	1.8410^3
0.25	1.00	1915872	6.4710^5	3.1510^1
0.10	0.50	25934796	4.9810^4	1.5010^0
0.09	0.36	38840580	4.8310^4	1.4310^0
0.08	0.32	51422112	4.9210^4	1.4710^0

Table 3.2: Parameters for the nonuniform meshes in PROMETHEUS. ζ_f, ζ_c are the numbers of mesh finesness.

$l = 5h$ to be an adequate value for the simulations. However, the mesh convergence study in tb. 3.4 and 3.2 was done with $l = 7h$.

The axial component is the main Lorentz force component (eq. 2.14), because the moving object is oriented along the z axes and its velocity is $\vec{v} = v_z\vec{e_z}$. The relative error ΔF for the force component asserts the difference between analytic F_a (eq. 3.2) and numeric F_n calculation:

$$\Delta F = \frac{(F_n - F_a)}{F_a}. \tag{3.3}$$

F_n depends on the mesh size. Because the dipole is very close to the cylinder, strong gradients of the magnetic flux density penetrate the cylinder. In order to resolve these changes the sensitive region in the middle of the cylinder it is more finely meshed (fig. 4.1).

Mesh Study PROMETHEUS

In the PROMETHEUS model the sensitive central region of the pipe is again $l/8$ wide and meshed with the parameter ζ_f. The size of the mesh elements then increase towards the ends of the cylinder as defined by the parameter ζ_c. There is no outer margin of the sensitive region like in the COMSOL model. The sensitive region extends along the whole cross section. Fig. 3.1 displays the mesh for $\zeta_f = 1mm$, $\zeta_c = 4mm$.

A mesh convergence study (tab. 3.2) was done for one dipole oriented perpendicular to the cylinder surface, with a cylinder length of $L = 7(h + R)$. The calculated Lorentz force converges with increasing numbers of mesh elements. Fig. 3.2. shows convergence of the numerical results to the analytic solution with increasing numbers of nodal values, i.e. degrees of freedom, in the grid. The relative error decreases approximately with the elements size and is thus inversely proportional to the number of elements. The results show a good agreement with [8], considering the different focuses on the meshes, i.e. a fine mesh along the total middle part of the cylinder vs. a single selective concentration.

It is important that the cylinder is sufficiently long in order to exclude the influence of edge effects. The length variation was done for one dipole and with the

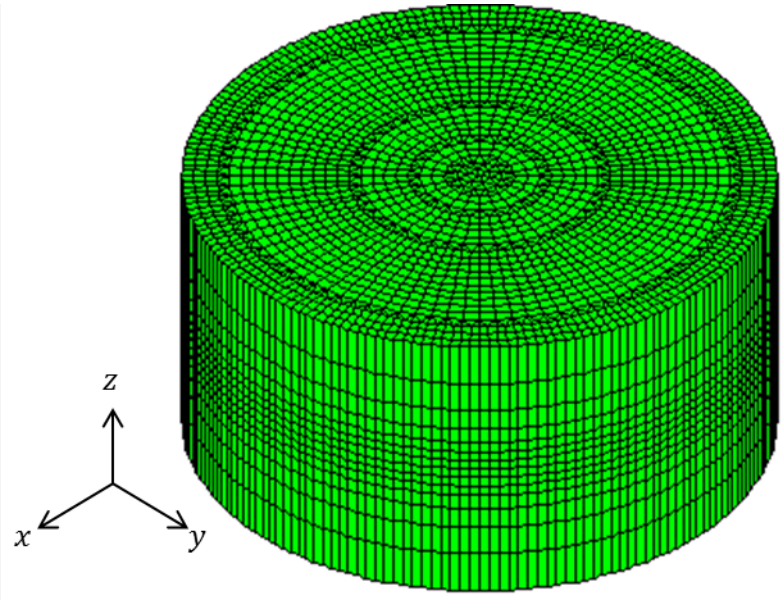

Figure 3.1: Mesh of the model in PROMETHEUS for $\zeta_f = 1mm$ and $\zeta_c = 4mm$.

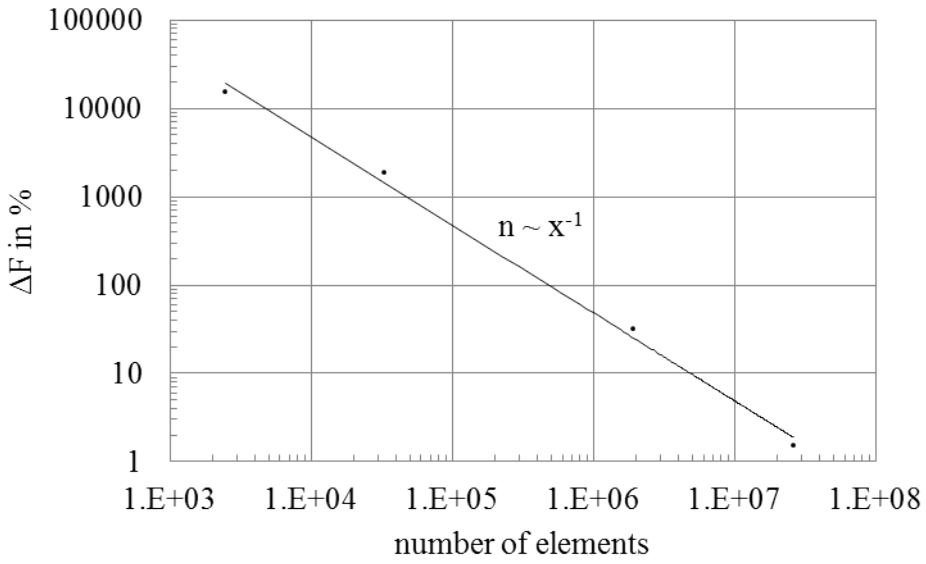

Figure 3.2: Comparison of analytic to numerical results of the Lorentz force for different grids (h=0.005R) in Prometheus.

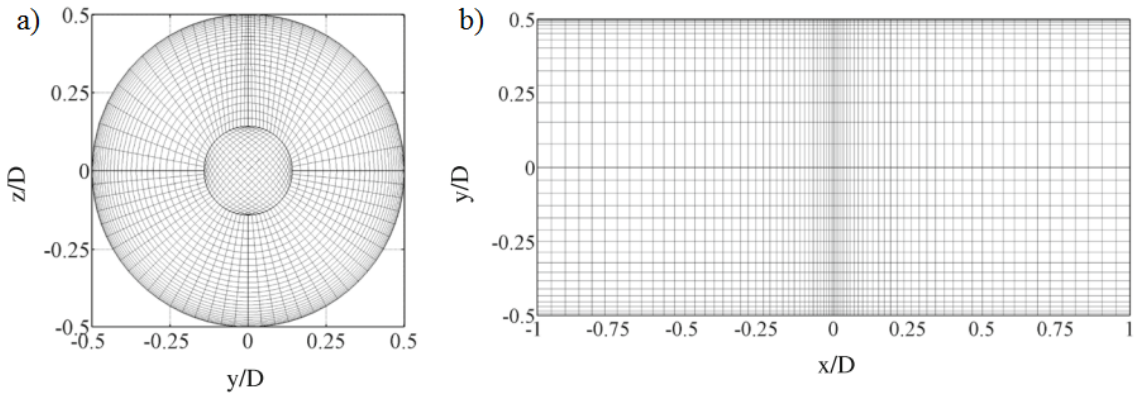

Figure 3.3: Typical structure of a mesh used for numerical simulations in [8] with small distances between dipole and cylinder surface; a)cross-section view, b) top view. The cylinder axis is oriented along the x-axis, which differs in this work.

mesh parameters $\zeta_f = 0.4mm$ and $\zeta_c = 1.6mm$ for the finely and coarsely meshed regions of the cylinder. The results of the length study are listed in Tab. 3.3. The Lorentz force in the cylinder of length $L = 10(h + R) = 500mm$ is used as the reference value for calculating the Lorentz force deviation in smaller cylinders. The mesh convergence study was done with a length $L = 7(h+R)$ which differs by 0.011% from the reference value. During the optimization procedure a cylinder length of $L = 5(h+R)$ was chosen, since an error of 0.028% with regard to the reference value is acceptably small compared to the reduction in computation time for one function evaluation.

L in mm	$error$ in %
$10(h + R) = 500$	–
$7(h + R) = 350$	0.011
$6(h + R) = 300$	0.021
$5(h + R) = 250$	0.028
$4(h + R) = 200$	0.029
$3(h + R) = 150$	0.242
$2(h + R) = 100$	4.077

Table 3.3: Parameter study for the length of the cylinder.

Mesh Study COMSOL

[8] use a structured mesh for their convergence study (fig. 3.3). The region underneath the single dipoles is meshed very finely to provide the necessary resolution to display the strong gradients of the magnetic field. Farther away from this region the mesh is coarser and the elements are very stretched. While this mesh is well suited for a single dipole, it does not adequately resolve multiple dipoles placed around the cylinder, which is in the focus here. The strongly stretched mesh elements distort the physical fields leading to a high error and unreasonably long computation time.

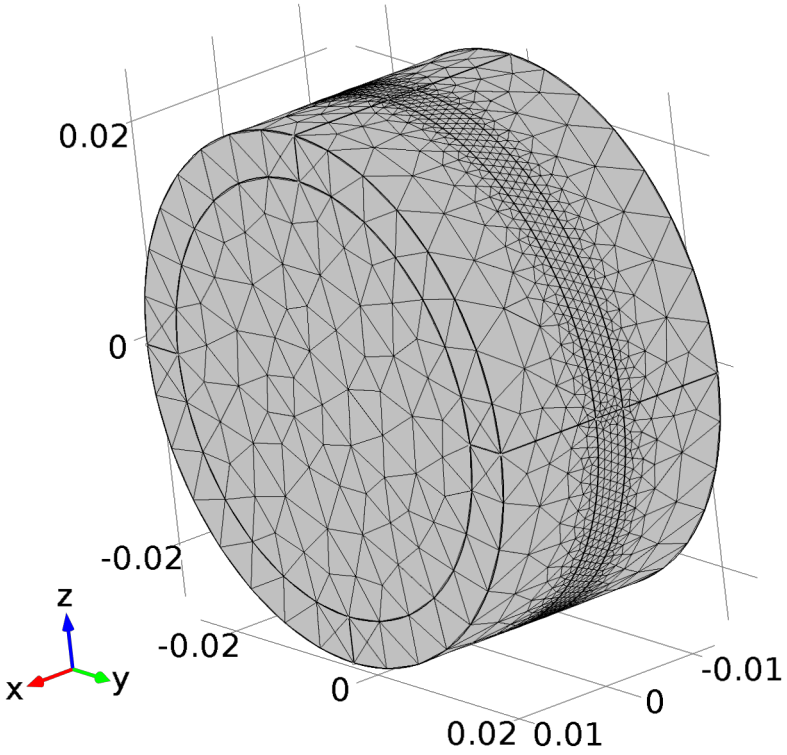

Figure 3.4: COMSOL mesh for the convergence study. The outer middle region is more sensitive because of its closeness to the dipole and needs to be meshed finer.

Here, the cylinder is meshed with tetrahedral elements (fig. 3.4). This permits for very finely meshed regions in the center of the cylinder, where field gradients are high, while the elements grow more regularly in size in the remaining domain (fig. 3.4). The outer part of the middle region of the cylinder has a finer mesh. Its length is $l/8$ and the radius of the inner circle is $4R/5$. Tb. 3.4 lists the mesh parameters. The elements of the finer sensitive region vary from a maximum element size of $3 \cdot 10^{-3}m$ to $1 \cdot 10^{-3}m$. The minimum elements size is kept constant at $1 \cdot 10^{-6}mm$, while the default settings for $extremely fine$ are used for all other parameters. The remaining domain is meshed with the predefined *normal* setting.

Fig. 3.5 displays the convergence plot for the COMSOL model which uses second-order elements. Compared with [8] the numerical results do not converge as quickly to the analytic solution. They used only one dipole and needed to refine the mesh in one specific region, whereas the distribution of multiple dipoles requires a finer grid all around the cylinder. As such a higher number of mesh elements are needed to archive a good convergence. Thus, while the total number of mesh elements is higher than in [8], the convergence is slower.

remaining domain	sensitive domain max. element size in mm	number of elements	F/F_0	ΔF
	0.30	1517966	2.1770	63.2757
	0.25	2566067	1.8080	35.6046
normal	0.20	4847789	1.6437	23.2796
	0.15	11143757	1.4820	11.1536
	0.12	21386495	1.3815	3.6152

Table 3.4: Parameters for the grid in COMSOL for one dipole placed very close to the cylinder surface.

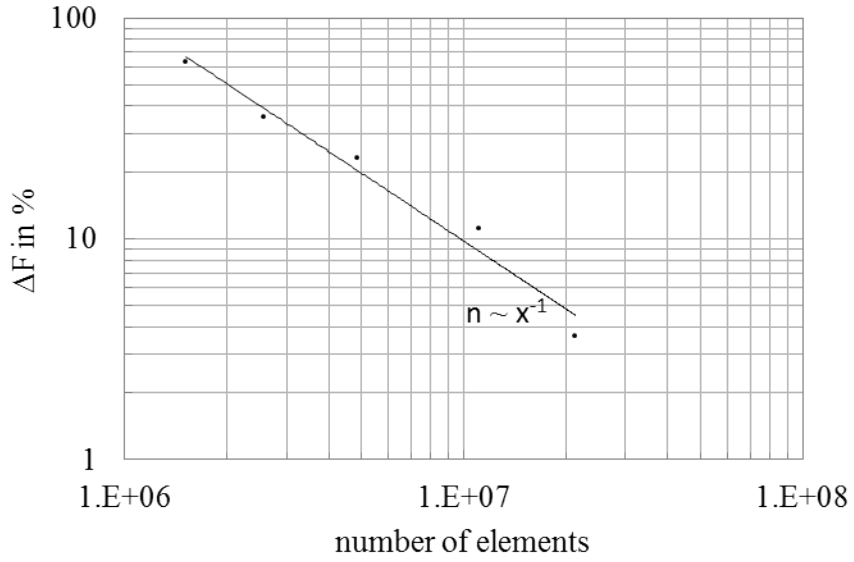

Figure 3.5: Convergence plot for mesh refinement study in COMSOL for one dipole for the close approximation. Second-order elements are used.

Chapter 4

Dipoles - Analytic Approximation

Chapter 2 introduced the physical background of Lorentz force velocimetry and the expression for the Lorentz force was derived for the special quasi-static case of a weakly conducting medium moving with a plug like profile in a pipe. However, an analytic solution for arbitrary magnetic field sources is not attainable. The difficulty lies in the calculation of the electric potential ϕ inside the pipe. Even with all the applied simplifications the analytic derivation of ϕ can only be done with further approximations. There are two limiting cases for an analytic formulation for dipoles. Either the dipole is very close to the surface of the cylinder or very far away. Investigations were made with one single dipole placed very close to a moving conducting plane [59], [43] or far away from a moving square bar [26] and a translating and rotating cylinder [8]. In this work multiple dipoles are put around a pipe and the orientation of the magnetic dipole moments is optimized which has not been done before. The use of multiple dipoles gives insight into the optimal configuration and flow of the magnetic flux density. Conclusions can be drawn from these results and adapted for a realistic and practical magnet system for Lorentz force velocimetry.

Dipoles are the simplest expression for magnetic field sources. They produce the following magnetic flux density at the point $\vec{r'}$ (fig. 4.1):

$$\vec{B}(\vec{r'}) = \frac{\mu_0}{4\pi} \frac{3\vec{r'}(\vec{m} \cdot \vec{r'}) - \vec{m}r'^2}{r'^5}. \tag{4.1}$$

$\vec{r'}$ is the position vector and r' its magnitude $|\vec{r'}| = ((x - H_x)^2 + (y - H_y)^2 + (z - H_z)^2)^{(1/2)}$. $\vec{m} = (m_x, m_y, m_z)$ is the magnetic dipole moment. $\vec{r'} = \vec{r} - \vec{H}$ can be expressed by the distance vector $\vec{H}$ [1] from the origin to the dipole and the vector $\vec{r}$ pointing from the origin to the position vector $\vec{r'}$ (fig. 4.1).

Here the asymptotic approximation developed by [26] is extended to include more dipoles placed at a fixed distance H in a plane perpendicular to the cylinder surface. The derivation for arbitrary positions was unsuccessful.

The approximation for large distances uses a long-wave expansion in the axial coordinate z. Since the dipole is very far away from the cylinder the magnetic flux

[1] The distance vector $\vec{H}$ should not be confused with the magnetic field $\vec{H}$. The meaning can be inferred from context.

density $\vec{B}$ varies slowly in z while the other parameters vary on the scale of the cylinder radius R. This disparity in length scales can be exploited by a regular perturbation expansion [67] in the small parameter $\varepsilon = \frac{R}{H} \ll 1$. For this the cartesian coordinates need to be rescaled:

$$x = R\hat{x} \qquad y = R\hat{y} \qquad z = H\hat{z}. \tag{4.2}$$

In the following chapters the regular perturbation theory is used to derive the Lorentz force for the small parameter ε, which is used to verify the numerical FEM model.

4.1 Analytic Lorentz Force

Regular perturbation theory [67] is a type of perturbation theory, where the effects of small disturbances are small[2]. It is used when a mathematical problem cannot be solved exactly. In this case an approximate solution is obtained by utilizing a small dimensionless parameter. The smaller the parameter the more accurate is the approximate solution.

The physical values $\vec{B}$, ϕ, $\vec{J}$ and $\vec{F}$ expressed with the rescaled coordinates are expanded to function series depending on the small parameter $0 < \varepsilon \ll 1$ where R and H are constant. The upper indices in brackets indicate the number of the term of the expansion. They coincide with the power of ε.

Magnetic flux density:

$$\vec{B} = \vec{B}^{(0)} + \varepsilon\vec{B}^{(1)} + \varepsilon^2\vec{B}^{(2)} + ... + \varepsilon^n\vec{B}^{(n)} + o(\varepsilon^n) \tag{4.3}$$

Eddy currents:

$$\vec{J} = \vec{J}^{(0)} + \varepsilon\vec{J}^{(1)} + \varepsilon^2\vec{J}^{(2)} + ... + \varepsilon^n\vec{J}^{(n)} + o(\varepsilon^n) \tag{4.4}$$

Electric scalar potential:

$$\phi = \phi^{(0)} + \varepsilon\phi^{(1)} + \varepsilon^2\phi^{(2)} + ... + \varepsilon^n\phi^{(n)} + o(\varepsilon^n) \tag{4.5}$$

Lorentz force:

$$\vec{F} = \vec{F}^{(0)} + \varepsilon\vec{F}^{(1)} + \varepsilon^2\vec{F}^{(2)} + ... + \varepsilon^n\vec{F}^{(n)} + o(\varepsilon^n) \tag{4.6}$$

Furthermore the rescaled coordinates are inserted into the vector differential operator:

$$\nabla = \begin{pmatrix} \partial_x \\ \partial_y \\ \partial_z \end{pmatrix} = \begin{pmatrix} \frac{1}{R}\partial_{\hat{x}} \\ \frac{1}{R}\partial_{\hat{y}} \\ \frac{1}{H}\partial_{\hat{z}} \end{pmatrix} = \begin{pmatrix} \frac{1}{R}\partial_{\hat{x}} \\ \frac{1}{R}\partial_{\hat{y}} \\ \frac{\varepsilon}{R}\partial_{\hat{z}} \end{pmatrix} = \frac{1}{R}\begin{pmatrix} \partial_{\hat{x}} \\ \partial_{\hat{y}} \\ \varepsilon\partial_{\hat{z}} \end{pmatrix}$$

and the laplace operator:

$$\Delta = \nabla \cdot \nabla = \frac{1}{R}\begin{pmatrix} \partial_{\hat{x}} \\ \partial_{\hat{y}} \\ \varepsilon\partial_{\hat{z}} \end{pmatrix} \cdot \frac{1}{R}\begin{pmatrix} \partial_{\hat{x}} \\ \partial_{\hat{y}} \\ \varepsilon\partial_{\hat{z}} \end{pmatrix} = \frac{1}{R^2}(\partial_{\hat{x}}^2 + \partial_{\hat{y}}^2 + \varepsilon^2\partial_{\hat{z}}^2).$$

[2]Otherwise, they are termed singular

With the rescaled coordinates and expansions a solvable analytic expression for the Lorentz force can be derived analogous to [26] and [8]. The complete, step by step derivation can be found in appendix A.

The necessary steps are shortly summarized here. First, the expanded values (eq. 4.3-4.6) are inserted into eq. 2.1-2.4 and the boundary conditions of the electric scalar potential eq. 2.19 are used to derive $\phi^{(0)}$. Second, the boundary conditions (eq. 2.18) and the divergencelessness of the eddy currents (eq. 2.7), with the help of the stream function (eq. A.9) and its characteristics, lead to an expression for $\vec{J}$. Then the Lorentz force (eq. A.19) can be derived, which consists of predefined parameters $\xi = (\sigma, v_{\hat{z}}, R, h, m)$ and an integral containing the derivatives of the magnetic field components containing the optimization variables $\vec{x} = (\mu, \nu, \gamma)$ (fig. 4.1):

$$F_a(\xi, \vec{x}) = -\frac{\pi\sigma v_{\hat{z}} R^4}{8H} \int_{-\infty}^{+\infty} 2[(\partial_{\hat{z}} B_x^{(0)})^2 + (\partial_{\hat{z}} B_y^{(0)})^2] + (\partial_{\hat{z}} B_z^{(0)})^2 d\hat{z}. \tag{4.7}$$

This is the objective function which is optimized for an varying number of dipoles in chapter 6, the subscript a indicates the analytic expression of the Lorentz force F. The components of the magnetic field produced by multiple dipoles $i = 1, 2, ..., n$ are the sum of each individual contribution, i.e.

$$B_{\hat{x}}^{(0)} = \sum_{i=1}^{n} B_{ix}^{(0)}, \quad B_{\hat{y}}^{(0)} = \sum_{i=1}^{n} B_{iy}^{(0)}, \quad B_{\hat{z}}^{(0)} = \sum_{i=1}^{n} B_{iz}^{(0)}.$$

With this derivation the FEM models are verified for one dipole. In chapter 6 the number of dipoles is increased and the respective Lorentz force is optimized.

4.2 Verification of Numerical FEM Model

A variety of setups with one dipole were already studied, by [59] (one fixed orientation, close to surface), [43] (dipole oriented along the three axes, close to surface), [26] (asymptotic approximation, bar) and [8] (asymptotic approximation, cylinder). All these studies have in common that they use only a single dipole. In this chapter the numerical results of [8] are reconstructed, since they also use a cylinder, to verify the used numerical FEM models. [8] used COMSOL Multiphysics for their numerical analysis. Licenses of this commercial software are very expensive and limit the number of program calls. Therefore, the results are compared with the results attained with the in-house code PROMETHEUS to assess applicability, whose usage is not restricted like COMSOL.

As will be seen in chapter 6, a complete analytic optimization of this simplified problem is limited by the number of dipoles, i.e. number of optimization variables. However, while a numerical optimization of this simplified problem is possible, i.e. the derived objective function is numerically optimized, the extension to arbitrarily placed dipoles is not. This obstacle can only be overcome with complete numerical calculation. Two FEM simulation software programs are used here, the in-house code PROMETHEUS [35] and the commercial code COMSOL Multiphysics [10].

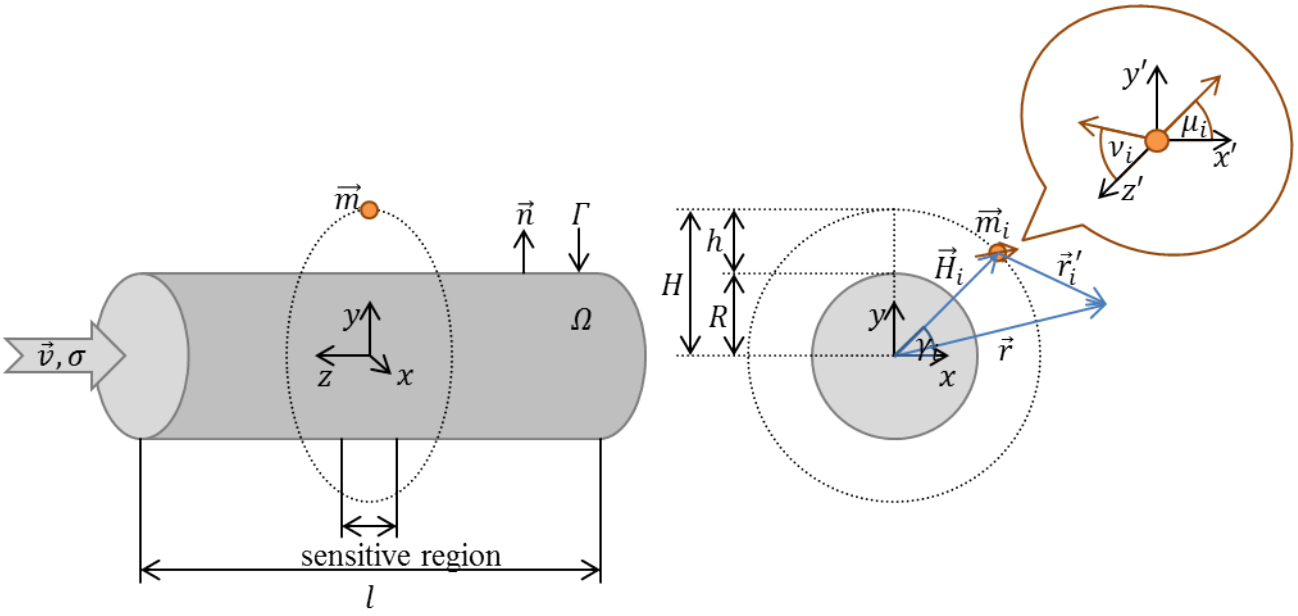

Figure 4.1: Geometrical dimensions of the dipole problem setup with the sensitive region which is meshed finer to better resolve field gradients and cross section view of the xy plane. The position of the dipoles $\vec{m}_i$ is fixed to a specific distance $\vec{H}_i$ in the $z = 0$ plane. The orientation of the magnetic moments are given by the spherical coordinates μ_i and ν_i. The magnetic field created by $\vec{m}_i$ at $\vec{r'}_i$ is expressed with eq. 4.1. h is the distance of the dipole from the surface of the cylinder and H the distance from the dipole to the origin. The cylinder has the radius R, length l, conductivity σ and velocity $\vec{v}$

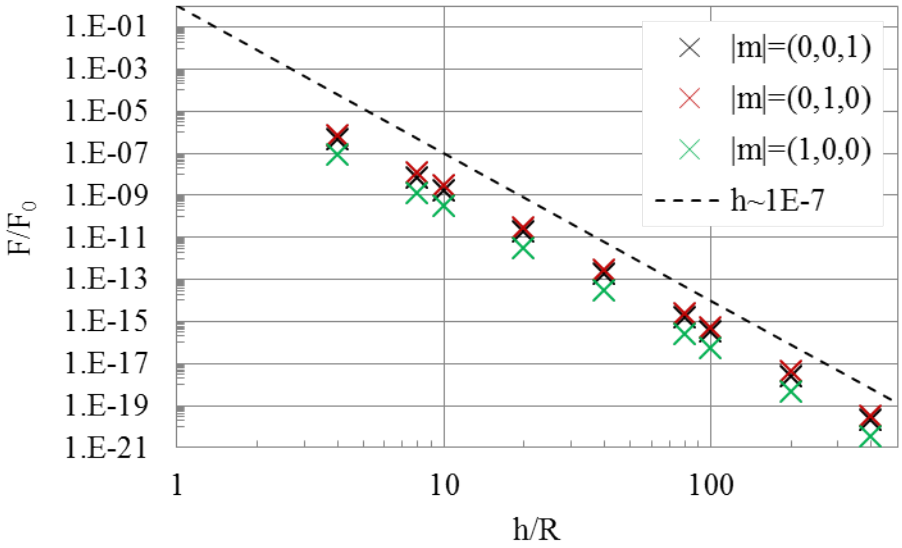

Figure 4.2: Nondimensionalized Lorentz force as a function of the distance h between one dipole oriented in $|m|$ direction and the cylinder surface of a moving pipe.

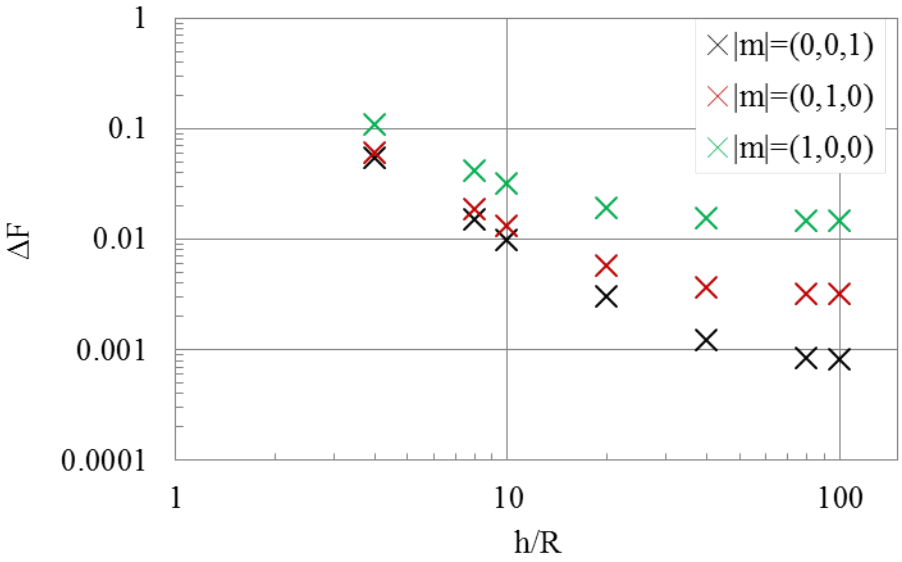

Figure 4.3: Relative error ΔF between analytic results and numerical results from PROMETHEUS.

In this chapter the derived analytic formulation of the Lorentz force (eq. 4.7) for the asymptotic approximation of one dipole is compared to the numerical results provided by PROMETHEUS and COMSOL. Consistently with [8] three different orientations of the single dipole are investigated. Fig. 4.1 depicts the geometrical dimensions. The dipole is fixed along the three coordinate axes x, y and z, respectively. Its distance to the cylinder is set to $h = 0.125mm$ for a mesh refinement study or is increased from $h/R = 4$ to 100 to determine the dependency on the distance. h is the distance of the dipole from the surface of the cylinder and R is the cylinder radius. With a ratio of $h/R = 100$ the dipole is at a distance of $H = 2.525m$ from the center of the cylinder.

For better comparison of the results the simulated Lorentz force is nondimentionalized with the following reference value [60]:

$$F_0 = \sigma v \mu_0^2 m^2 L^{-3}$$

m is the absolute value of the magnetic dipole moment and $L = R$ is the characteristic length which equals the radius of the cylinder. Inserting the following values[3] for the parameters:

$$\sigma = 3.85 \cdot 10^7 S/m \qquad v = 0.82678 m/s \qquad m = 3.5 Am^2 \qquad L = 25mm$$

gives:

$$\Rightarrow F_0 = 39.41N.$$

[3]The cited values were taken from [8] to make for better comparability. Contrary to their work, the focus here lies on weakly conducting fluids, meaning a electric conductivity of $\sigma < 10 S/m$. The quasi-static approximation (chapter 2.2.2 still holds, because of the small product of vL^{-3}.

h	number of	F_n/F_0			$\Delta F \cdot 10^{-3}$		
in cm	elements	$(m_x, 0, 0)$	$(0, m_y, 0)$	$(0, 0, m_z)$	$(m_x, 0, 0)$	$(0, m_y, 0)$	$(0, 0, m_z)$
10	617760	4.4010^{-07}	6.9410^{-07}	7.8010^{-08}	54.26	59.79	108.84
20	1233180	6.9210^{-09}	1.0910^{-08}	1.2010^{-09}	14.83	18.42	40.99
25	1605240	1.6910^{-09}	2.6610^{-09}	2.9110^{-10}	9.83	13.08	31.73
50	3004560	1.8210^{-11}	2.8610^{-11}	3.1110^{-12}	2.99	5.66	18.80
100	6891300	1.6810^{-13}	2.6410^{-13}	2.8610^{-14}	1.21	3.66	15.35
200	10801440	1.4310^{-15}	2.2410^{-15}	2.4410^{-16}	0.83	3.19	14.70
250	12397320	3.0410^{-16}	4.7910^{-16}	5.2010^{-17}	0.81	3.15	14.70

Table 4.1: Lorentz force depending on the distance to the cylinder surface h.

If the distance between dipole and cylinder is of the same size as the cylinder radius $h \approx R$ or larger then the field gradients (of the magnetic flux density, eddy currents, etc.) do not vary as strongly in the cross section of the cylinder. Thus the high resolution of the mesh of the cross section can be reduced. This is essential since the farther away the dipole is located the longer the moving object needs to be to ensure sufficient decay of the field towards its ends to eliminate effects due to finite length. For $h/R > 1$ the size of the mesh elements are increased and higher values are used for the parameters ζ_f and ζ_c. Simultaneously, the axial length l of the cylinder is increased. A systematic variation determined $l = 5h$ to be adequate for a specific dipole distance h.

For the dependence of the dipole distance to the cylinder surface h is varied from $0.1m$ to $12.5m$. For $l = 12.5m$ the integrated Lorentz force converges to an satisfying value for a mesh of $\zeta_f = 0.4mm$, $\zeta_c = 1.6mm$. However, the resulting number of total mesh elements requires to much computational resources. The difference between this converged Lorentz force and the one with the mesh parameters $\zeta_f = 1mm$, $\zeta_c = 4mm$ is less than 2%. This is an acceptable deviation and good choice for the calculations. Tb. 4.1 displays all data points for a mesh of $\zeta_f = 1mm$, $\zeta_c = 4mm$. The mesh does not stretch along with increasing l, but the number of elements grows with l. When l is small PROMETHEUS needs less memory and finer meshing would be possible.

Fig. 4.2 shows the development of the Lorentz force depending on the distance from the cylinder surface h. Near $h/R \approx 1$ the dependency of the distance of the dipole transitions between the asymptotic approximation and the close approximation $h \ll R$. In the close approximation, the dipole is very near the translating conductor [59] (vertical dipole orientation, only) and [43] (arbitrary dipole orientation). This branch for $h/R < 1$ is not reconstructed with numerical data, because here the analytic multi-dipole study (chapter 5) is limited to the asymptotic case.

The analytic Lorentz force (eq. 4.7) for one dipole (eq. 4.1) for the asymptotic approximation is:

$$F_a = \frac{\mu_0^2 R^4 \sigma v}{131072 H^7}(4275m_x^2 + 720m_y^2 + 6705m_z^2). \tag{4.8}$$

The numerical results agree well with (eq. 4.8) for large h and different dipole orientations. With increasing h/R the Lorentz force gets closer to the asymptotic solution confirming the power law $F \sim h^{-7}$.

Fig. 4.3 depicts the relative error (eq. 3.3) between analytic and numerical values for all dipole orientations. They are in the range of previous work of [8], but show a different behavior. The relative error of the Lorentz force for the different dipole orientations show small variations, and while the overall error values are lower, they stagnate for $h/R > 40$, which is not the case in [8]. This might be due to numerical uncertainties.

Chapter 5

Optimization

This chapter gives an overview of the optimization procedure. It formulates the optimization problem and introduces the used optimization procedures and algorithms. Finally, it summarizes the optimization variables of the different setups.

5.1 Introduction

Optimization plays a very important role in the field of engineering. A lot of energy and effort are put into finding optimal cost-benefit ratio, production processes, techniques, etc. [45], [56]. The goal is to find the values for one or several decision variables that minimize or maximize one or more objectives, which may be subjected to constraints.

There is a wide variety of optimization algorithms ranging from relatively simple heuristic [20] to complex global [23] methods. Some require a lot of information like the analytic objective function, its derivatives and even hessian matrix. Others, so called black box algorithms [3], only need the input parameters and the corresponding value of the objective function delivered by some kind of numerical model. All of them are suited for different problems, which exploit their respective advantages and disadvantages. Many optimization algorithms and especially the heuristic methods produce only local extrema of the objective functions. Fortunately, in the field of engineering it is often enough to find an acceptable improvement of the current situation, especially if the time of the optimization process is also considered important [44]. The final result is in the foreground and the algorithm only a tool. This is in contrast to mathematics, where the optimal solution is often known and the main focus is on the methods to derive this solution.

In this work, different optimization types are used in the study of the multi-dipole problem. The goal is to find the optimal setup of magnetic field sources in the framework of LFV. The following chapter gives an overview of the methods and algorithms which are applied to the different setups in chapter 6.

5.2 Formulation of the Problem

The most basic formulation of an optimization problem for the objective function $f(x) : \mathbb{R}^k \rightarrow \mathbb{R}$ with the decision variables $x = (x_1, x_2, ..., x_k)$ belonging to the feasible set $G \subset \mathbb{R}^k$ is:

$$\begin{aligned} & f(x) \longrightarrow \text{ min (max)} \\ \textit{subject to} & \\ & x \quad \in \quad G. \end{aligned}$$

Conventionally this function is minimized. However a change in sign converts a minimization into a maximization problem and vice versa:

$$\min f(x) = \max -f(x).$$

One can adapt the formulation to aid in the understanding of a specific problem. In the field of engineering it is more intuitive to talk about finding maxima instead of minima, when a physical quantity is supposed to be actually maximized.

The nature of $f(x)$ and G classify the optimization problem and determine the appropriate optimization method. Important characteristics are for example linearity, monotony convexity and differentiability [15], multi-objectivity, discretness of variables, constraints, etc [42]. The more good-natured the optimization problem and especially the objective function is the better can an optimization algorithm be formulated to fit the task and most importantly the more successful the results will be. Good-natured are functions which are differentiable, convex, etc, which provide the algorithm many useful properties to consider. If the optimization problem is not good-natured, high demands are put on the optimization method.

The variable x^* is a local maximizer if there exists a neighborhood U of x^* such that x^* produces the highest value of $f(x)$ in x^* compared to all $x \in U \cap G$. This neighborhood U is an open set containing x^*:

$$f(x^*) \geq f(x) \qquad \text{for } x \in U.$$

x^* is a global maximizer if it archives the highest value of $f(x)$, where x ranges over the domain of interest:

$$f(x^*) \geq f(x) \qquad \forall x \in G.$$

The maximizer is unique if the inequality is strict:

$$f(x^*) > f(x) \qquad \text{for } x \in G \setminus \{x^*\}.$$

The analytic part of the asymptotic dipole problem is non-linear, smooth and differentiable with multiple decision variables limited by box constraints. The feasible set has upper and lower bounds:

$$lb \leq x \leq ub.$$

The fundamental steps of a numerical optimization algorithm are as follows [42]:

- A starting point x^0 is supplied based on user knowledge or some other arbitrary manner.
- The objective function $f(x^c)$ and its characteristics (like derivative, monotonity, ...) are evaluated at the current x^c and even former iterates $x^0, x^1, ..., x^{c-1}$.
- The selected strategy, i.e. line search, trust region,... generates the next iterate x^{c+1} based on the information gained from $f(x)$.
- A stopping criterion prescribes when this sequence terminates.

The next chapter explains the analytic optimization of an objective function.

5.2.1 Analytic Optimization

The analytic expression for the multi dipole problem which is derived from eq. A.19 is a smooth function and depends on the parameters $x = (x_1, x_2, ..., x_i, ..., x_k)$. It can be analytically optimized as follows:

- The first derivatives of the objective function are taken with respect to all x_i and set to zero:
$$\frac{\partial f(x)}{\partial x_i} = 0. \tag{5.1}$$
- The critical points x_{crit} are calculated which satisfy eq. 5.1.
- The Hessian matrix of the objective function is derived. The Hessian contains the second derivatives of $f(x)$ and determines the character of the critical points:
$$\mathcal{H}_f(x) = \left(\frac{\partial^2 f(x)}{\partial x_i \partial x_j}\right)_{i,j=1,...,k} = \begin{pmatrix} \frac{\partial^2 f(x)}{\partial x_1 \partial x_1} & \cdots & \frac{\partial^2 f(x)}{\partial x_1 \partial x_k} \\ \vdots & \ddots & \vdots \\ \frac{\partial^2 f(x)}{\partial x_k \partial x_1} & \cdots & \frac{\partial^2 f(x)}{\partial x_k \partial x_k} \end{pmatrix}.$$
A twice continuously differentiable multivariable function is independent of the order in which the derivatives are taken according to Young's theorem [2]:
$$\frac{\partial^2 f(x)}{\partial x_i \partial x_j} = \frac{\partial^2 f(x)}{\partial x_j \partial x_i}$$
meaning that the Hessian $\mathcal{H}_f(x)$ is symmetric. It is positive/negative definite if the leading principle minors are positive/negative or the eigenvalues are greater/smaller than zero. The Hessian is evaluated at the critical points $f(x)$ and the definite quadratic form of the Hessian is calculated.
- Hessian is positive definite $\Rightarrow x^{crit}$ is a unique local minimum
- Hessian is negative definite $\Rightarrow x^{crit}$ is a unique local maximum
- Hessian is semi-definite or indefinite $\Rightarrow$ assertion is not possible

- Calculation of the values of the objective function belonging to the respective local extrema which reveals the global optimal solution.

This process is done with the symbolic calculation software MATHEMATICA and only with the analytic dipole problem (chapter 3) with a small number of dipoles (chapter 6.1). As the number of dipoles increases MATHEMATICA is not able to calculate the critical points anymore. Thus, more complex setups are optimized numerically (chapters 6.2 and 6.3) via the MATLAB optimization toolbox [38] for a large number of dipoles.

5.2.2 Nelder-Mead Simplex Direct Search

The most successful optimization algorithm from the MATLAB optimization toolbox [38] in the context of this work is the Nelder-Mead simplex direct search method (NMSDS). This chapter describes this method in more detail.

J. A. Nelder and R. Mead introduced this heuristic algorithm in 1965. It impresses with a simple and robust character, making it easy to use and implement [40], [37]. While modern methods are more sophisticated, it enjoys popularity in engineering [36], physics [16] and finance [53], to name just a few and it is still object of current research [18], [29].

NMSDS is a direct search method, meaning that it does not use the derivative of a function, but evaluates the objective function values to determine the next possible iterate. This makes the algorithm well suited for problems without access to a gradient, i.e. $f(x)$ is provided by a black box simulation, the exact first derivatives are difficult to compute, etc. A consequence of this is that it converges slower compared to the methods which use gradients [30] and it might converge to a non-stationary point [39].

The objective function $f(x) : \mathbb{R}^k \rightarrow \mathbb{R}$ can be non-linear and depends on k variables, without constraints. The corresponding simplex $\mathcal{S}$ on which this method is based is a polyhedral with $k+1$ vertices $x^0, x^1, ..., x^{k+1} \in G$. The set $\{x^k - x^j | k \in \{1, ..., k+1\} \setminus \{j\}\}$ is linear independent in $\mathbb{R}^k$. The simplex adjusts itself to the local form of the objective function according to three methods: reflection, expansion and contraction (fig. 5.1). The algorithm passes through the following steps:

1. The function values at the vertices of the simplex are compared and sorted from the point x^w with the worst function value $f(x^w)$ to x^b with the best function value $f(x^b)$. Here, the worst and best function values are the respective minimal and maximal function values.

2. x^w is then reflected to x^* with regard to the centroid of all other vertices x^i with $i \neq w$ (fig. 5.1). The function value $f(x^*)$ determines the next action:

   If $f(x^w) < f(x^*) < f(x^b)$ then x^* is the new vertex of the simplex, replacing x^w and continue to step 3.

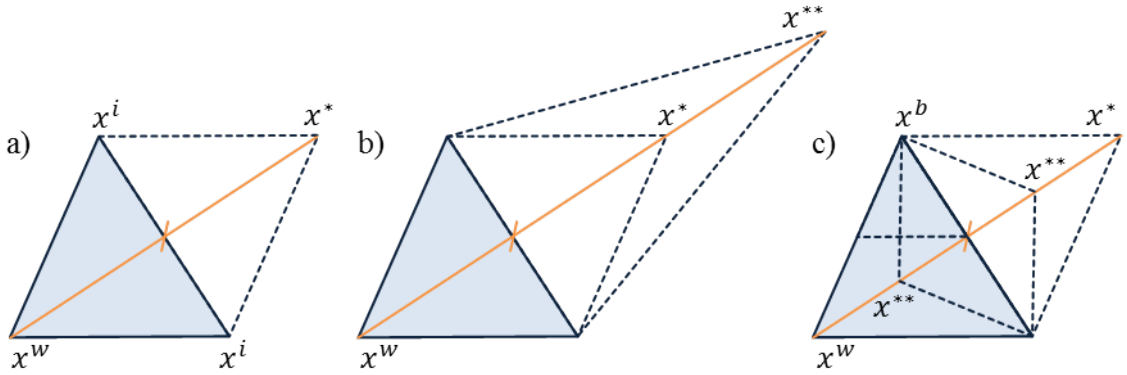

Figure 5.1: Generation of a new iterate x^* in the Nelder-Mead simplex direct search method with a 2D simplex: a) reflection, b) expansion, c) contraction based on [19].

If $f(x^b) < f(x^*)$ then x^* is further extended to the point x^{**} (fig. 5.1), which is used as the new iterate if $f(x^b) < f(x^{**})$ otherwise it is x^* and continue to step 3.

If $f(x^*) < f(x^i) \forall i \neq w$ then $f(x^*)$ is always the minimum and the simplex is contracted with respect to the centroid. Should this point be again worse then all x^i are moved and continue to step 3.

3. Repeat from step 1 until the stopping criterion is meet.

The following optimality conditions are necessary for the NMSDS method, assuming that $f(x)$ is once differentiable:

$$\begin{gathered} f(x) \text{ has a local maximum at } x^b \in G \\ \Longleftrightarrow \text{ There is a ball } \mathcal{B}(x) \text{ around } x^b \\ \text{such that } f(x) \leq f(x^b) \forall x \in G \cap \mathcal{B}(x) \\ \Rightarrow \frac{\partial}{\partial x_i} f(x^b) = 0, i = 1, 2, ..., k. \end{gathered}$$

$f(x)$ has to be twice differentiable for the sufficient conditions:

$$\begin{gathered} \frac{\partial}{\partial x_i} f(x^b) = 0, i = 1, 2, ..., k \text{ and} \\ \mathcal{H}_f(x^b) = \left(\frac{\partial^2}{\partial x_j \partial x_i} f(x^b) \right)_{kk} \text{ is positive definite} \\ \Rightarrow f(x) \text{ has a unique local maximum at } x^b \in G. \end{gathered}$$

Compared with other methods, especially ones that use gradients, NMSDS does relativly well when there are great differences in the function values, but suffers when it closes on an optimum, leading to a slow convergence [30]. This is not a disqualifying factor in the field of engineering and particularly when simulations with numerical errors are considered. It is already satisfactory to reach a better result than the given one.

5.2.3 Gradient-Ascent Method

PROMETHEUS uses a simple, build-in gradient method [42] for optimization procedures, enabling parallel computation which reduces computation time.

The gradient method also called steepest-ascent is a line search algorithm. Line search methods determine a direction p_c and then move a step size α_c in this direction. The steepest-ascent method uses the gradient as the direction $p_c = \nabla f(x^c)$ to a local maximum. Requirement is that the objective function $f(x)$ is differentiable. PROMETHEUS numerically calculates $f(x)$ at the current point x^c and numerically determines the gradient $\nabla f(x^c)$. The algorithm then goes in the direction of the gradient to determine the new iterate x^{c+1}.

$$x^{c+1} = x^c + \alpha_c \nabla f(x^c).$$

The step size α_c determines the distance traveled along the direction of the gradient. PROMETHEUS starts with a user defined step size and an integer value u specifying how many times α_c moves along the gradient. For each time the objective function $f_i(x^c + i\alpha_c)$ is calculated with $i = [1, u]$. The best function value determines the step size for the next iteration $\alpha_{c+1} = i\alpha_c$. The u function evaluations are done in parallel computation, allowing for a more efficient optimization.

The starting step size for all gradient-ascent optimizations is $\alpha_c = 1 \cdot 10^8$ and $u = 8$.

The steepest-ascent method is a local optimization algorithm and there is no guarantee that it will find global maxima, however it is able to leave local maxima.

5.2.4 Non-linear Optimization by Mesh Adaptive Direct Search

Engineering and industrial problems are real life problems and as such they bring along several difficulties. With the help of simulations one can relatively cost efficiently analyze a problem and of course optimize it. A special area in the methodology of optimization are so called black box problems [3]. They present a field which is characterized by very specific attributes.

In black box optimization the objective functions are computed via computer simulations, where one evaluation is usually computationally heavy, time consuming, or the results might have a low quality, i.e. are affected by numerical noise or inaccuracies. They are termed black-box, because the user provides only the input data and then receive an output.

Usually one cannot access the internal structure of the problem, making the determination of a gradient time consuming and not feasible. Thus, derivative free methods are used without assuming anything about the objective function or the admissible region. Only the values for the set of variables can be provided as an input. Based on the resulting output value of the objective function, the next input variables are determined.

The commercial FEM simulation software COMSOL Multiphysics does not provide the gradient of the objective function nor does it allow access to its source code,

in order to numerically derive it and one function evaluation is computationally expensive. Thus, it can be termed as a black box problem.

Non-linear optimization by mesh adaptive direct search (NOMAD) [31], [4] is the black box algorithm applied in the optimization of the COMSOL problem of this work. NOMAD is a software based on a constrained mesh adaptive direct search (MADS) algorithm. It handles single- and bi-objective problems, considers general inequality constraints and continuous, integer or binary decision variables.

Direct search methods search the space of variables systematically for maxima. Their only clue is the function evaluation provided by the numerical model. MADS algorithms are a more sophisticated form of direct search methods [33], [27] with a detailed convergence theory based on non-smooth calculus. This iterative method discretises the space of variables on a mesh which is refined if necessary.

Each iteration is composed of a $SEARCH$, and $POLL$ step. The $SEARCH$ step tries to find a better solution on the mesh. Previously evaluated points are stored which avoids double evaluations. Should the $SEARCH$ step be unsuccessful then the $POLL$ step starts. It explores the mesh near the current best solution with a set of trail points. The convergence analysis relies on the $POLL$ step which is consequently more strictly defined. If a better solution than the current iterate has been found then the mesh is coarsened otherwise it is refined and the procedure repeats itself until the stopping criteria is met.

5.3 Defining the Geometric Setup and Optimization Variables

The geometric setup of the multi-dipole problem is as follows: a cylinder representing the conductive medium is surrounded by dipoles (fig. 4.1). The center of mass of the cylinder lies in the origin and its axis aligns with the z-axis. Now that the expression for the Lorentz force for this problem is derived (eq. 4.7), it can be used to analytically calculate different configurations of dipoles. The dipoles are located on a circular ring in a plane perpendicular to the center of the cylinder. A derivation for arbitrary distances $\vec{H}$ was not successful. The orientation of the $i = 1, 2, ..., n$ dipoles depends on spherical coordinates, i.e. the polar angle μ_i and the azimuthal angle ν_i. The principle of superposition [24] states that the magnetic flux density of multiple sources is the sum over all single sources:

$$\vec{B} = \sum_{i=1}^{n} \vec{B}_i.$$

The magnetic flux density for a single dipole (eq. 4.1), the location vector $\vec{H}_i$, position vector $\vec{r}$ and orientation vector $\vec{m}_i$ are (fig. 4.1):

$$\vec{H}_i = \begin{pmatrix} H\cos\gamma_i \\ H\sin\gamma_i \\ 0 \end{pmatrix}, \vec{r} = \begin{pmatrix} x \\ y \\ z \end{pmatrix}, \vec{m}_i = \begin{pmatrix} m\sin\nu_i\cos\mu_i \\ m\sin\nu_i\sin\mu_i \\ m\cos\nu_i \end{pmatrix}. \tag{5.2}$$

case	κ_1	κ_2	κ_3	decision variables	k	number of dipoles
3	1	1	1	γ_{i-1}, μ_i, ν_i	$3n-1$	$n = 1, 2, 3$
2	0	1	1	μ_i, ν_i	$2n$	$n = 1, 2, 3$
1	0	1	0	μ_i	n	$n = 1, 2, ..., 6, 8, 16$

Table 5.1: Summary of the different κ_j values and the respective decision variables. The three κ_j represent optimization cases with varying degree of complexity for the analytic dipole formulation. γ_i is the angles of the positioning vector of each dipole and μ_i and ν_i are the polar and azimuthal angles of the magnetization vectors.

H is the distance from the dipoles to the origin, γ_i is the positioning angle of the ith dipole and starts from the x-axis counterclockwise, $\vec{r}$ is the position vector of the magnetic field, $\vec{m}_i$ is the magnetic moment of the dipoles with the orientation angles μ_i and ν_i.

The derivation of the magnetic flux density $\vec{B}$ for the asymptotic approximation (appendix A) is inserted into the expression for the Lorentz force of the asymptotic approximation (eq. 4.7). This resulting objective function depends on the predefined parameter $\xi = (H, m, R, \mu_0, v, \sigma)$ and the optimization variables $x = (\gamma, \mu, \nu)$ (fig. 4.1).

The complexity of the optimization problem varies with the number of decision variables $k = \kappa_1 \sum_{i=2}^{n} \gamma_i + \kappa_2 \sum_{i=1}^{n} \mu_i + \kappa_3 \sum_{i=1}^{n} \nu_i$. $\kappa_j = 0, 1$ is a binary number and represents different optimization cases of complexity, which are summarized in tb. 5.1. The position of the first dipole is always fixed without loss of generality because of symmetry. γ_1 is always given, reducing the problem by one variable. Three different optimization cases are investigated.

In case 3 the optimization variables are the azimuthal and polar angles of the orientation vectors of the magnetic dipole moments and their position vector. The feasible set of the position vectors is not arbitrary but fixed to a ring in the $z = 0$ plane, i.e. $\gamma_2, ..., \gamma_n$, because this allows for a derivation of an analytic objective function (appendix A).

In case 2 the angles γ_i of the position vectors $\vec{H}_i$ are distributed equidistantly around the pipe. The orientation of the magnetic moments is allowed to adjust in 3D leaving its azimuthal and polar angles as the decision variables.

Case 1 is the simplest formulation and considers only the variation of the azimuthal angle of the orientation of the magnetic dipole moment, i.e. the dipole moment vectors are only allowed to change in the $z = 0$ plane. However, as will be seen later, even this simple variation of the problem is still very complicated with increasing numbers of dipoles.

This successive decrease in the number of optimization variables is done to study the influence of the type of variable on the problem and also to test the capability of the optimization algorithm to handle the problem.

The geometry of the investigated problems allows the reduction of the optimization variables. For example, if the cylinder is surrounded by only one dipole, there is an infinite number of optimal solutions, since at any arbitrary position, within

the stated limits, the magnetic dipole moment may point perpendicular towards or away from the cylinder surface to yield a maximal Lorentz force. Therefore, for the first dipole, we can fix the position without loss of generality and limit the magnetic moment orientation to a half sphere. Keeping this in mind, we obtain only one global maxima which represents all possible global maxima, which can be derived by rotating the dipoles around the z-axis and by changing the magnetic moments orientation by 180°.

Chapter 6

Results

In this work, three different optimization types are used. The goal is to find the optimal setup of magnetic field sources in the framework of Lorentz force velocimetry.

The first is a completely analytic solution. This is done with the analytic formulation of the Lorentz force for a small number of dipoles (chapter 6.1). However, with increasing numbers of dipoles the numerical capabilities of symbolic computation software like MATHEMATICA [68] are quickly exceeded. The derivation of first derivatives and hessian matrix is still possible, but the system of equations containing the critical points is no longer analytically solvable.

Second is the numerical optimization of the analytic formulation of the Lorentz force for a higher number of dipoles (chapter 6.2). For a small number of dipoles the standard optimization algorithms of the MATLAB optimization toolbox [38] successfully find global maxima. For larger numbers of dipoles it is not possible to ascertain the type of the derived extrema and it is highly possible that only local maxima were reached.

And last is the numerical and black box optimization applied to complex 3D FEM model setups (chapter 6.3).

6.1 Completely Analytic Solution

The analysis starts with the most complex optimization formulation case 3. For $n = 1$ dipole the Lorentz force does not depend on the position of the dipole as long as $H = const.$ because of the cylindrical character of the pipe. γ_1 is set to 90° so that the dipole is located at $(x, y, z) = (0, H, 0)$. The orientation of the dipole (μ_1 - polar angle and ν_1 - azimuthal angle) is optimized (fig. 4.1). Replacing the constant parameters with $w = m^2\mu_0^2R^4\sigma v_z/H^7$ results in the following objective function (eq. 4.7):

$$\begin{aligned} F(\xi, \vec{x}) &= \frac{45\mu_0^2R^4\sigma v_z}{131072H^7}\left(16m_{x1}^2 + 149m_{y1}^2 + 95m_{z1}^2\right) \\ &= \frac{45w}{131072}\left(\sin^2(\nu_1)\left(149\sin^2(\mu_1) + 16\cos^2(\mu_1)\right) + 95\cos^2(\nu_1)\right). \end{aligned}$$

There are two first derivatives, one for the variables μ_1 and ν_1:

$$\frac{\partial F(\xi,\vec{x})}{\partial \mu_1} = \frac{5985w}{65536}\sin(\mu_1)\cos(\mu_1)\sin^2(\nu_1)$$
$$\frac{\partial F(\xi,\vec{x})}{\partial \nu_1} = -\frac{45w}{262144}(133\cos(2\mu_1)+25)\sin(2\nu_1).$$

These derivatives are set to zero and the system of equations is solved analytically. The resulting critical points are potential extrema:

$$(\mu_1,\nu_1)^{crit} = (\mu_1,0°),(0°,-90°),(0°,90°),(-90°,-90°),(-90°,90°),\\ (90°,-90°),(90°,90°),$$

where μ_1 can take on any value.

The Hessian matrix is needed to assert the character of a critical point:

$$\mathcal{H}_F(\xi,\vec{x}) = \frac{\partial^2 F(\xi,\vec{x})}{\partial\mu_1\partial\nu_1} \\ = \frac{w}{131072}\begin{pmatrix} 11970\cos(2\mu_1)\sin^2(\nu_1) & 23940\cos(\mu_1)\cos(\nu_1)\sin(\mu_1)\sin(\nu_1) \\ 5985\sin(2\mu_1)\sin(2\nu_1) & -45(133\cos(2\mu_1)+25)\cos(2\nu_1)\end{pmatrix}.$$

Maxima are the critical points for which the Eigenvalues of the Hessian are negative:

$$(\mu_1,\nu_1)^b = (-90°,-90°),(-90°,90°),(90°,-90°),(90°,90°).$$

Thus, the dipole orientations that create a maximal Lorentz force point either perpendicular away or towards the cylinder surface (fig. 6.4a).

Since this problem has only two variables a graphical analysis (fig. 6.1) is possible and the obtained optimized variables match the four global maxima in the plot.

For $n = 2$, the position of the dipoles and their orientation is variable (case 3). The location of one dipole can be fixed because of the symmetry of the problem to for example at $(0, H, 0)$. This eliminates one variable.

The objective function is:

$$\begin{aligned} F_{case3}(\xi,\vec{x}) = \frac{45\mu_0^2R^4\sigma v_z}{262144H^7}(&-7\cos(2\gamma_2)\left(16m_{x1}m_{x2}-19m_{x2}^2+44m_{y1}m_{y2}+19m_{y2}^2\right)\\ &+28\cos(\gamma_2)(\sin(\gamma_2)(-8m_{x1}m_{y2}+22m_{x2}m_{y1}+19m_{x2}m_{y2})\\ &+5m_{x2}m_{y1})\\ &+140\sin(\gamma_2)(m_{y1}m_{y2}+2m_{z1}m_{z2})+32m_{x1}^2-48m_{x1}m_{x2}\\ &+165m_{x2}^2+298m_{y1}^2+148m_{y1}m_{y2}\\ &+5\left(33m_{y2}^2+38m_{z1}^2+20m_{z1}m_{z2}+38m_{z2}^2\right)). \end{aligned}$$

When their position is allowed to vary, the dipoles collect themselves in a single point $\gamma_i = \gamma_1 = 90°$. The corresponding optimal dipole orientations point perpendicular towards or away from the cylinder surface $\mu_i = \pm 90°$ and $\nu_i = \pm 90°$.

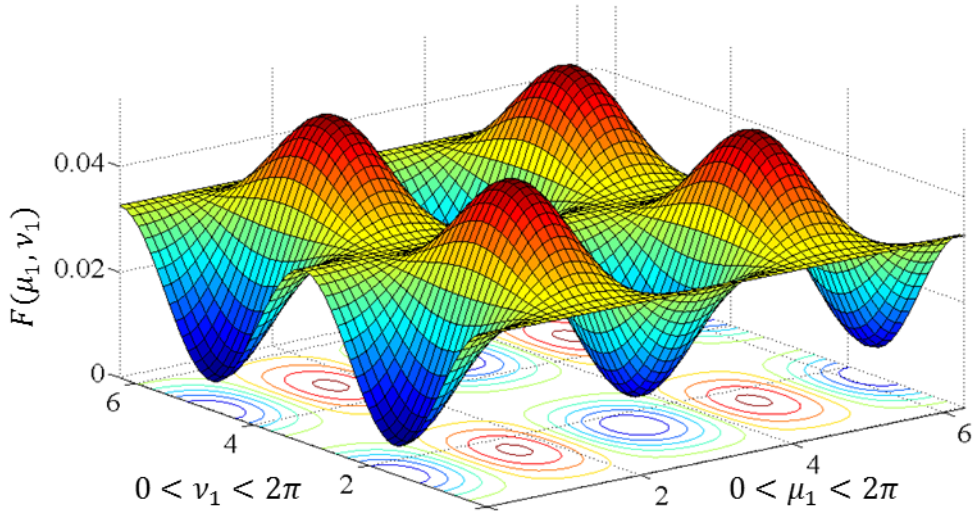

Figure 6.1: Lorentz force for one dipole depending on the azimuthal (μ_1) and polar (ν_1) angles of the orientation vector of the magnetic moment.

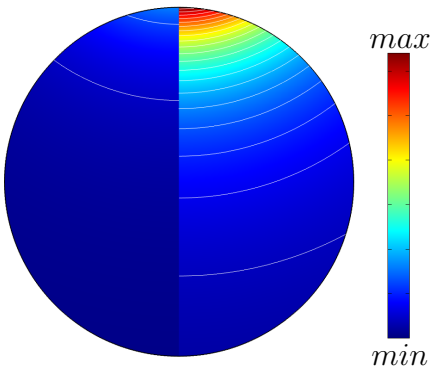

Figure 6.2: Magnitude of the magnetic field inside the cross section of the cylinder directly underneath the dipole. The cylinder is divided vertically in the middle. The left hand shows the optimized magnetic field for $n = 1$ dipole and the right hand side the optimized magnetic field for $n = 4$ dipoles.

Meaning that a single strong filed source is better than several weaker ones. Fig. 6.2 shows the cross-section of the cylinder directly underneath the dipole. The cylinder is divided vertically and the left hand side shows the resulting magnetic field for the optimized dipole orientation of $n = 1$ dipole. On the right hand side, we have the resulting magnetic field created by $n = 2$ dipoles. This is attributed to the fast decay of the magnetic field, which varies with H^{-3} and H^{-7} for close and large distances respectively [43], [8]. When the magnetic field strength of multiple weak dipoles reaches the pipe, it is weaker than the field created by one strong magnetic source. Regarding the practical aspect for the magnet system construction, the strength of permanent magnets cannot be increased randomly, but it is limited by current magnet materials. As such, the dipoles are placed equidistantly around the cylinder and only their orientation is optimized.

In case 2, the dipoles will be equidistantly positioned around the pipe. For $n = 2$, the dipoles face each other, leaving μ_i and ν_i as the decision variables (case 2).

The objective function is:

$$F_{case2}(\xi, \vec{x}) = \frac{45\mu_0^2 R^4 \sigma v_z}{131072 H^7}(16(m_{x1} + m_{x2})^2 + 149m_{y1}^2 + 158m_{y1}m_{y2} + 149m_{y2}^2 + 95m_{z1}^2 - 90m_{z1}m_{z2} + 95m_{z2}^2).$$

The optimal polar angles are $\mu_i = \pm 90°$ and, as long as the dipoles are positioned in one plane only, the optimal azimuthal angles are also $\nu_i = \pm 90°$. Thus, the azimuthal angles can be removed from the list of optimization variables, while $\mu_i = [0°, 360°]$, which leads to case 1.

In case 1, the azimuthal angles $\nu_i = 90°$, so that the orientation of the dipoles varies only in the perpendicular $z = 0$ plane.

The objective function for case 1 is:[1]:

$$F_{case1}(\xi, \vec{x}) = \frac{45w}{131072}(158\sin(\mu_1)\sin(\mu_2) + 32\cos(\mu_1)\cos(\mu_2) + 149[\sin^2(\mu_1) + \sin^2(\mu_2)] + 16[\cos^2(\mu_1) + \cos^2(\mu_2)]).$$

The two first derivatives of the objective function F_{case1} are:

$$\frac{\partial F_{case1}(\xi, \vec{x})}{\partial \mu_1} = \frac{45w}{65536}(16\sin(\mu_1)\cos(\mu_2) - \cos(\mu_1)(133\sin(\mu_1) + 79\sin(\mu_2)))$$
$$\frac{\partial F_{case1}(\xi, \vec{x})}{\partial \mu_2} = \frac{45w}{65536}(16\cos(\mu_1)\sin(\mu_2) - \cos(\mu_2)(79\sin(\mu_1) + 133\sin(\mu_2))).$$

The critical points which solve the system of equations consisting of $\frac{\partial F_{case1}(\xi, \vec{x})}{\partial \mu_1} = 0$ and $\frac{\partial F_{case1}(\xi, \vec{x})}{\partial \mu_2} = 0$ are:

$$(\mu_1, \mu_2)^{crit} = (0°, 0°), (0°, 180°), (-90°, -90°), (-90°, 90°), (90°, -90°), (90°, 90°), (180°, 0°), (180°, 180°).$$

[1]The functions for cases 3 and 2 are shown with their dependency on the components of the magnetic moments. The expansions to include the angles μ_i and ν_i is rather long and can be done by inserting eq. 5.2.

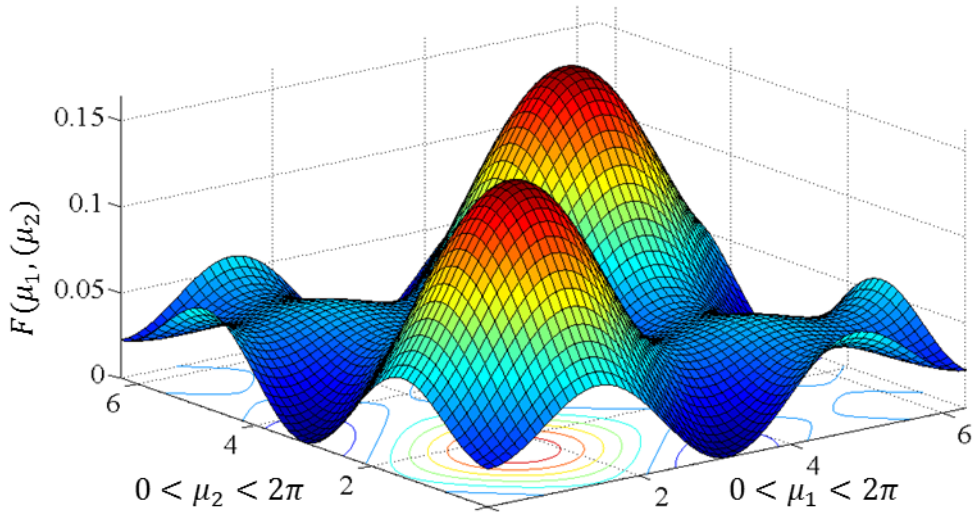

Figure 6.3: Lorentz force for two dipole depending on the azimuthal angles μ_1 and μ_2 of the orientation vector of the magnetic moments.

The hessian for this problem is:

$$\mathcal{H}_{F_{case1}}(\xi,\vec{x}) = \frac{\partial^2 F_{case1}(\xi,\vec{x})}{\partial\mu_1\partial\mu_2}$$
$$= -\frac{45w}{131072}\begin{pmatrix} 2(-79\sin(\mu_1)\sin(\mu_2) & 2(16\sin(\mu_1)\sin(\mu_2) \\ -16\cos(\mu_1)\cos(\mu_2)+133\cos(2\mu_1)) & +79\cos(\mu_1)\cos(\mu_2)) \\ 2(16\sin(\mu_1)\sin(\mu_2) & (-95\cos(\mu_1-\mu_2) \\ +79\cos(\mu_1)\cos(\mu_2)) & +63\cos(\mu_1+\mu_2)+266\cos(2\mu_2)) \end{pmatrix}.$$

And the eigenvalues are negative ($\frac{\partial^2 F_{case1}(\xi,\vec{x})}{\partial\mu_1\partial\mu_2} = 0$) for the following critical points:

$$(\mu_1,\mu_2)^{max} = (-90°,-90°),(-90°,90°),(90°,-90°),(90°,90°).$$

These critical points are all maxima. Whether the type of maxima is local or global, can be determined by graphical analysis (fig. 6.3), since there are only two variables, or by inserting the points into the objective function and comparing the calculated values. The global maxima are:

$$(\mu_1,\mu_2)^b = (-90°,-90°),(90°,90°),$$

meaning that they are aligned with respect to each other and perpendicular to the cylinder surface.

With increasing number of variables the symbolic software MATHEMATICA is not able to solve the system of equations to attain the critical points. For these problems numerical optimization is used next.

	algorithm	gradient	constraints
$fminunc$	trust-region	yes	no
$fminsearch$	Nelder-Mead simplex direct search	no	no
$fmincon$	trust-region-reflective	yes	yes

Table 6.1: Summary of suitable MATLAB optimization algorithms.

6.2 Numerical Analytic Solution

The means to solve the analytic dipole problem is quickly exceeded with rising numbers of dipoles. To continue the optimization process numerical algorithms from the MATLAB optimization toolbox [38] are used. Since the problem is non-linear and uses box constraints the algorithm $fmincon$ should be suited best. Nevertheless $fminunc$ and $fminsearch$ are also tested to revise the best choose for this problem. This chapter compares and evaluates the results of the optimization of the analytic dipole problem with numerical means.

$fminunc$, $fminsearch$ and $fmincon$ are all algorithms that optimize scalar, non-linear, multivariable functions and are in this aspect well suited for the analytic dipole problem. Tb. 6.1 summarizes the characteristics of the three possible problems of the MATLAB Optimization Toolbox [38]. $fmincon$ seems to be the most appropriate since it uses gradients and considers the constraints for the feasible set.

The parameter $exitflag$ categorizes the reason why the algorithm terminates and thus indicates how successful the optimization has been. A value of 1 means that the first-order optimality measure (chapter 5.2.2) and maximum constraint violation were less than the specified limit. $exitflag$ takes on 0, when the number of allowed function evaluation is exceeded, i.e. the algorithm was not able to satisfy the convergence criteria during $200 \cdot k$ function evaluations. Interior-point algorithms ($fmincon$) denote a 2 when the first-order optimality measures are not meet, but the change in the variable x and maximum constraint violation were less than the specified limits.

The suitability of the three optimization problems $fmincon$, $fminsearch$ and $fminunc$ are evaluated for the analytic dipole problem. Theoretically all three are applicable to the provided non-linear objective function, while $fminunc$ does not utilize the box constraints of the feasible set and $fminsearch$ does not consider additional derivative information and is the least sophisticated with its Nelder-Mead simplex direct search algorithm (chapter 5.2.2).

For the comparison of the optimization problems the objective functions of the analytic dipole formulation (eq. 4.7) for $n = 1, 2, 3, 4, 5, 6, 8$ and 16 dipoles were used. The algorithms were run 1000 times starting from randomly determined starting points x^0. These starting points are the same depending on the number of optimization variables, i.e. the same 1000 randomly determined individual starting points were used for the nth dipole problem for all three optimization formulations ($fmincon$, $fminsearch$ and $fminunc$). The optimized Lorentz force $\mathcal{F}$ is nondimensionalized by dividing it with the prefactor $-w$, i.e. the value of $\mathcal{F}$ depends

only on the decision variables, the respective angles. The optimized values for the variables and objective function are summarized in tb. 6.3 and fig. 6.4 shows the cross section view of the cylinder and dipoles. The success rates of the algorithms $fminunc$, $fmincon$ and $fminsearch$ are summarized in tb. 6.2. Figs. 6.6-6.13 show the success of the three optimization algorithms for the first 100 starting points. Each of the 100 runs represents one of optimization rounds with the resulting optimized nondimensionalized Lorentz force.

The same three optimization cases are considered like in section 6.1. Case 3 has the most decision variables for for $i = 1, 2, ..., n$ dipoles, i.e. the azimuthal angles ν_i and the polar angles μ_i of the magnetic moments of the dipoles and the position of the dipoles specified by γ_{i+1} since the position of the first dipole γ_1 is fixed without loss of generality.

Case 2 sets $\gamma_i = 90° + (i-1)360°/n$, leaving μ_i and ν_i as decision variables.

Case 1, considers only a variation of the polar angles μ_i, while the azimuthal angles are set to $\nu_i = 90°$.

The total number of dipoles optimized in case 3 was increased successively from $n = 1$ to $n = 3$.

The $n = 1$ dipole formulation includes two optimization variables, the azimuthal ν_1 and μ_1 polar angles of the orientation vector of the magnetic dipole moment. Because of the symmetry of the problem, the location of the dipole can be arbitrarily fixed without loss of generality. Since there are only two variables the objective function can be plotted, graphically analyzed (fig. 6.1) and the global maxima determined. There are multiple global maxima. The Lorentz force is maximal when the dipole points perpendicularly to or away from the pipe, which is at $\mu_1 = \pm 90°$ and $\nu_1 = \pm 90°$ (fig. 6.4a) producing a Lorentz force $\mathcal{F} = 0.0511$. The optimized values of the force for the first 100 starting points (fig 6.6) show that $fminunc$ is a lot less successful in reaching the global maximum compared with the other two algorithms. It lands very often on an inflection point and it also has $exitflag$ values of 2 meaning that the algorithm did not converge in the allowed number of iterations. Therefore, $fminunc$ is not further considered for analysis. $fmincon$ and $fminsearch$ always have an $exitflag$ value of 1, i.e. the first-order optimality measure and maximum constraint violation were satisfied. Both problems found the global maximum almost all the time, making it not yet possible to assert the success of one algorithm over the other.

For $n = 2$ dipoles in case 3 when the location of the dipoles is also optimized, the dipoles coalesce into one point, which is the fixed position of the first dipole. The effect is that the two dipoles act as if they are one single dipole with a four[2] times higher strength $\mathcal{F} = 0.2046$. As with the formulation with only one dipole, the orientation of the vector of the magnetic moments of the two dipoles point in the same direction, perpendicularly away or towards the pipe $\mu_i = \pm 90°$ and $\nu_i = \pm 90°$. Fig. 6.7 indicates that $fminsearch$ reaches more frequently the global

[2]Because of the quadratic dependence in m, see eq. 6.1.

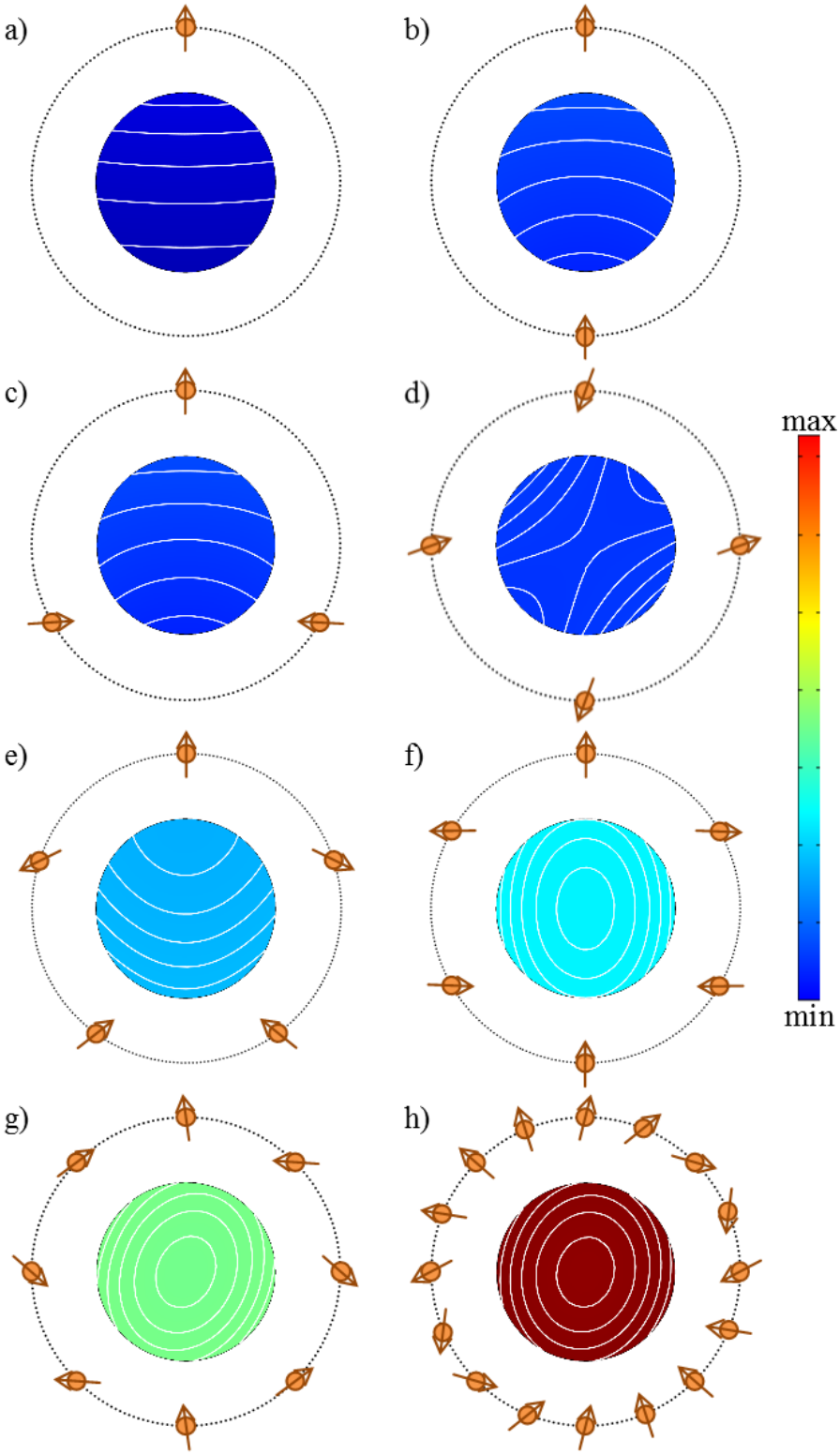

Figure 6.4: Depiction of the azimuthal angles μ_i and the resulting magnetic field (color and contour plots) in the xy cross section of the cylinder for the numerically optimized analytic problems.

algorithm			local max	successful convergence
$fminunc$	$n = 1$		82%	99%
$fmincon$	$n = 1$		96%	100%
		case 3	40%	95%
	$n = 2$	case 2	69%	98%
		case 1	60%	87%
		case 3	11%	0%
	$n = 3$	case 2	53%	0%
		case 1	43%	100%
	$n = 4$		34%	95%
	$n = 5$		71%	100%
	$n = 6$		52%	67%
	$n = 8$		55%	21%
	$n = 16$		27%	0%
$fminsearch$	$n = 1$		94%	100%
		case 3	55%	100%
	$n = 2$	case 2	94%	100%
		case 1	84%	100%
		case 3	39%	83%
	$n = 3$	case 2	100%	99%
		case 1	55%	100%
	$n = 4$		93%	100%
	$n = 5$		92%	100%
	$n = 6$		93%	100%
	$n = 8$		98%	86%
	$n = 16$		39%	1%

Table 6.2: Success rates of the algorithms $fminunc$, $fmincon$ and $fminsearch$.

maximum than $fmincon$ and even when $fminsearch$ lands on a local maximum, it finds a higher objective function value than $fmincon$ (case 3). The $exitflag$ value for $fminsearch$ is always 1, meaning that the first-order optimality measure and maximum constraint violation were less than the specified limit.

The qualitative findings gained from the convergence study when two dipoles are considered are confirmed in the results for $n = 3$ dipoles. In case 3 all dipoles cluster together, resulting in one stronger magnetic dipole moment pointing directly away or towards the pipe and a higher force $\mathcal{F} = 0.4604$.

The current results are enough for a qualitative assessment of all similar setups for increasing number of dipoles. When the location of the dipoles is also optimized, the dipoles coalesce into one point, which is the fixed position of the first dipole. This supports the importance of the strength of the magnetic source (fig. 6.2, section 6.1). A source, for example a magnet, that is twice as strong is far superior to two sources that are only half as strong each (fig. 6.5). This is attributed to the quadratic

dipoles $n \rightarrow$ $i \downarrow$	1 μ_i in °	2 μ_i in °	3 μ_i in °	4 μ_i in °	5 μ_i in °	6 μ_i in °	8 μ_i in °	16 μ_i in °
1	90.0	90.0	90.0	199.6	90.0	89.9	98.5	94.1
2		90.0	3.2	70.3	206.0	181.8	175.9	126.0
3			176.8	199.6	38.5	358.1	319.1	163.3
4				70.3	141.4	90.0	36.5	218.6
5					333.9	181.8	98.5	299.0
6						358.1	175.9	354.2
7							319.1	31.5
8							36.5	63.4
9								94.1
10								126.0
11								163.3
12								218.6
13								299.0
14								354.2
15								31.5
16								63.4
force $\mathcal{F}$	0.0511	0.1566	0.1915	0.4757	0.5058	0.7395	6.1523	5.1440

Table 6.3: Overview of the optimized polar angles μ_i and nondimensionalized force $\mathcal{F}$ of the analytic dipole problem for case 1.

dependence of m and the fast decay of the magnetic field, which varies with distance H. The decrease of the field of a dipole is $\sim H^{-3}$ for small distances and $\sim H^{-7}$ for large distances [59], [26], [8]. Thus, the strength of the magnetic field of the two weak dipoles is a lot weaker when it finally reaches the pipe than the magnetic field created by a single, twice as strong, magnetic source. However, regarding the practical aspect for the construction of the magnetic source, i.e. the magnet system, the strength of permanent magnets cannot be increased randomly, but is limited by current magnet materials. While it is possible to optimize the size and mass of the permanent magnets, it is not effective to arbitrarily increase them since the force measurement setup limits the dimensions and mass of the magnet system (chapter 6.5).

For the further analysis of the analytic dipole problem the positioning variables will be removed as an optimization parameter and the dipoles are equidistantly fixed $\gamma_i = 90° + (i-1)360°/n$, which is case 2.

The results for case 2 for $n = 1$ dipole are the same as in case 3, i.e. the Lorentz force is maximal when the dipole points perpendicularly to or away from the pipe, which is at $\mu_1 = \pm 90°$ and $\nu_1 = \pm 90°$ (fig. 6.4a) producing a Lorentz force $\mathcal{F} = 0.0511$.

The maximum for $n = 2$ dipoles is reached when the variables are $\mu_1 = \mu_2 = \pm 90°$ and $\nu_i = \pm 90°$, meaning the orientation vectors are parallel to each other and

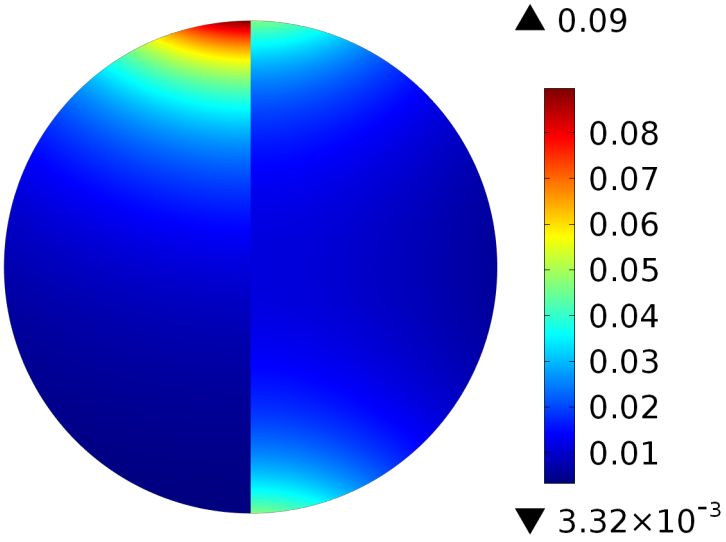

Figure 6.5: Magnitude of the magnetic field inside the cross section of the cylinder directly underneath the dipole. The cylinder is divided vertically in the middle. It shows the optimized magnetic field for $n = 2$ dipoles for case 3 (left hand side) and case 2/case 1 (right hand side). The magnetic field reaching the cylinder is stronger when the dipoles cluster together in one position, than when the dipoles on opposite sides of the cylinder.

perpendicular to the pipe (fig. 6.4b). Which essentially also happens in the first case, but now the dipoles are placed at opposite positions and not in the same spot.

For $n = 3$ dipoles, the optimal values for the azimuthal angles are $\nu_i = 90°$ and the optimal polar angles have values of $(\mu_1, \mu_2, \mu_3) = (90°, 3.2°, 176.8°)$ (fig. 6.4c), which produce a force $\mathcal{F} = 0.1915$.

These results indicate that a maximal Lorentz force can only be reached, when the dipoles orient themselves in a plane perpendicular to the cylinder axis. As such, the azimuthal angles of the vector of the magnetic dipole moment will be set to $\nu_i = 90°$, i.e. restricting the orientation vector of the magnetic dipole moments to the $z = 0$ plane. This also reduces the complexity of the optimization problem, which increases exponentially with the number of variables. The consideration of variable azimuthal angles is again of interest when neighboring dipole rings interact with each other (chapter 6.4).

In case 1 the dipoles are equidistantly placed around the pipe and the azimuthal angles are $\nu_i = 90°$, only the polar angles μ_i are optimized.

The results for $n = 1$ dipole are the same as above.

For $n = 2$ dipoles the optimized variables are $\mu_i = \pm 90°$ (fig. 6.4b) with a force of $\mathcal{F} = 0.1566$. This is the same result which was gained from case 2. Since there are only two optimization variables a 3D presentation (fig. 6.3) of the objective function is possible which proves the location of the two global maxima. *fmincon* exceed in the first case in 1% of the runs the specified number of objective function

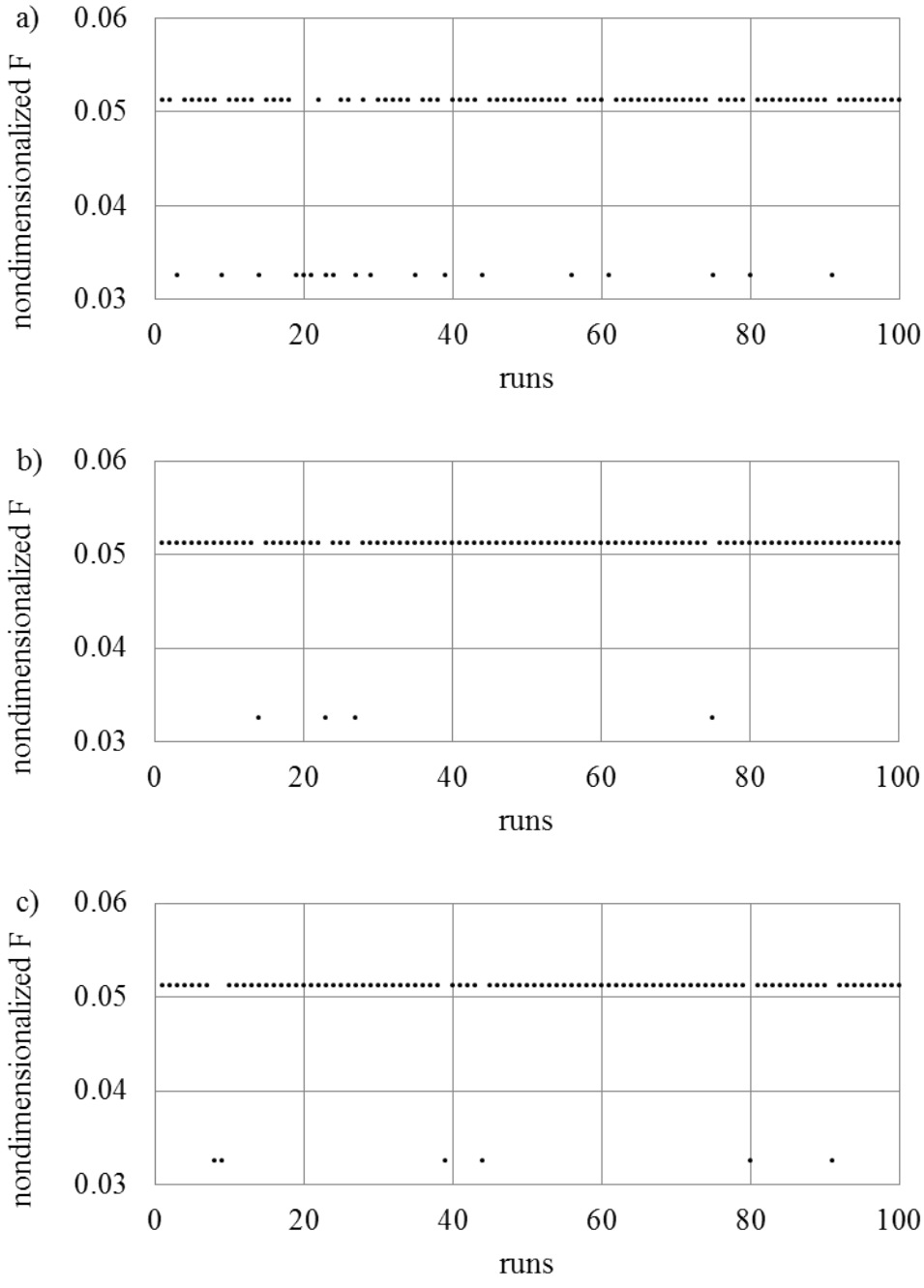

Figure 6.6: Best values of the nondimensionalized force $\mathcal{F}$ for the first 100 starting points for $n = 1$ dipole, optimized by: a) $fminunc$, b) $fmincon$, c) $fminsearch$.

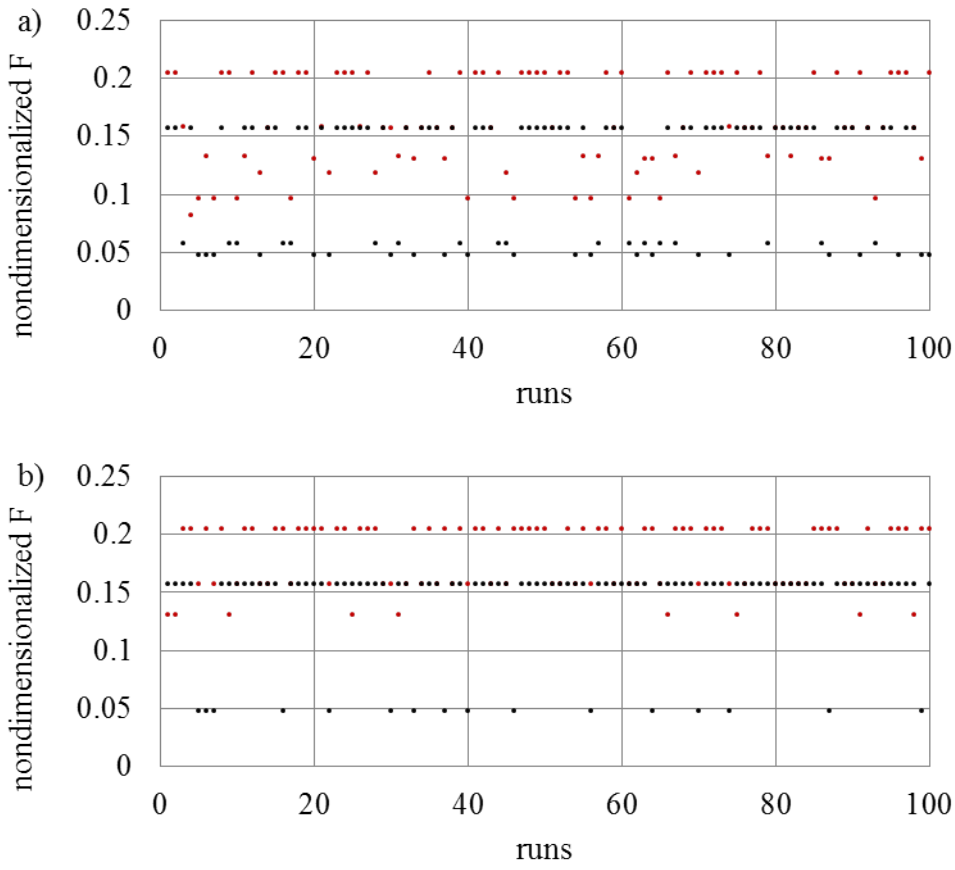

Figure 6.7: Best values of the nondimensionalized force $\mathcal{F}$ for the first 100 starting points for $n = 2$ dipole, optimized by: a) $fmincon$, b) $fminsearch$, for case 3 (red) and case 1 (black).

evaluations, indicated by $exitflag = 0$. In 3% of the runs of the first case $exitflag = 2$ meaning that the first-order optimality measure was not met but the variables and maximum constraint violation were less than specified. Thus, even though $fmincon$ is a more sophisticated algorithm, $fminsearch$ seems to be better suited for the dipole problem.

For $n = 3$ dipoles, case 1 has three parameters and a graphical analysis is not possible anymore. However, three variables are still quite a small number and it is feasible to do a brute force calculation with a parameter step size of 1° to find maxima. In a brute force calculation all possible values of the feasible set are assessed within the limits set by this step size. The resulting maximum is at $(\mu_1, \mu_2, \mu_3) = (90°, 5°, 175°)$. The angles μ_2 and μ_3 differ by 1.8° from the maximum reached by the numerical optimization. There are two possible reasons for this deviation. The first is numerical error. The second is that the algorithm converged to a local maximum. $fminsearch$ found this maxima more often than $fmincon$ (fig. 6.8).

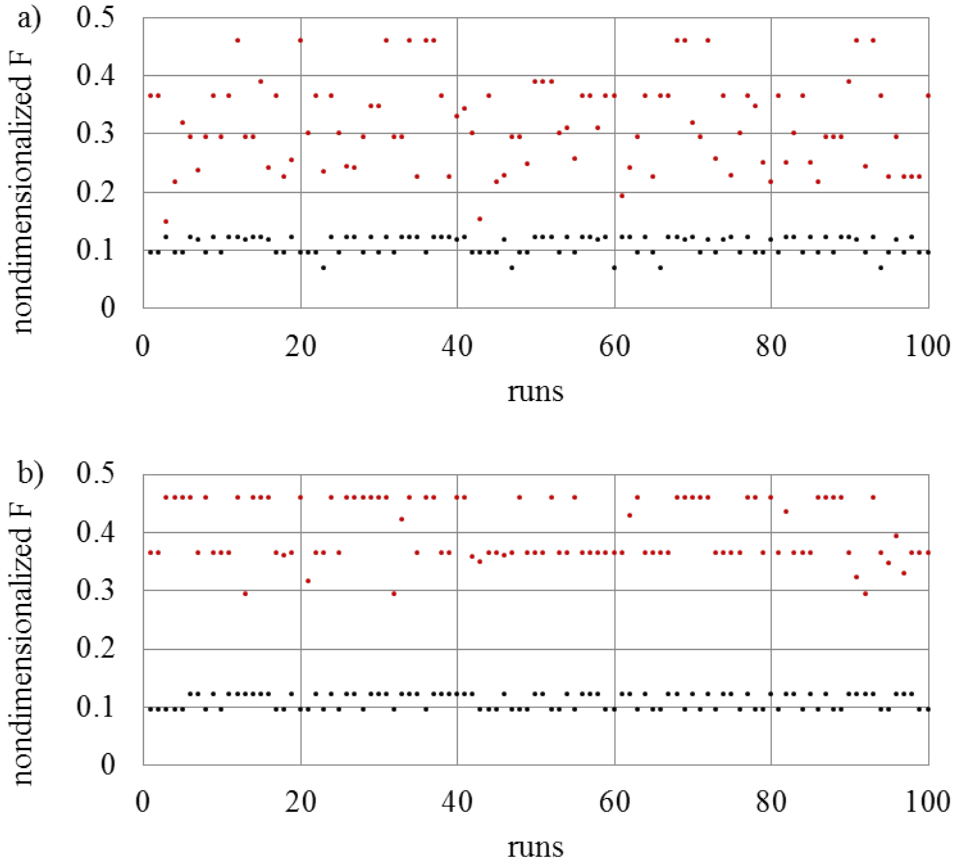

Figure 6.8: Best values of the nondimensionalized force $\mathcal{F}$ for the first 100 starting points for $n = 3$ dipole, optimized by: a) $fmincon$, b) $fminsearch$, for case 3 (red) and case 1 (black).

The convergence plots for four dipoles are very interesting (fig. 6.9). The values of the objective function found by $fminsearch$ are always in the range of $\mathcal{F} = 0.4757$ with an angle configuration of $(\mu_1, \mu_2, \mu_3, \mu_4) = (199.6°, 70.3°, 199.6°, 70.3°)$ (fig. 6.4d). There is no proof, that this maximum is global or only local, a graphical analysis is not possible and a brute force calculation with a sufficiently fine parameter step size is not feasible. This is the only instance that an algorithm always converges to such a narrow range of the objective function. This suggests, but does not guarantee, that a global maximum was reached. $fmincon$ finds also sometimes objective function values that are in the same range of the maxmima reached by $fminsearch$, but it often lands in a weaker local maximum. The values of $exitflag$ also support the success of $fminsearch$, which always satisfy the first-order optimality measure and maximum constraint violation, while $fmincon$ sometimes just meets the specified change in variables and maximum constraint violation.

For $n = 5, 6$ and 8 dipoles the convergence plots (fig. 6.10-6.12) exhibit a similar behavior and are examined together. $fminsearch$ is the more successful algorithm. It finds the highest maximum objective function value more often. Only in less

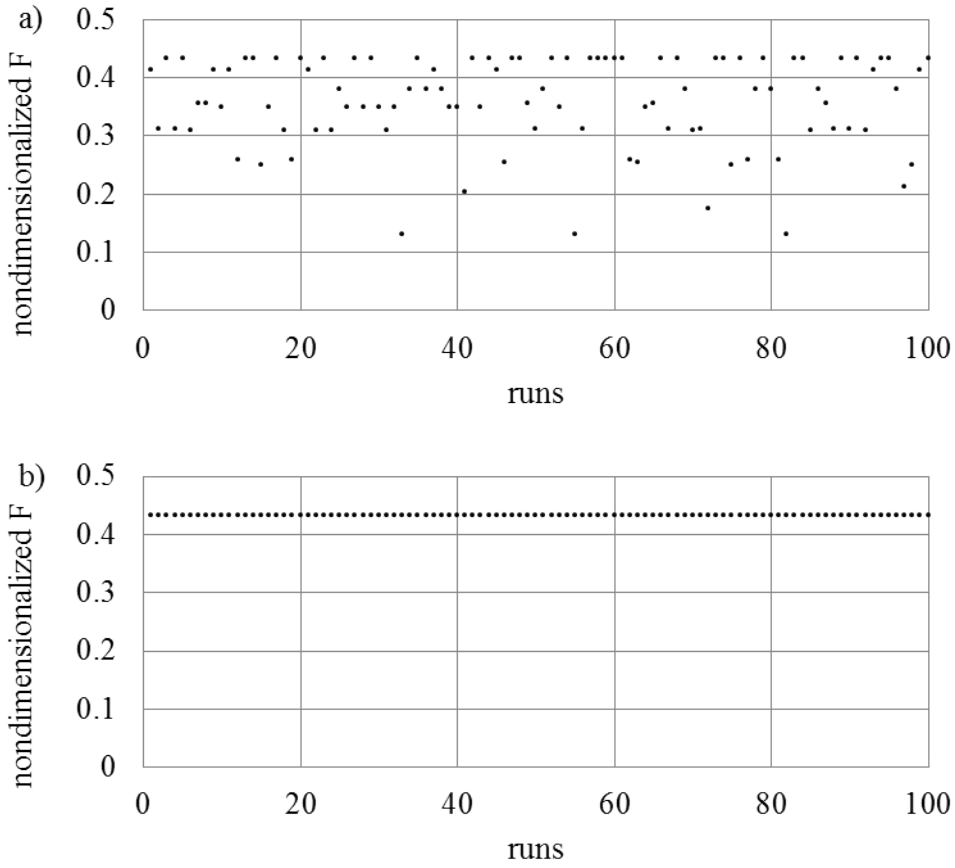

Figure 6.9: Best values of the nondimensionalized force $\mathcal{F}$ for the first 100 starting points for $n = 4$ dipole, optimized by: a) $fmincon$, b) $fminsearch$.

than 10% of the runs this maximum was not found. It cannot be proven what kind of maximum the attained results are, but the consisted results reinforce the likelihood that it is a global maximum. $fmincon$ is also able to find the same maximal value of the objective function but with a much lower probability, which further decreases with increasing dipoles. $exitflag$ again supports the qualitative assessment of the two algorithms. $fminsearch$ satisfies the first-order optimality measure and maximum constraint violation for $n = 5$ and 6 dipoles, for 8 dipoles it sometimes exceeds the allowed number of maximal function evaluation. Allowing for more function evaluations might result in $exitflag$ to always take on the value 1. $exitflag$ indicates that $fmincon$ does not reach the first-order optimality measure, but $fmincon$ still satisfies the limits for the change in the variables and maximum constraint violation. The frequency for $exitflag = 2$ increases with the number of dipoles. The optimal polar angles μ_i and the corresponding forces are summarized in tb. 6.3 and visualized in fig. 6.4e-g.

The case of $n = 16$ dipoles is the last formulation of the analytic dipole problem in this context. It is the most complex with 16 variables and with the most complicated expression of the objective function. This makes it very difficult for an optimization

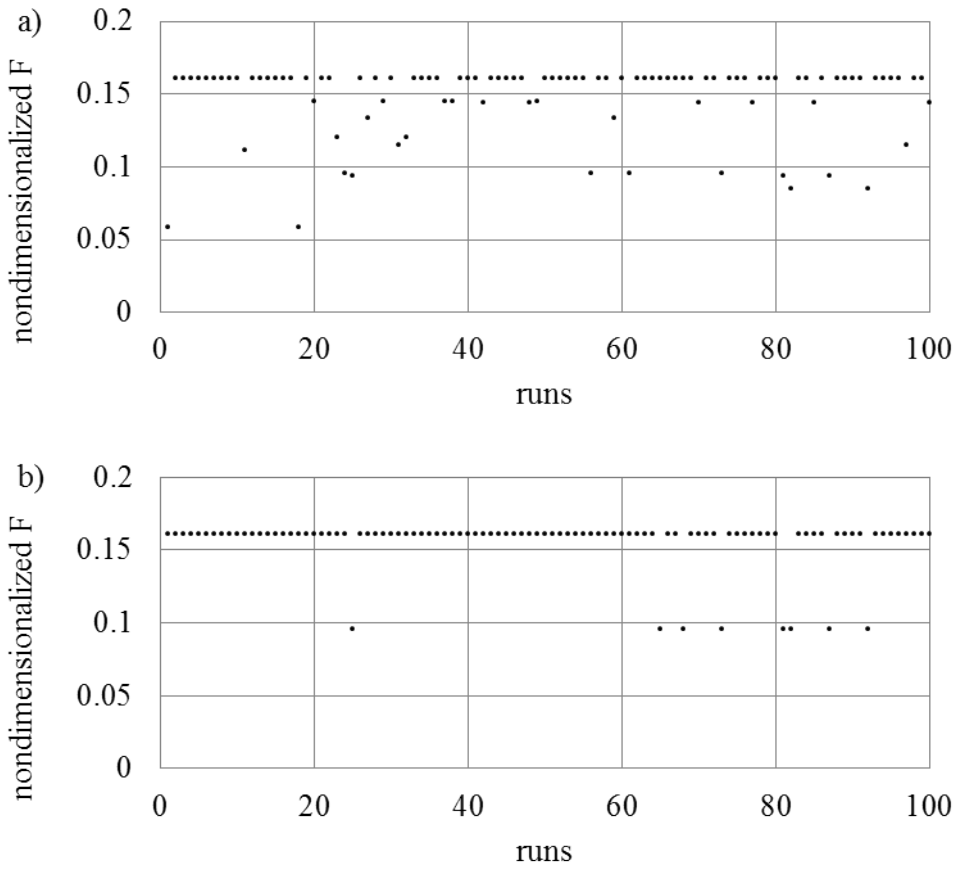

Figure 6.10: Best values of the nondimensionalized force $\mathcal{F}$ for the first 100 starting points for $n = 5$ dipole, optimized by: a) $fmincon$, b) $fminsearch$.

algorithm to find the global maximum. The attained maximal value of the objective function $\mathcal{F} = 5.1440$.

Both algorithms $fminsearch$ and $fmincon$ reach this value (fig. 6.13). However, it is not possible to determine which of the algorithms is more successful. Both are not able to satisfactorily process the problem and land often in local maxima. This is also reflected in the values for $exitflag$. $fmincon$ stopped because the change in the variables and maximum constraint violation was less than specified. $fminsearch$ reached the limit of allowed function evaluations, except for a single instance where it was able to meet the first-order optimality measure and maximum constraint violation. The optimal polar angles μ_i and the corresponding force are listed in tb. 6.3 and visualized in fig. 6.4h.

Fig. 6.14 shows a graphical depiction of the vector fields created by the optimized magnetic dipole moments for $n = 16$ dipoles indicated by the orange dots. One quarter of the cylinder was cut out. The color indicates the magnitude and the arrows point into the direction of a) the magnetic field, b) eddy currents and c) Lorentz force. The magnetic field is almost homogeneous. The eddy currents form two closed loops which are separated by the dipole plane. The Lorentz force points

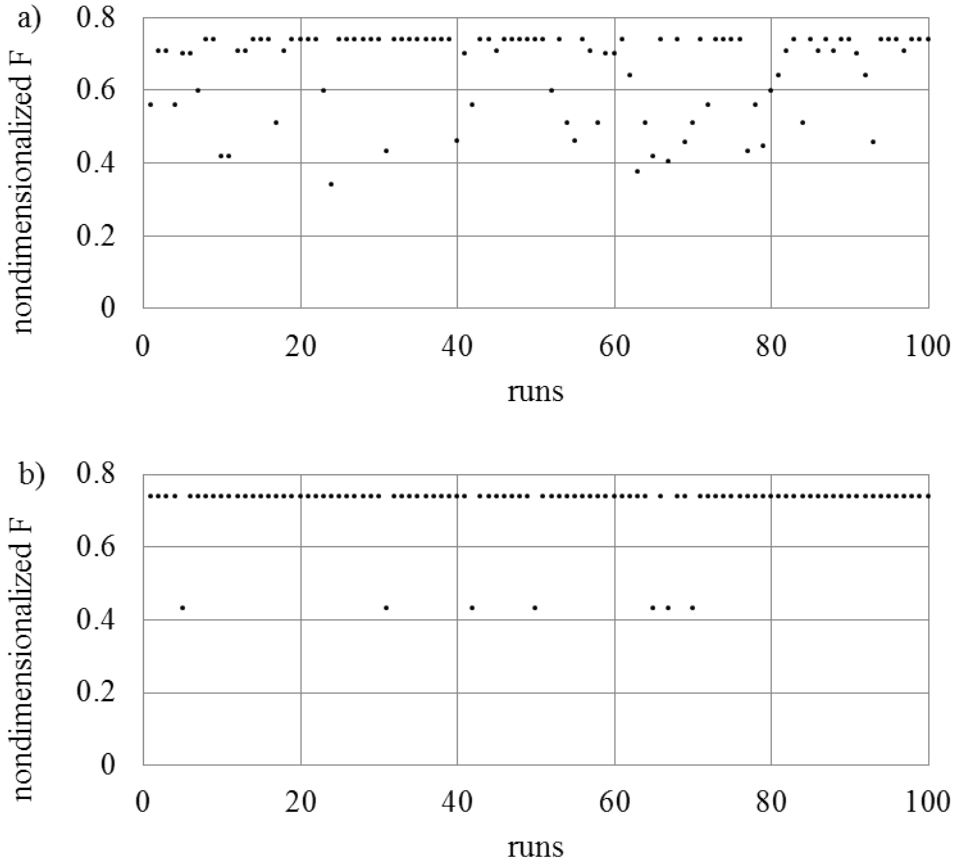

Figure 6.11: Best values of the nondimensionalized force $\mathcal{F}$ for the first 100 starting points for $n = 6$ dipole, optimized by: a) $fmincon$, b) $fminsearch$.

towards the cylinder axis on the one side of the dipole plane, while it points outwards on the other side. This results from the interaction of the magnetic field and eddy currents. The Lorentz force points only in the center of the cylinder against the velocity direction and opposes the movement, which is the component of the Lorentz force used in LFV.

The results of case 1 can be summarized very nicely by splitting the azimuthal angles μ_i into the position angles γ_i and the deflection angles ω_i with respect to the line connecting the origin and respective dipole, i.e. $\omega_i = \mu_i - \gamma_i$, i.e. $\omega_i = \mu_i - \gamma_i$. Fig. 6.15 shows the azimuthal angles μ_i with γ_i on the abscissa and ω_i on the ordinate. There is a periodicity $\omega_{i+n/2} = \omega_i + 180°$. Also ω_i meanders along the line $\gamma_i = \omega_i$. The angles ω_i are confined to a rather limited area close to this line, seemingly restricting the variable domain to $\omega_i \in [\omega_i + \delta, \omega_i - \delta]$ with $\delta < 70°$. With increasing numbers of dipoles the curve seems to approach an optimum that represents the optimal orientation of infinitely many dipoles, i.e. a continuous ring. . The polar angles μ_i are split into the position angles γ_i and the deflection ω_i with respect to the line connecting the origin and respective dipole, i.e. $\omega_i = \mu_i - \gamma_i$.

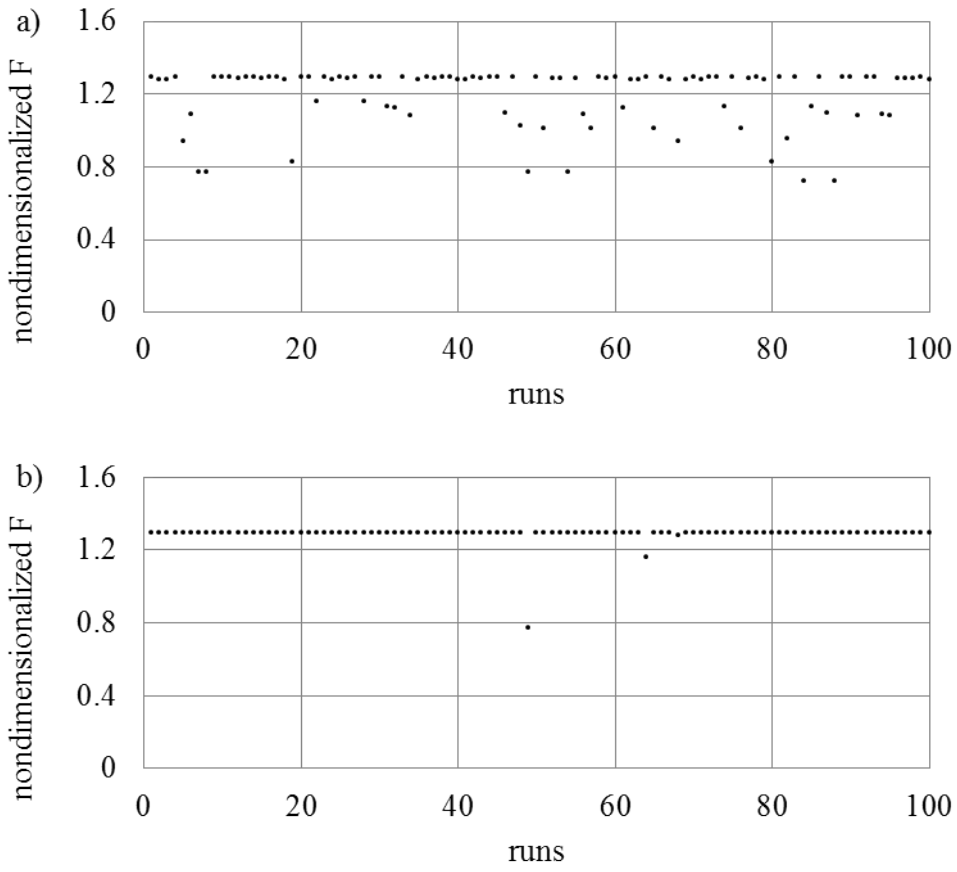

Figure 6.12: Best values of the nondimensionalized force $\mathcal{F}$ for the first 100 starting points for $n = 8$ dipole, optimized by: a) $fmincon$, b) $fminsearch$.

Global Optimization

The algorithms used in chapter 6.2 do not guarantee to find the global maximum and very often they land in local maxima as can be seen from the results (fig. 6.6-6.13). Next to the normal optimization toolbox, which was used until now, MATLAB offers a global optimization toolbox [38]. The included algorithms have specific functions designed to deal with global maxima and minima. Two of these solvers, the global search and the multistart solver, were tested. Both are gradient based methods, use local solver and multiple starting points to find local and global maxima. Thus, qualitatively they analyze a problem in the same way, like the local optimization problems in chapter 6.2, i.e. a local solver was started from multiple starting points. The difference lies in the type of acquisition of the starting points. In chapter 6.2, 1000 randomly chosen points were used as starting configurations, while the global optimization algorithms determine them via other, internal methods like scatter-search algorithms or evenly distributed between barriers.

For small numbers of variables the results gained by these global solvers coincide with the local solvers. This is true specifically for $n = 1, 2$ dipoles when all possible

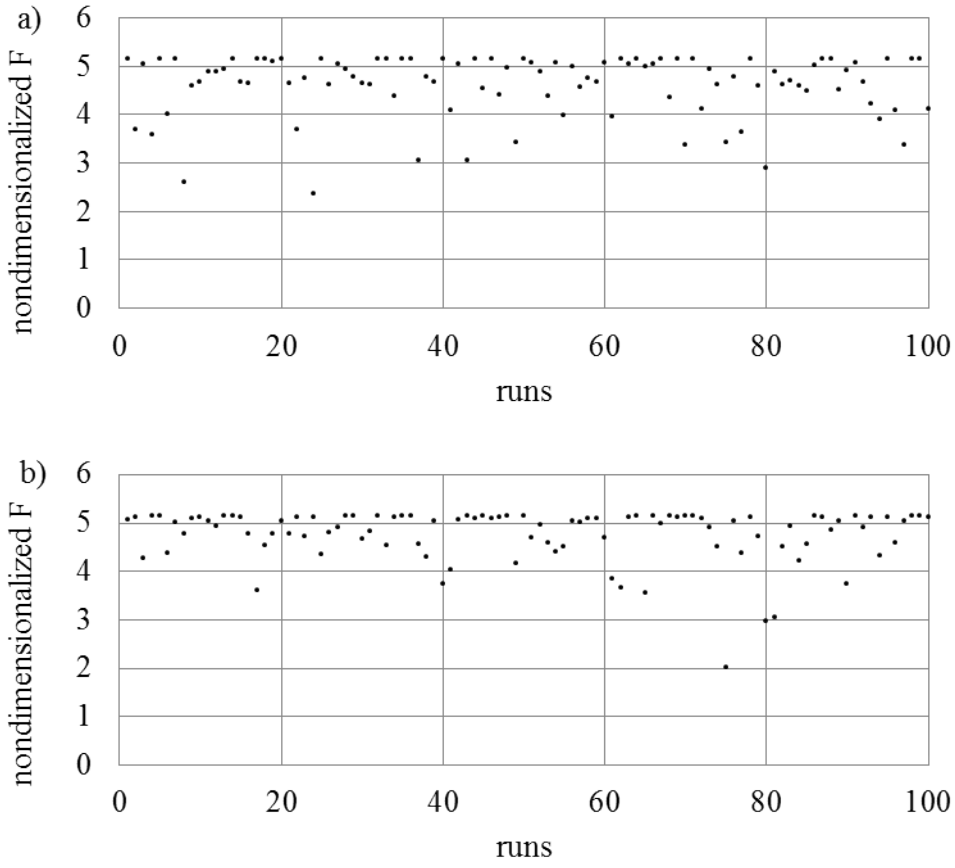

Figure 6.13: Best values of the nondimensionalized force $\mathcal{F}$ for the first 100 starting points for $n = 16$ dipole, optimized by: a) $fmincon$, b) $fminsearch$.

variables (γ, ν, μ) are included and for $n = 4$ when only μ are considered. In all other cases the procedure applied in the last chapter proved to be more successful in finding local optima.

Also a modified αBB method [13] which finds all optimal solutions was used for a small number of variables, i.e. $n = 2, 4$ and varying only μ_i. They proofed that the obtained maxima from chapter 6.2 where indeed global maxima. Nevertheless, these algorithms reached their limits when the number of variables was increased.

In summary: the optimization solver $fminsearch$ with its Nelder-Mead simplex direct search algorithm proved to be more successful than the more sophisticated $fmincon$, which uses interior-point algorithm and also considers gradients in its calculations. The global optimization solvers were only effective for problems with a small number of variables and verified the results gained by the local solvers. With higher number of variables the global solvers failed miserably. Therefore the algorithms provided by the normal MATLAB optimization toolbox are used in this work, i.e. $fminsearch$ and $fmincon$.

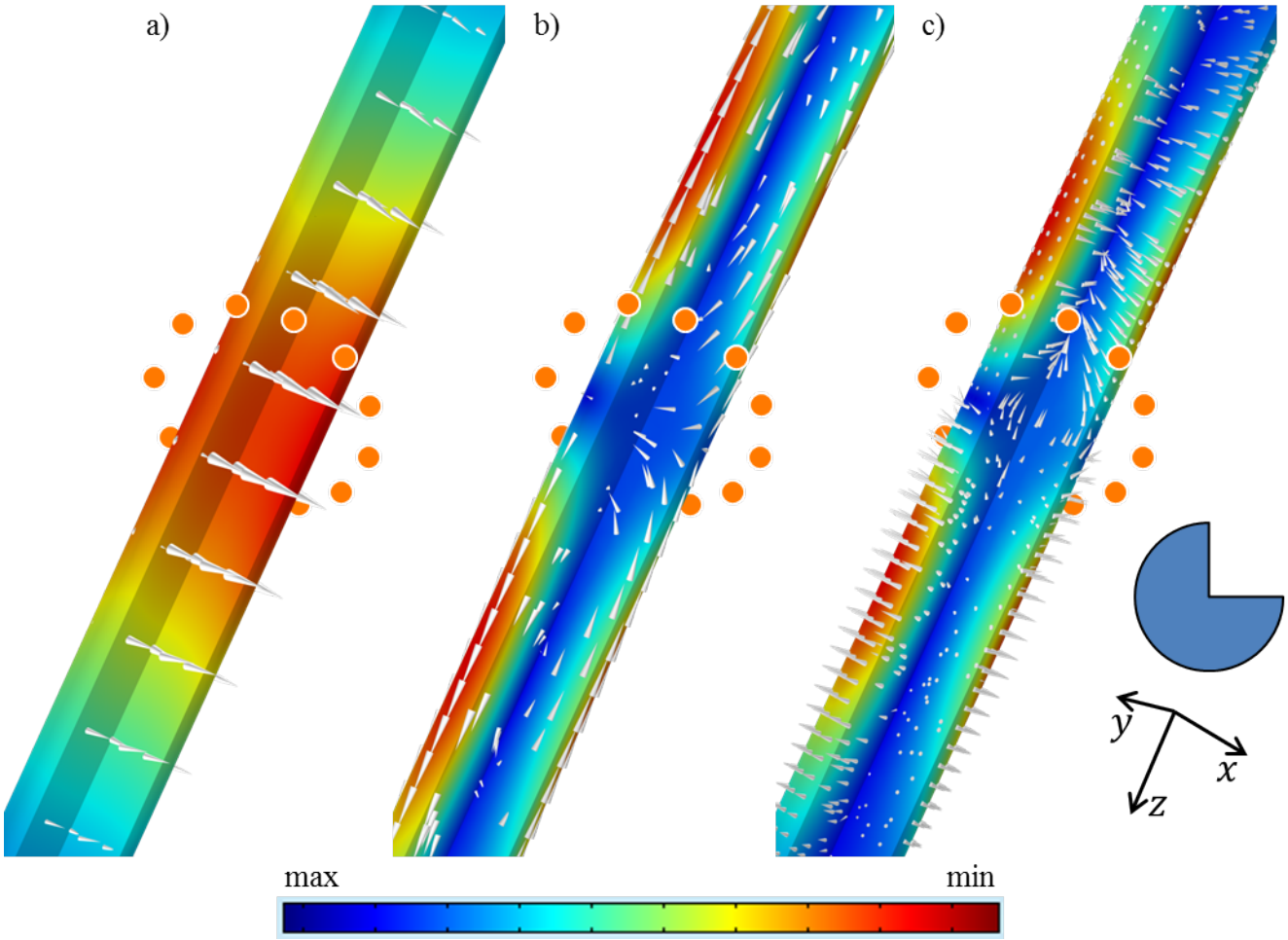

Figure 6.14: Graphical depiction of the vector fields created by the optimized magnetic dipole moments for $n = 16$ dipoles indicated by the orange dots. One quarter of the cylinder was cut out. The color indicates the magnitude and the arrows point into the direction of a) the magnetic field, b) eddy currents and c) Lorentz force.

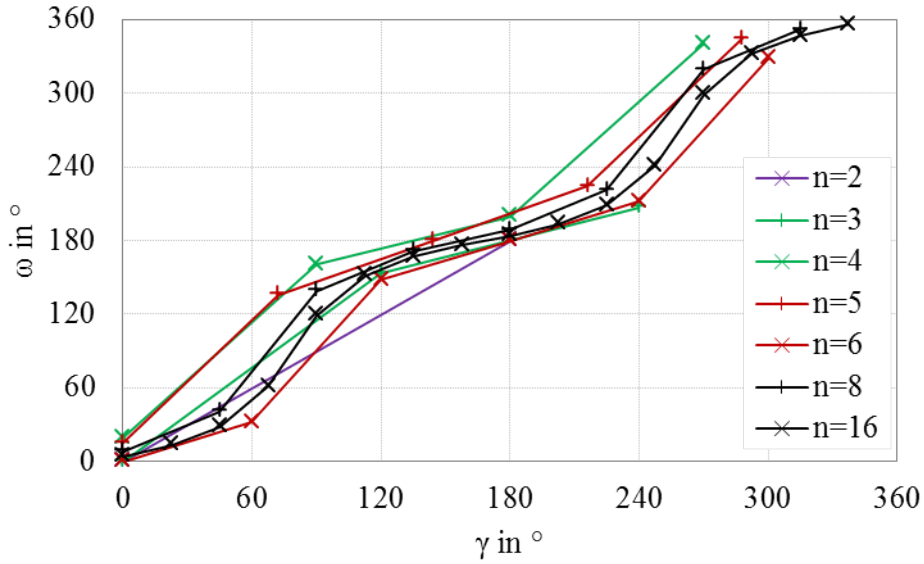

Figure 6.15: Azimuthal angles μ_i for the numerical optimization of the analytic problems for $n = 1, 2, ..., 16$ dipoles. μ_i is separated into position angle γ_i and deflection angle $\omega_i = \mu_i - \gamma_i$.

6.3 Numerical FEM Solution

The analytic analysis of the dipole problem has its limits. First the applied approximation is only true for magnetic dipoles placed very far away from the pipe. At least in a distance of $h/R = 10$ where R is the radius of the pipe and h is the distance from the dipole to the cylinder surface (fig. 4.1). Unfortunately, this is a very inconvenient setup for practical applications. The farther away the magnetic field sources the smaller the Lorentz force. It is proportional to H^{-3} for small [59], [43] and H^{-7} for large distances [26], [8]. A complete analytic study of the dipole problem is not possible, especially with multiple arbitrarily placed dipoles. Furthermore, complex realistic magnet systems and the resulting forces can only be analyzed by numerical means. Such being the case, the problems studied with the complete analytic formulation are reconstructed with two FEM software programs and also optimized to gauge which software is better suited for more complex problems.

Here two software programs are used. One is the in-house code PROMETHEUS [35] and the second is the commercial program COMSOL Multiphysics [10]. Both software programs are introduced, their functional principle is explained and their advantages and disadvantages considered in chapter 3. They both solve the governing equations (chapter 2). The magnetic field of the dipoles is analytically specified inside the pipe by eq. 4.1. The outer air domain can be discarded, reducing the simulation region to the pipe. This significantly decreases the number of FEM elements and computational cost.

For the study of the multi dipole problem the distance of $h = 25cm$, a cylinder length of $L = 5h = 125cm$ and radius $R = 2.5cm$ is used (fig. 4.1). These geo-

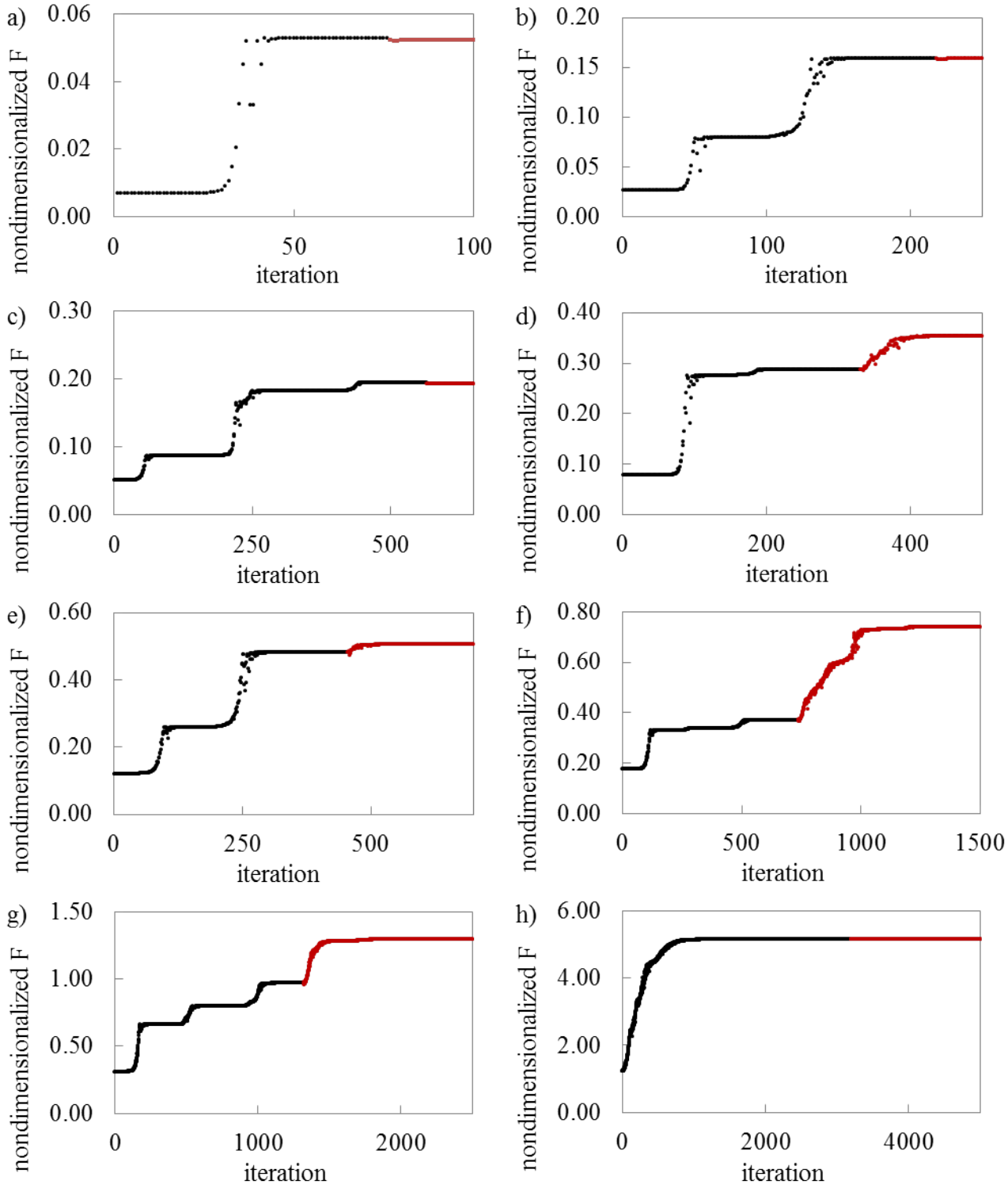

Figure 6.16: Convergence of the objective function in PROMETHEUS optimized by *fminsearch* for a coarse (black) and fine (red) mesh for a) $n = 1$, b) $n = 2$, c) $n = 3$, d) $n = 4$, e) $n = 5$, f) $n = 6$, g) $n = 8$, h) $n = 16$.

dipoles $n \rightarrow$ $i \downarrow$	1 μ_i in °	2 μ_i in °	3 μ_i in °	4 μ_i in °	5 μ_i in °	6 μ_i in °	8 μ_i in °	16 μ_i in °
1	89.9	89.9	89.9	109.3	96.4	89.9	98.3	92.8
2		89.9	4.6	160.5	250.2	181.6	175.7	124.3
3			175.4	109.3	46.9	358.0	318.7	160.5
4				160.5	151.9	89.9	36.4	211.7
5					351.0	181.6	98.3	290.9
6						358.0	175.7	350.8
7							318.7	29.6
8							36.4	62.0
9								92.8
10								124.4
11								160.5
12								211.7
13								290.9
14								350.8
15								29.6
16								62.0
force $\mathcal{F}$	0.0522	0.1575	0.1929	0.3523	0.5011	0.7393	1.2940	5.1474

Table 6.4: Overview of the optimized polar angles μ_i and nondimensionalized force $\mathcal{F}$ of the numerical FEM dipole problems simulated with PROMETHEUS and optimized by the inbuilt gradient method.

metric parameters where chosen, because at a ratio of $h/R = 10$ the asymptotic approximation just begins to hold, while the appropriate parameters for the cylinder allows for a relatively fine and regular mesh, i.e. the mesh elements are not stretched too much out of proportion along the pipe. Two meshes with different degrees of fineness are used in the optimization procedure. A coarse mesh decreases computational time so that the optimization algorithm may converge quickly. The resulting optimal angle configurations are then used as the starting point for the calculations with a finer mesh. For PROMETHEUS the parameters for the coarse mesh are $\zeta_f = 2mm$, $\zeta_c = 8mm$ and for the fine mesh are $\zeta_f = 1mm$ $\zeta_c = 4mm$, i.e. the same as in chapter 4.2. The model in COMSOL (chapter 4.2, fig. 3.4) is meshed with the default setting of $finer$. For the fine calculation the setting for the sensitive region is changed to $extremelyfine$ with a maximum / minimum element size of $1mm$ / $0.01mm$.

PROMETHEUS is optimized with two methods. The first is the inbuilt gradient-ascent method (chapter 5.2.3), which requires absolutely no licenses and uses parallel computing. The second is the MATLAB problem $fminsearch$ [38], $fmincon$ is passed on because it was less successful with the analytic problem (chapter 6.2). COMSOL is used in conjunction with $fminsearch$ but also with the algorithm NOMAD (chapter 5.2.4), which was made for the optimization of time and resource expensive black box problems.

dipoles $n \rightarrow$ $i \downarrow$	1 μ_i in °	2 μ_i in °	3 μ_i in °	4 μ_i in °	5 μ_i in °	6 μ_i in °	8 μ_i in °	16 μ_i in °
1	90.0	89.9	89.9	70.5	89.9	90.0	98.3	94.1
2		90.0	3.9	19.4	205.8	181.7	36.4	125.9
3			176.0	70.5	38.4	358.2	318.7	163.4
4				19.4	141.5	90.0	175.7	218.6
5					334.1	181.7	98.3	298.8
6						358.2	36.4	354.0
7							318.7	31.4
8							175.7	63.3
9								94.1
10								126.0
11								163.4
12								218.6
13								298.8
14								354.0
15								31.4
16								63.3
force $\mathcal{F}$	0.0526	0.1578	0.1927	0.3526	0.5064	0.7399	1.2951	5.1476

Table 6.5: Overview of the optimized polar angles μ_i and nondimensionalized force $\mathcal{F}$ of the numerical FEM dipole problems simulated with PROMETHEUS and optimized by $fminsearch$ from the MATLAB optimization toolbox [38].

Now the objective function is not given as an analytic expression, but its value is provided by an FEM calculation. One function evaluation by FEM software is relatively time consuming. Based on the results of chapter 6.2 the dipoles are equidistantly placed around the cylinder in a ring of radius $H = h + R$ (fig. 4.1). The decision variables are reduced to μ_i, since all dipoles are in the $z = 0$ plane. It is not feasible anymore to explore multiple starting configurations, let alone 1000, as it was done with the analytic study of the problem (chapter 6.2). All problems for $n = 1, 2, ..., 6, 8, 16$ dipoles start from the same point $\mu_i = 0°$.

Tb. 6.3 and 6.5 provide an overview of the results from PROMETHEUS with the fine mesh optimized with the gradient ascent method and $fminsearch$ respectively.

The differences between the optimized angles for the coarse (not shown) and fine mesh are up to $\pm 3°$ for the gradient ascent method. The algorithm also stops after only a few function evaluations with the fine mesh. The same cannot be said for the optimization with $fminsearch$. The angles for the coarse (not shown) and fine mesh may vary by $\pm 155°$ and a high number of function evaluations are also needed for the optimization with the fine mesh, even though the starting point was the optimal configuration gained from the coarsely meshed problem. The optimization is prone to finding local optima and depends also on the cylinder mesh sizes. The algorithm starts from the starting point and converges to an optimum for a coarsely meshed cylinder. The optimization with the fine mesh, starting from this optimum, can leave

dipoles	analytic	PROMETHEUS		COMSOL	
n	obj. function	gradient	*fminsearch*	*fminsearch*	NOMAD
1	0.0511	0.0522	0.0527	0.0517	0.0517
2	0.1566	0.1575	0.1579	0.1566	0.1566
3	0.1915	0.1929	0.1928	0.1924	0.1923
4	0.4757	0.3523	0.3526	0.3524	0.3357
5	0.5058	0.5012	0.5064	0.5029	0.5061
6	0.7395	0.7393	0.7400	0.4146	0.6989
8	6.1523	1.2940	1.2952	1.1766	1.2945
16	5.1440	5.1475	5.1477	2.8292	5.0814

Table 6.6: Overview of the best objective function values (nondimensionalized force $\mathcal{F}$) from the numerical optimization.

this local optimum to converge at another point. Fig. 6.16 shows the convergence plots for the coarse mesh and how it continues when a fine mesh is considered. There is no significant change of the objective function values for the different meshes for $n = 1, 2, 3, 16$. This is not the case for $n = 4, 5, 6, 8$, where the algorithm leaves the local optimum for the coarsely meshed cylinder to find a better configuration.

Despite this different behavior for the angles, the final objective function values agree relatively well with each other (tb. 6.6) considering that the analytic objective functions from section 6.2 uses the asymptotic approximation, while the dipoles in the FEM models are exactly modeled, but closer to the cylinder surface. The difference between the gradient ascent and *fminsearch* methods are $\leq 1\%$ and compared to the analytic results (tb. 6.3) the difference is $\leq 0.7\%$, except for $n = 4$ where it is 8.7%.

The model in COMSOL is optimized with *fminsearch* (chapter 5.2.2) and NOMAD (chapter 5.2.4). The calculated optimized angles are not shown, because it would not lead to new fruitful findings. The objective function values derived by *fminsearch* and NOMAD do not agree as well as PROMETHEUS with the analytic results (tb. 6.6, fig. 6.17). This is especially the case for $n > 6$ dipoles, with NOMAD being more successful than *fminsearch*. For $n = 4$ dipoles both the PROMETHEUS and COMSOL models differ rather strongly from the analytic result, but agree well with each other. This is not surprising since the FEM models were started with the same angle configuration and seem to have found the same maximum. Numerical uncertainties can account for the slight differences between them.

The results reflect the behavior of the respective objective function. The landscapes of the objective functions have multiple valleys, hills and inflection points, which makes optimization very difficult, but some agreement is still obtained.

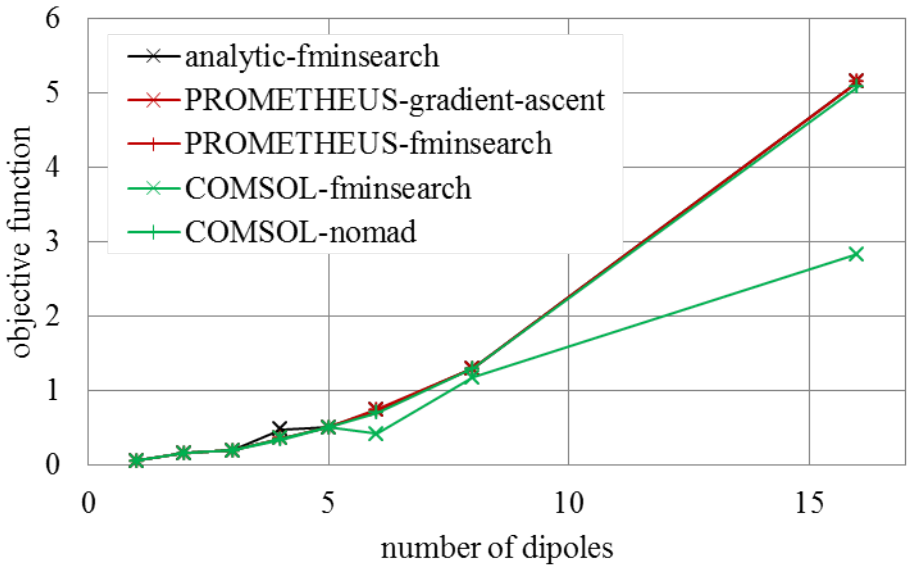

Figure 6.17: Best objective function values (nondimensionalized force $\mathcal{F}$) from the numerical optimization.

6.4 PROMETHEUS - Multi-Dipole-Ring Problems

Up until now the dipole problem was restricted to a relatively small number of dipoles placed in a plane at a specific distance around the cylinder. The goal was to gain insight into possible realistic magnet systems. With these limitations the only obtainable practical arrangement can be of cylindrical nature with a cavity, like a Halbach cylinder which can produce a high magnetic field on the inside of the structure, while it is weaker on the outside [21].

The results of the last section suggest that a magnetic field which is rather close to a Halbach cylinder is suited best for LFV. A Halbach cylinder setup produces an almost homogeneous magnetic field within the cylinder, while it cancels itself on the outside. Here, the magnetic field is not quite as uniform, but more closely to the magnetic field a dipole in the center of the setup would produce.

To assess possible and more complex magnet systems the number of dipoles needs to be increased also along the cylinder axis. The study of the dipole problem restricted to one plane suggest that a ring of $n = 8$ dipoles to be a good compromise between number of variables and qualitative representation of the results.

Three different setups are analyzed in this context. In the first case two successive rings of 8 dipoles are placed around the cylinder, while the second case includes three successive dipole rings (fig. 6.18). The last case is the most complex setup investigated in the scope of the dipole problem. It consists of 11 successive dipole rings. s denotes the distance between each ring, which is an optimization variable only in the first two cases, since it would be too time consuming for the third case.

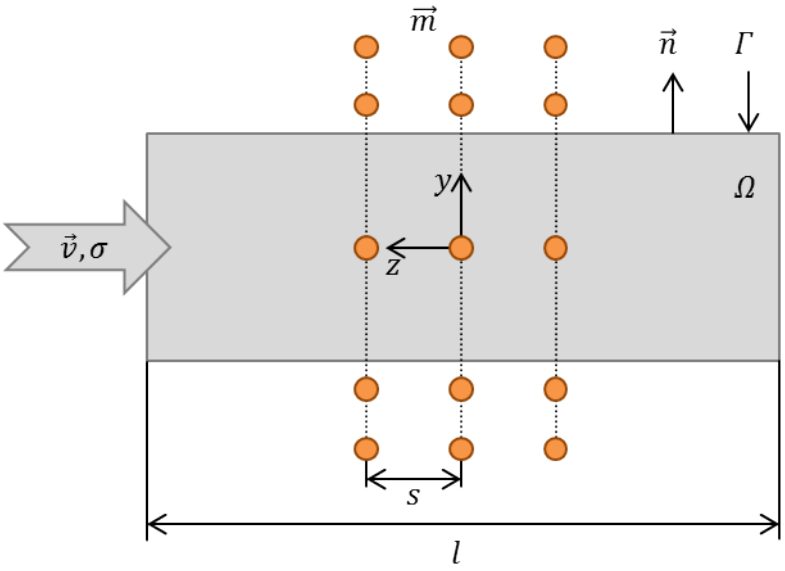

Figure 6.18: Geometric parameters of the multi dipole ring setups for 2 and 3 dipole rings.

The orientations of the magnetization vectors of the dipoles are optimized which are given by azimuthal ν_{ij} and polar angles μ_{ij}, where $i = 1, 2, ..., 8$ is the number of dipoles in one ring and $j = 1, 2, ..., o$ is the number of successive dipole rings.

The parameters for the geometric setup of these problems are based on different attributes than in former chapters. There, the main goal was the comparison with the analytic asymptotic solution. With this aspect in mind the length of the cylinder and the distance between cylinder and dipoles were chosen. Now, the dipole distribution should represent realistic, possible magnet configurations. They are placed closer to the cylinder surface at $h = 2.5cm$ (fig. 6.18). This allows for the approximation of a magnet with a dipole and leaves necessary space between magnets and pipe surface, since they are not permitted to touch. The length of the cylinder depends on the lateral expansion $S = (o - 1)s$ of the dipole system. A systematic variation of the length shows $l = 5S$ to be an adequate value for the simulations. The conductivity is $\sigma = 4S/m$, the velocity is $v = 5m/s$ and the dipole moment is $m = 2Am^2$.

PROMETHEUS and the inbuilt gradient-ascent method (chapter 5.2.3) are used for the optimization. The mesh has again two different degrees of refinement. The first optimization is done with a rather coarse grid defined by the parameters $\zeta_f = 2mm$, $\zeta_c = 8mm$ to quickly find an optimal solution, which is then the starting point for a fine mesh where $\zeta_f = 1mm$, $\zeta_c = 4mm$. ζ_f meshes the central region of the channel of length S.

Fig. 6.19 shows the dependence of the Lorentz force on the distance s between 2 and 3 dipole rings. The strongest force is produced, when the dipole rings are close together. This underlines again the advantage of a stronger field source to multiple weaker ones. The nondimensionalized Lorentz force decreases with s until it reaches

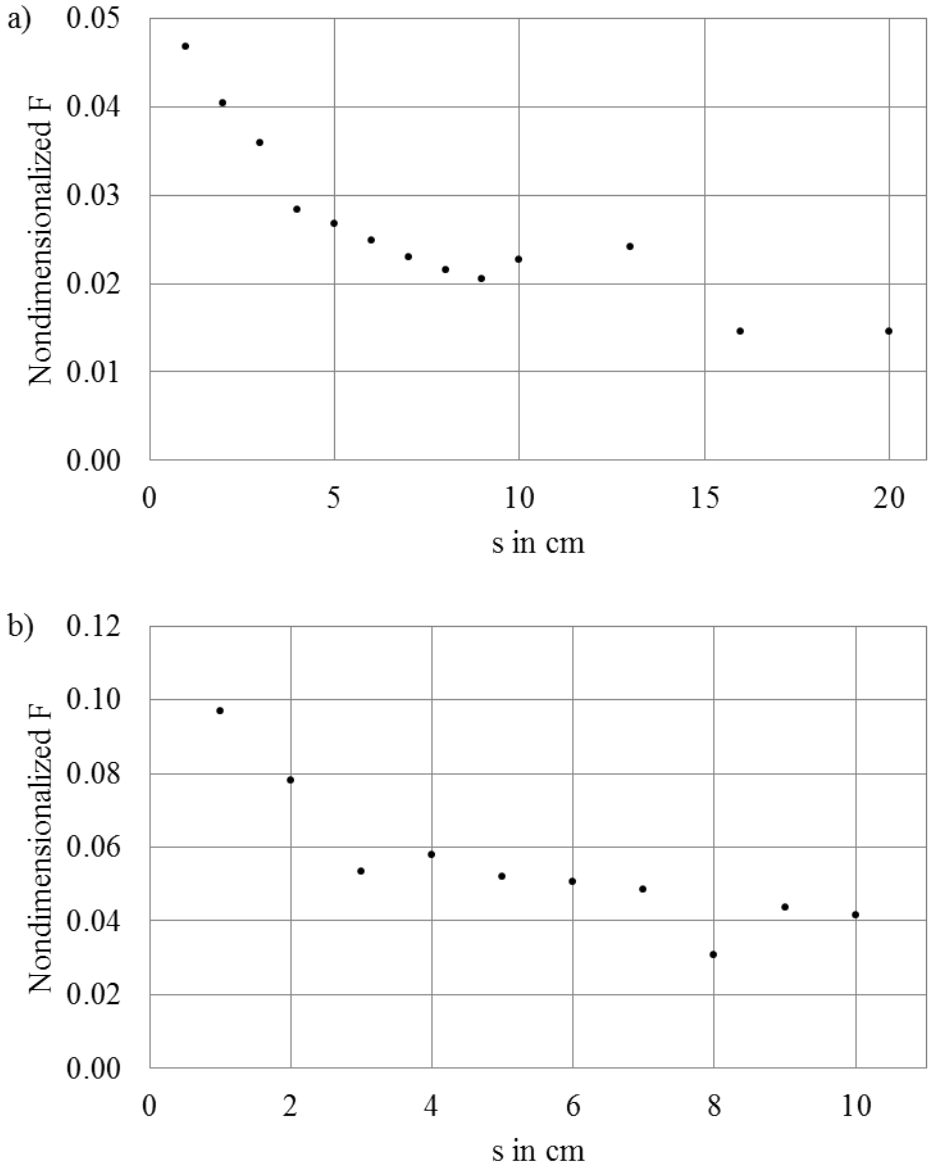

Figure 6.19: Lorentz force depending on the distance s between the respective dipole rings: a) 2 dipole rings, b) 3 dipole rings with 8 dipoles in each ring.

a minimum at $s = 90mm$ for 2 dipole rings. The force then increases by 0.004 and decreases again until it reaches a constant value, when the two dipole rings do not influence each other anymore.

The resulting optimized angles exhibit two different symmetrical cases. For the 2 dipole ring setup the first case is depicted in fig. 6.20, where the dots and contours with the same colors represent the same dipole angle values, e.g. the topmost and bottommost dipole in the first and second dipole ring are orange and have thus the same μ_i angle. The contours of the topmost dipole in the first dipole ring and the bottommost dipole in the second dipole ring have the same dark orange contour, meaning that they have the same ν_i angles. The following angles concur, for the distances $s = 10, 20, 50, 200mm$ between dipole rings [3]:

- The polar angles of opposite dipoles, i.e. $\mu_{ij} = \mu_{(i+4)j}$ where $j = 1$ or 2 (filled out dots in fig. 6.20a).
- The azimuthal anlges $\nu_{i1} = \nu_{(i+4)2}$ (thick contours around the dots in fig. 6.20a).
- Two successive azimuthal angles with different values are followed by two azimuthal angles with the same value, i.e. angles ν_{i-1} and ν_i are followed (clockwise) by $\nu_{i+1} = \nu_{i+2}$ (fig. 6.20a).

The second symmetry case is the same without the the last match and happens for $s = 40, 70, 80, 100, 130mm$. There are no consecutive angles with the same value as is indicated in fig. 6.20b.

For 3 dipole rings the force decreases steadily from $s = 10mm$ to $100mm$ with two minima at $s = 30$ and $s = 80$ (fig. 6.19). These two points might be local extrema that the algorithm found. The following angles coincide for $s = 10, 50, 60, 70mm$ in the first symmetry case (fig. 6.21):

- The polar angles of opposite dipoles in the first and third dipole ring, i.e. $\mu_{ij} = \mu_{(i+4)j}$ where $j = 1$ or 3 (orange filled out dots in fig. 6.21a).
- The polar angles of opposite dipoles in the second dipole ring, i.e. $\mu_{i2} = \mu_{(i+4)2}$ (green filled out dots in fig. 6.21a).
- The azimuthal anlges $\nu_{ij} = \nu_{(i+4)j}$ where $j = 1$ and 3 on either side of the equation (thick grey contour around the dots in fig. 6.21a).
- The azimuthal anlges $\nu_{i2} = \nu_{(i+4)2}$ and after two different $\nu_{(i-1)2} \neq \nu_{(i)2}$ follow two angles with the same value $\nu_{(i+1)2} = \nu_{(i+2)2}$ (thick blue and purple contour around the dots in fig. 6.21a).

In the second symmetry case for the 3 dipole ring setup with $s = 20, 30, 80, 90$, $100mm$ the polar angles of opposite dipoles in the first and third dipole ring show almost the same behavior as in the fist symmetry case. Only one opposite dipole

[3] The cyclic character of the problems should not be forgotten, i.e. $angle_{ij} = anlge_{(i+8)j}$.

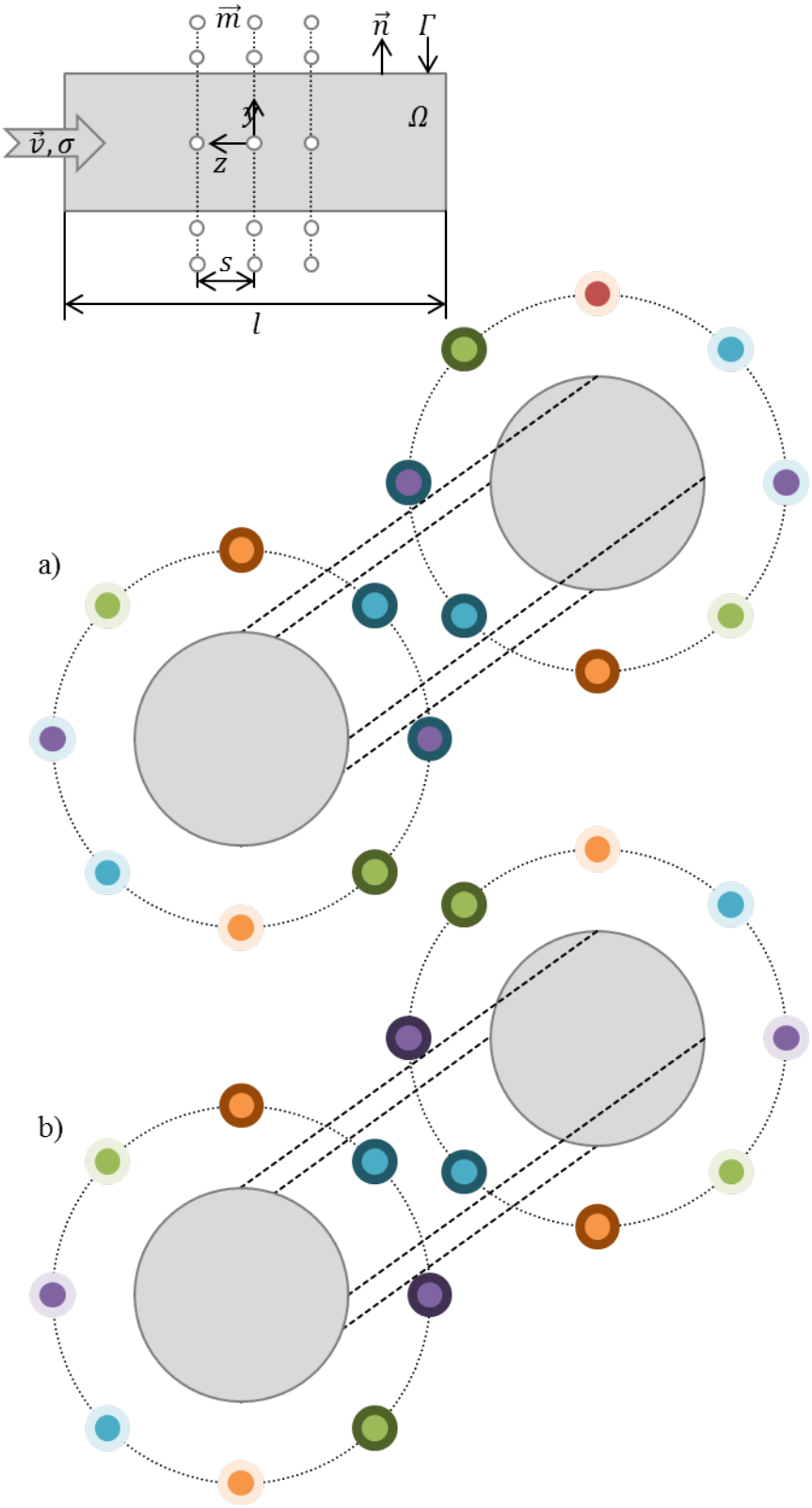

Figure 6.20: Qualitative depiction of the symmetry among the dipole orientation angles. Filled out dots represent the respective μ_i and the thicker contours to ν_i.

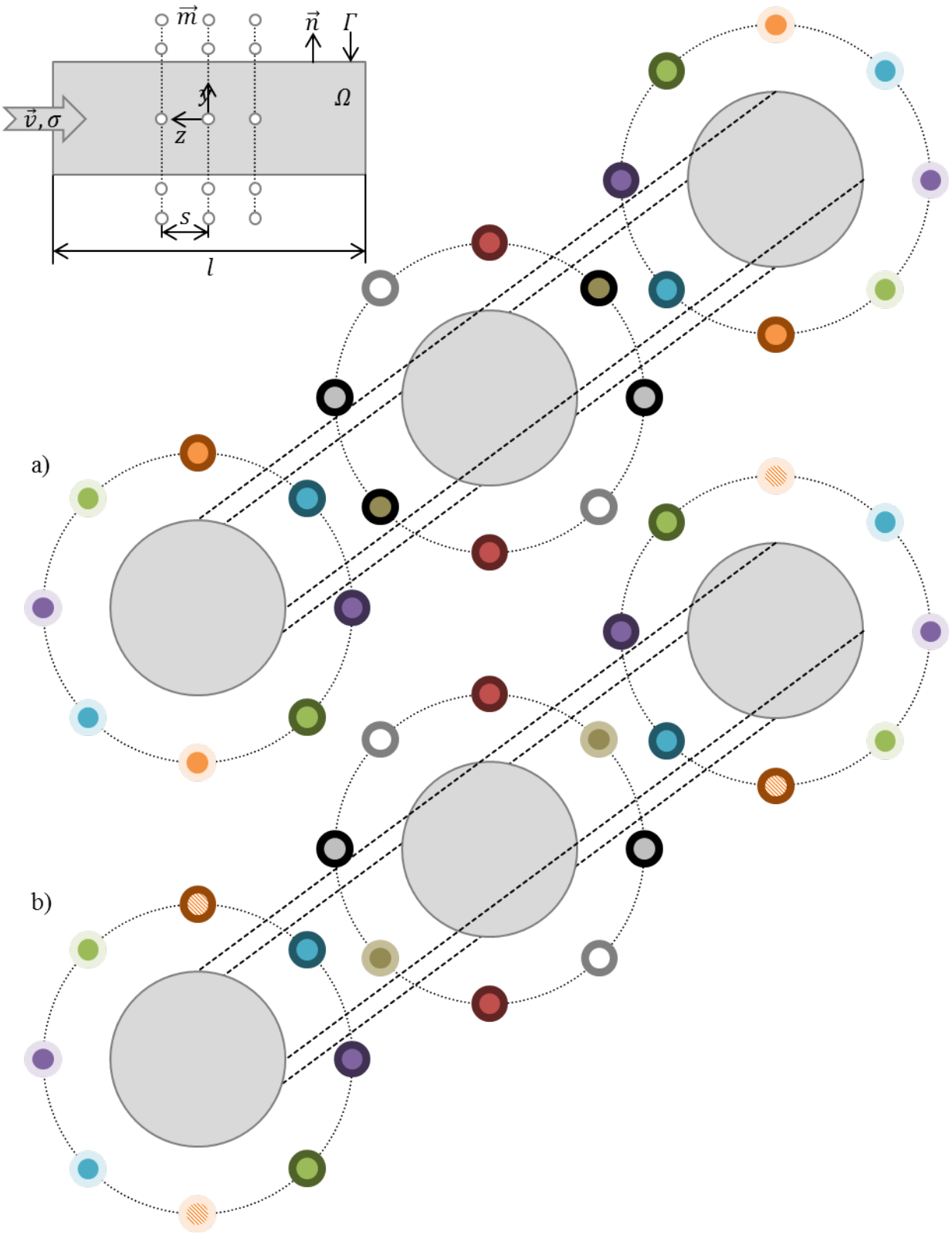

Figure 6.21: Qualitative depiction of the symmetry among the dipole orientation angles. Filled out dots represent the respective μ_i and the thicker contours to ν_i.

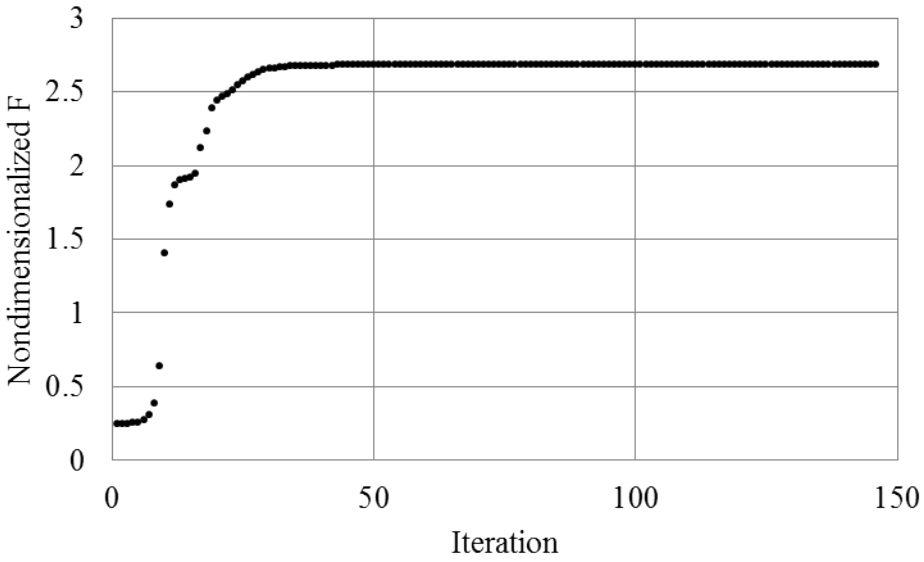

Figure 6.22: Convergence plot of the 11 dipole rings problem optimized with the gradient-ascent method in PROMETHEUS.

pair in the whole ring does not have the same value indicated by the striped orange dots in fig. 6.21b.

In both cases the $z = 0$ plane marks a symmetry plane, but the parameters in the first case are mirror-symmetric, while they are point-symmetric in the second case. The second case is a more general formulation of the first case. As a consequence a symmetry plane cannot be included in FEM simulations, which would significantly reduce the geometric volume of the problem and thus the mesh. However, it is possible to exploit the cyclic relations among the angles, which in turn reduces the number of possible optimization variables.

The uncertainty of the optimum type, i.e. local or global, makes an interpretation of these results difficult. The dipole interaction depends on the distance between the dipoles and one configuration/symmetry can be more favorable than the other at specific distances. A global optimization is necessary for final determination. However, global optimization algorithms are usually limited to a smaller number of decision variables [62].

11 dipole ring problem

The setup for $o = 11$ successive dipole rings (fig. 6.23) was chosen to test the capacity of the optimization approach and as such the number of total dipoles per ring was increased to $n = 16$. However, the distance between dipole rings s was fixed to $s = 10mm$. This means there is a total of 352 decision variables. The other geometrical parameters are analog to the other multi dipole ring problems. The PROMETHEUS model is optimized with the built-in gradient method and fig. 6.22

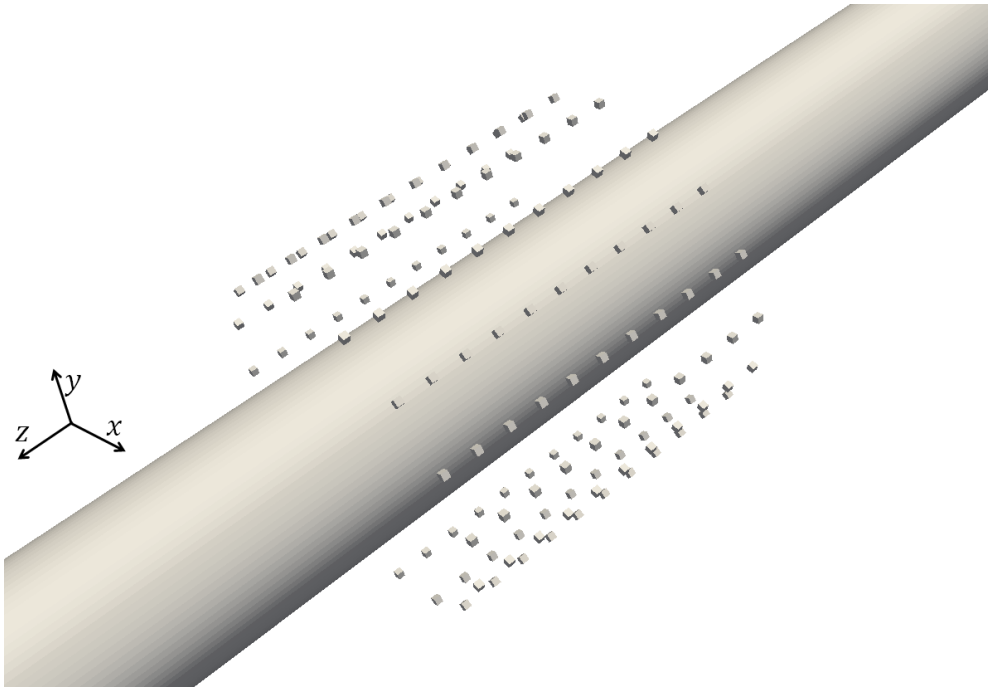

Figure 6.23: Geometrical setup of the 11 dipole rings problem. The dipoles are indicated by the small cubes.

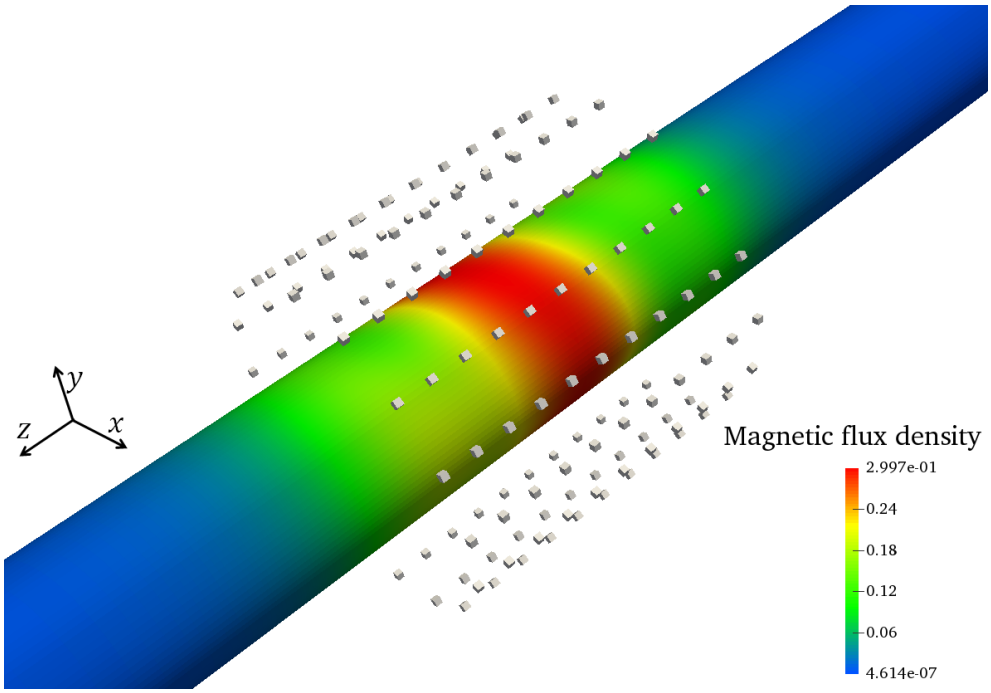

Figure 6.24: Optimized magnetic flux density in T of the 11 dipole rings problem.

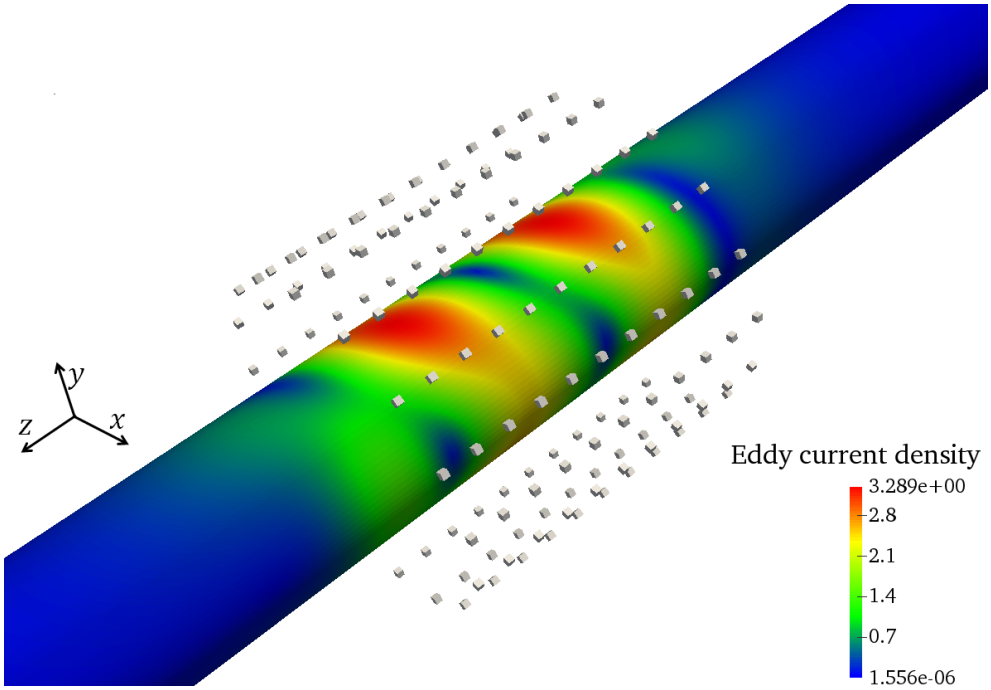

Figure 6.25: Resulting eddy current density in A/m^2 of the 11 dipole rings problem.

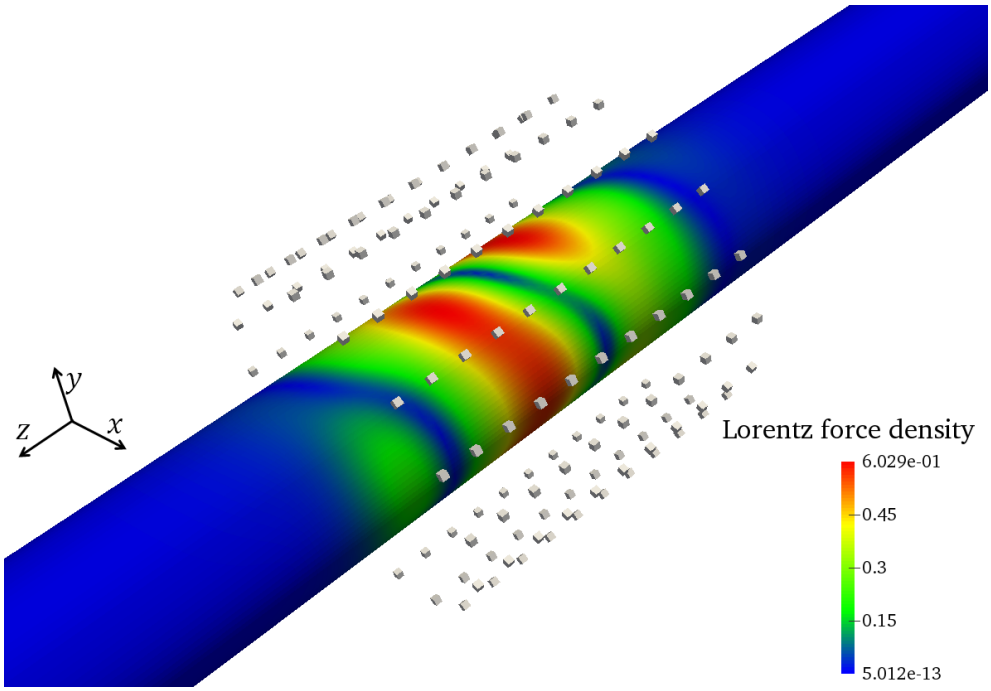

Figure 6.26: Resulting Lorentz force density in N/m^3 of the 11 dipole rings problem.

depicts the convergence plot. A maximum of the objective function is reached after 60 iterations.

Fig. 6.24-6.26 show the magnetic flux density, the eddy current density and the Lorentz force density on the cylinder surface. All physical properties exhibit a point-symmetrical behavior. The dipoles are oriented in a way that the strongest part of the magnetic field (fig. 6.24) is tilted with respect to the cylinder axis. A larger volume of the cylinder is penetrated by a strong magnetic field than it would be if the flow of the magnetic field would be perpendicular to the cylinder axis. This is reflected in all other physical properties.

The large number of dipoles could enable setups which send the magnetic field through the cylinder multiple times. However, the magnetic field concentrates only in the central part of the cylinder. All physical properties exhibit a point-symmetrical behavior consistent with the simpler $o = 2, 3$ dipole rings setups. The strongest part of the magnetic field (fig. 6.24) is tilted with respect to the cylinder axis. A larger volume of the cylinder is penetrated by a stronger magnetic field than it would be if the flow of the magnetic field were perpendicular to the cylinder axis. This is reflected in all other physical properties. Apparently, a magnet system that is tilted with respect to the cylinder axis is most efficient.

6.5 COMSOL - Realistic Magnet System

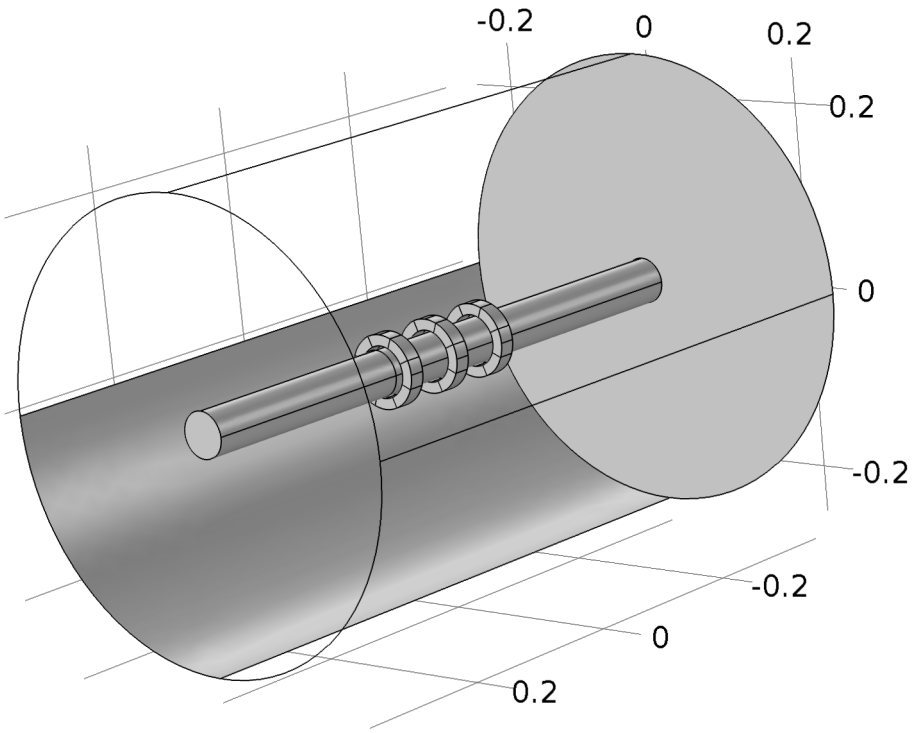

Figure 6.27: Geometry of the setup with three successive magnet rings composed of eight individual segments (units in cm).

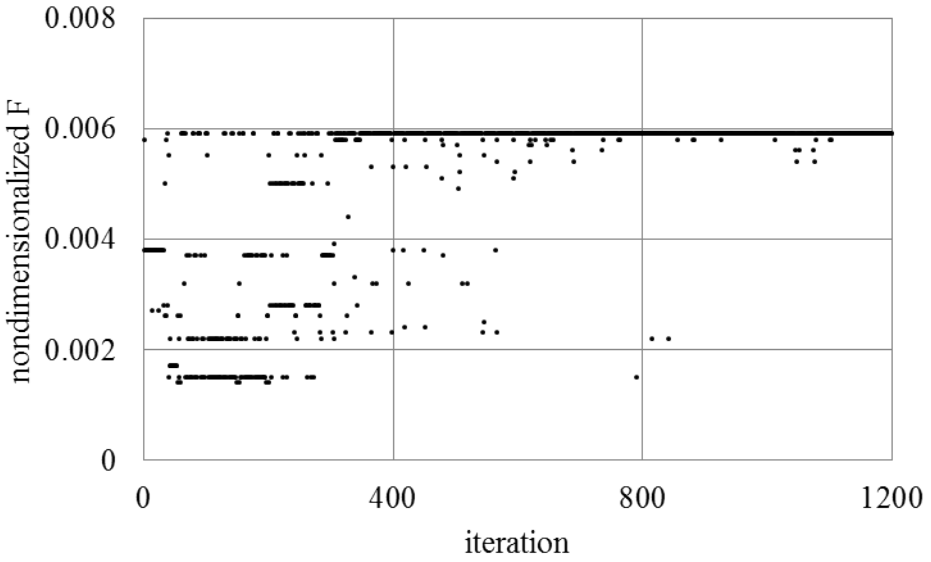

Figure 6.28: Optimization of the magnet system with the NOMAD algorithm.

The preliminary findings gained with the study of different dipole configurations are finally applied to a realistic magnet system. Unfortunately the in-house code PROMETHEUS is not able to simulate coupled setups with permanent magnets and moving bodies. COMSOL Multiphysics [10] is used to conduct the simulations in this chapter.

The conclusions drawn from the multi-dipole problems are as follows:

- For one ring of dipoles the magnetic field in a plane perpendicular to the cylinder is similar to one that a dipole placed in the center would produce (sections 6.2, 6.3).

  $\rightsquigarrow$ A realistic representation of this setup is a magnet cylinder. The number of segments is initially arbitrary. There should be enough segments to create this dipole like magnetic field, while having as few optimization parameters as possible. Magnet cylinders with 8 segments satisfactorily create the desired magnetic field, while they contribute an acceptable number of 16 decision variables, i.e. two parameters per segment.

- For multiple dipole rings the magnetic field is tilted with respect to the cylinder axis (section 6.4).

  $\rightsquigarrow$ The character of the magnetic field can be reproduced by successive magnet cylinders with different segmential orientations (or with one magnet cylinder where the segments are not in a single row but shifted in respect to each other. This generates a tilted magnetic field compared to a straight magnet cylinder).

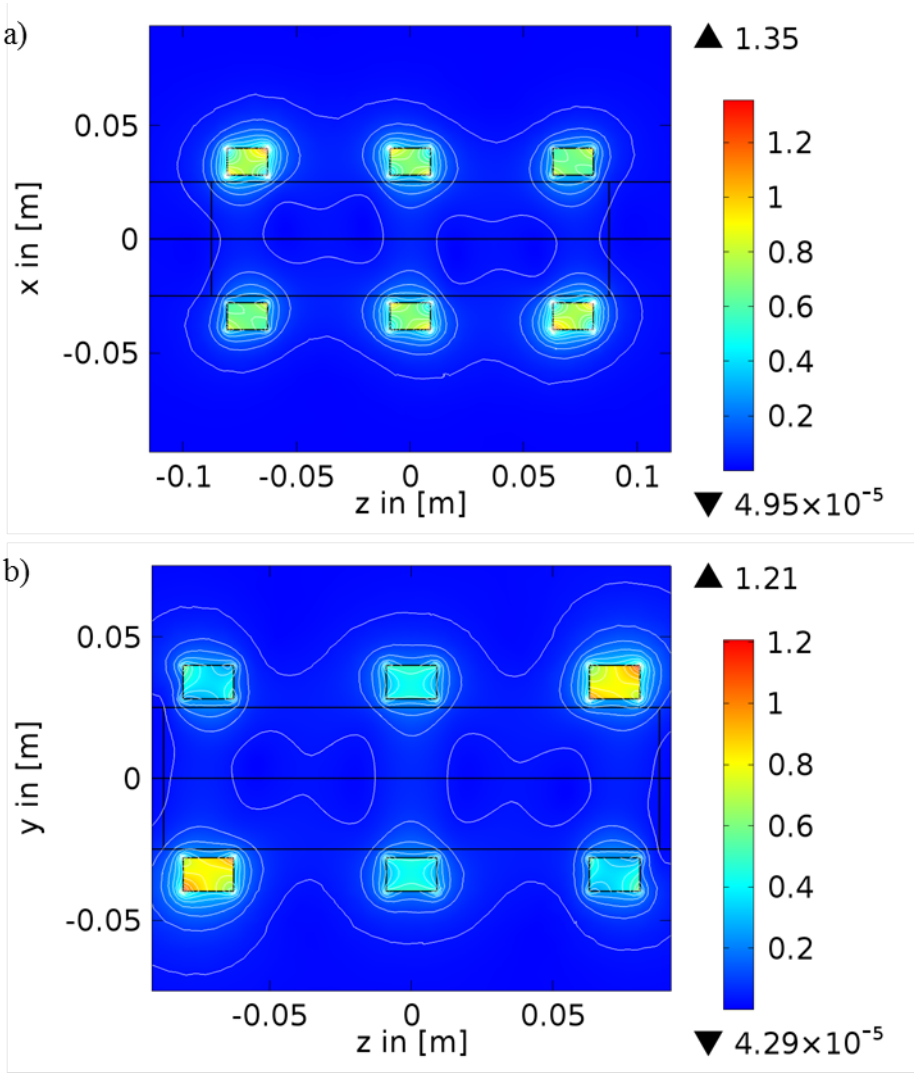

Figure 6.29: 2D plots of the magnetic field in $Tesla$ created by the optimized 3 magnet ring setup: a) cut through the xz plane and b) the zy plane.

- The Lorentz force for the 3 dipole ring problem is twice as high that for the 2 ring problem, even though the number of dipoles was increased by 1/3 (section 6.4).

  $\rightsquigarrow$ Three successive magnet rings will be used (fig. 6.27).

The measurement fluid used in the actual experiments is saltwater with a very low electric conductivity. Here the conductivity is set to $4S/m$. The water is pumped with a velocity of $5m/s$ through a channel. The measured Lorentz forces are in the range of a few μN. To detect this small force a very sensitive balance system is used. The magnet system hangs from the balance system and its sensitivity limits the weight of the magnet system to $1kg$ [12]. The density of NeFeB magnets is in the range of $7.3 - 7.5g/cm^3$. This defines the maximal volume of magnetic material that can be used. The magnets have a remanent flux density of $1T$. The distance

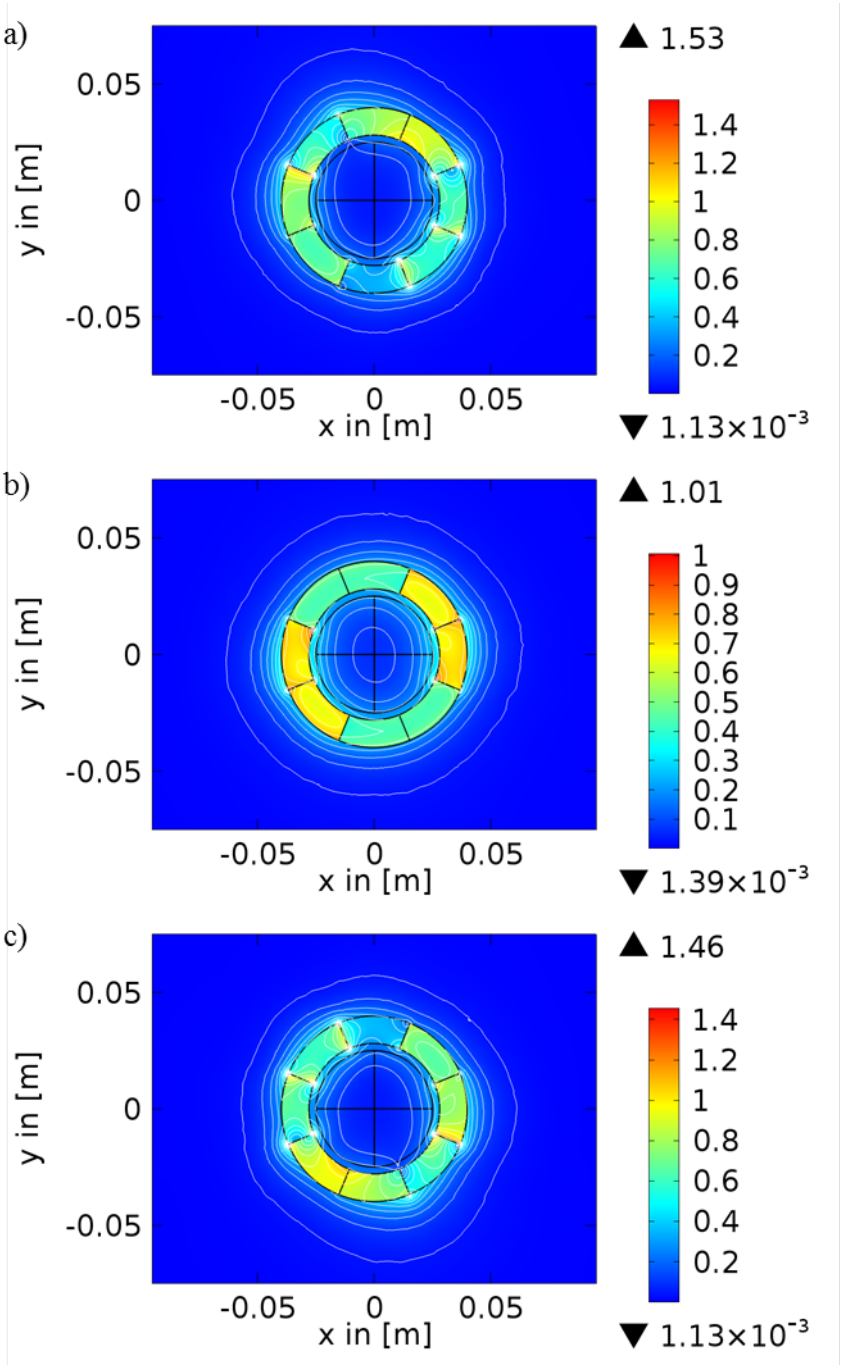

Figure 6.30: 2D plots of the magnetic field in *Tesla* created by the optimized 3 magnet ring setup: cut through the middle of the a) first ring, b) the second ring, c) the third ring.

from the fluid to the channel is $0.03cm$. It accounts for the thickness of the channel wall and an air gap. For a pipe radius of $2.5cm$ the inner radius of the magnet rings is set to $2.8cm$. The outer radius depends on the thickness of the magnet rings, which is the same for all three rings. The radius of the surrounding air domain is

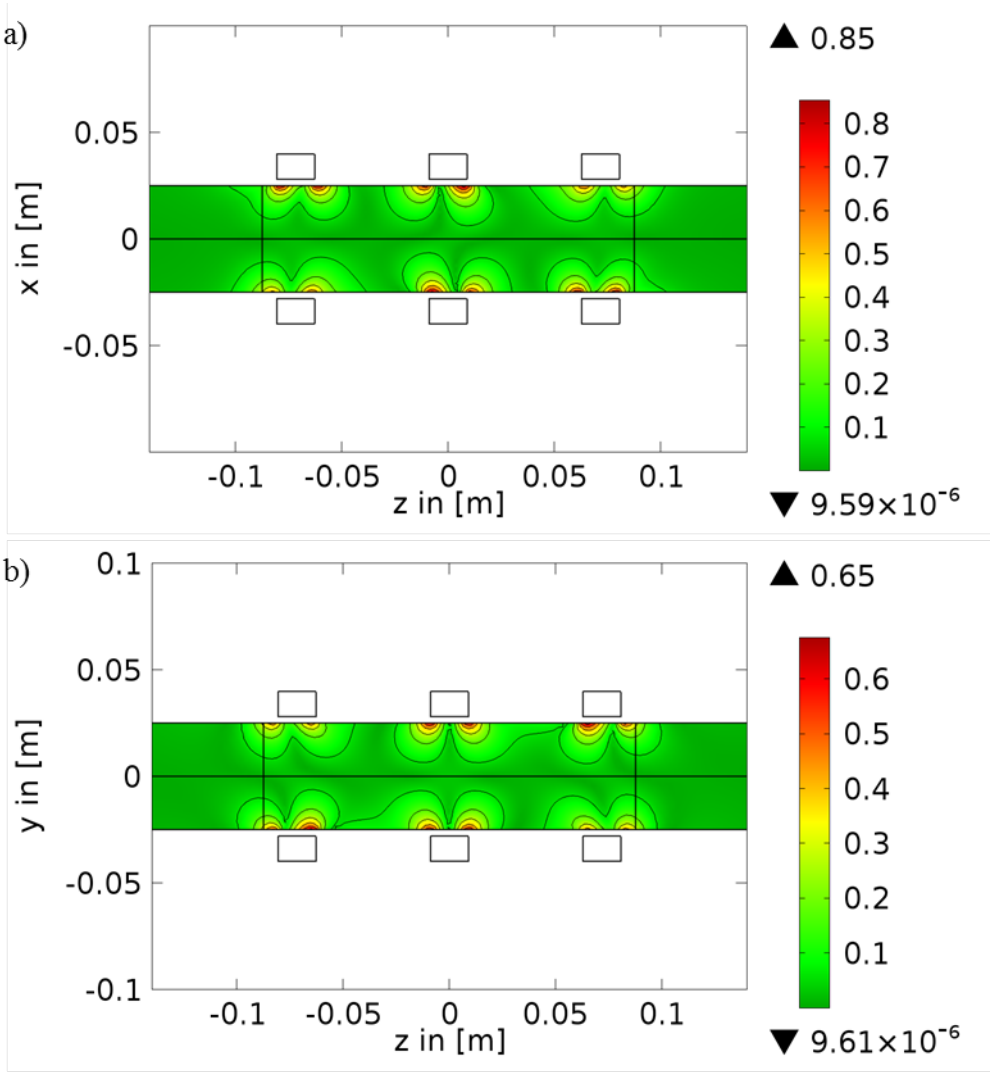

Figure 6.31: 2D plots of the eddy currents in A/m^2 created by the optimized 3 magnet ring setup: a) cut through the xz plane and b) the zy plane.

10 times larger than the pipe and the length of the pipe is $20R$ in order to account for the various geometric dimensions the magnet system can change into, i.e. slim rings with a large diameter or thick rings with a small diameter.

The optimization variables are the orientation angles of the magnetization for each segment of the magnet rings, considering the symmetric character displayed in fig. 6.21b. This reduces the number of angle variables from 48 to 20. Thus, the decision variables for $i = 1, 2, ..., 8$ dipoles per dipole ring and $j = 1, 2, 3$ the number of the respective dipole rings are the polar angles $\mu_{ij} = \mu_{(i+4)j}$ where $j = 1$ or 3 and $\mu_{i2} = \mu_{(i+4)2}$ and the azimuthal anlges $\nu_{ij} = \nu_{(i+4)j}$ where $j = 1$ and 3 and $\nu_{i2} = \nu_{(i+4)2}$. The thickness s_t of and the distance s between the magnet rings are also considered.

The optimization is done with the NOMAD algorithm. The configuration of the starting point $\mu_i = \nu_i = 0$ and the distance between the magnet rings is $s =$

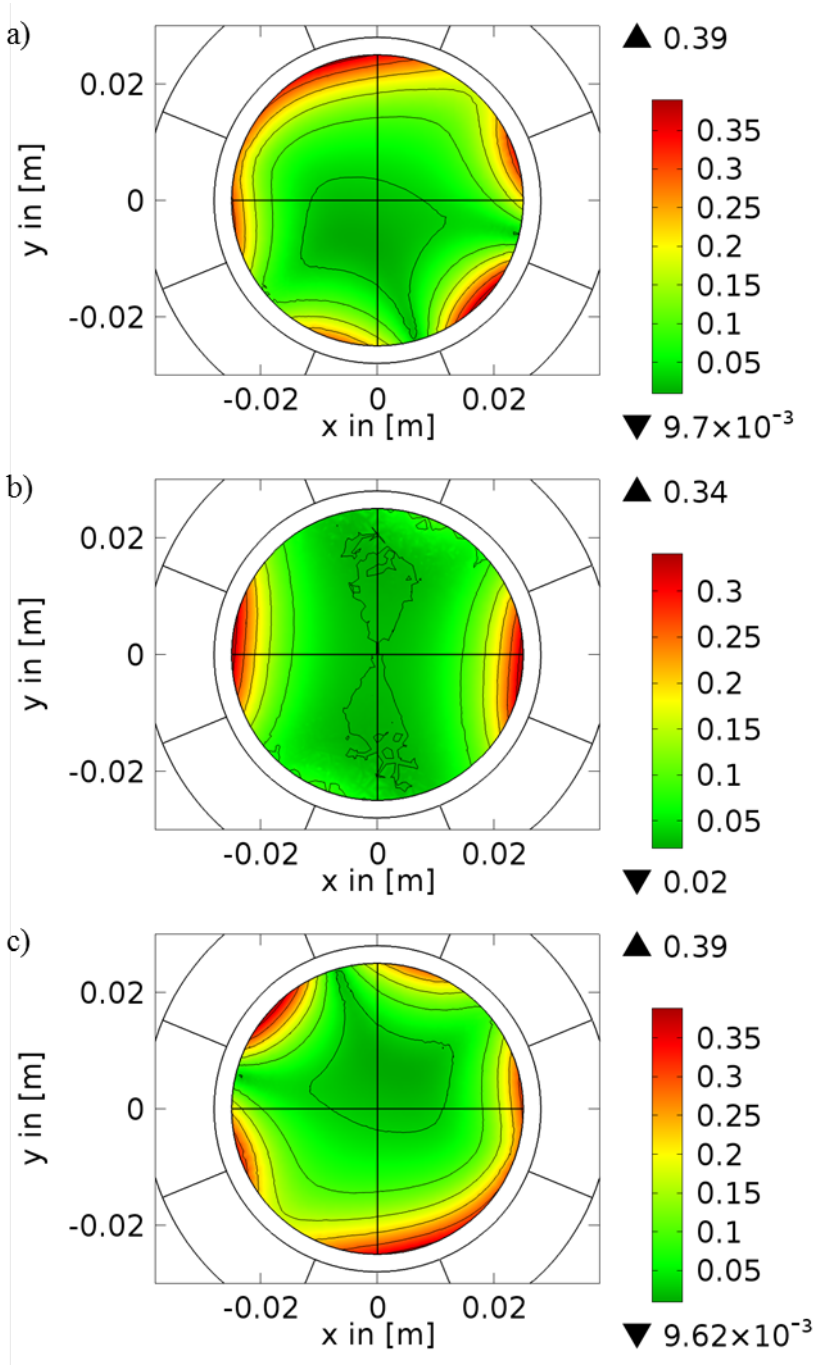

Figure 6.32: 2D plots of the eddy currents in A/m^2 created by the optimized 3 magnet ring setup: cut through the middle of the a) first ring, b) the second ring, c) the third ring.

$5cm$ and their thickness is $s_t = 5cm$. The bounds are $s = [1cm, 10cm]$ and $s_t = [0.5cm, 4.5cm]$. The initial value of the objective function is already very close to the derived maximum (fig. 6.28). The large swings in value mark changes on the thickness of the magnet rings. The small changes in magnitude belong to changes

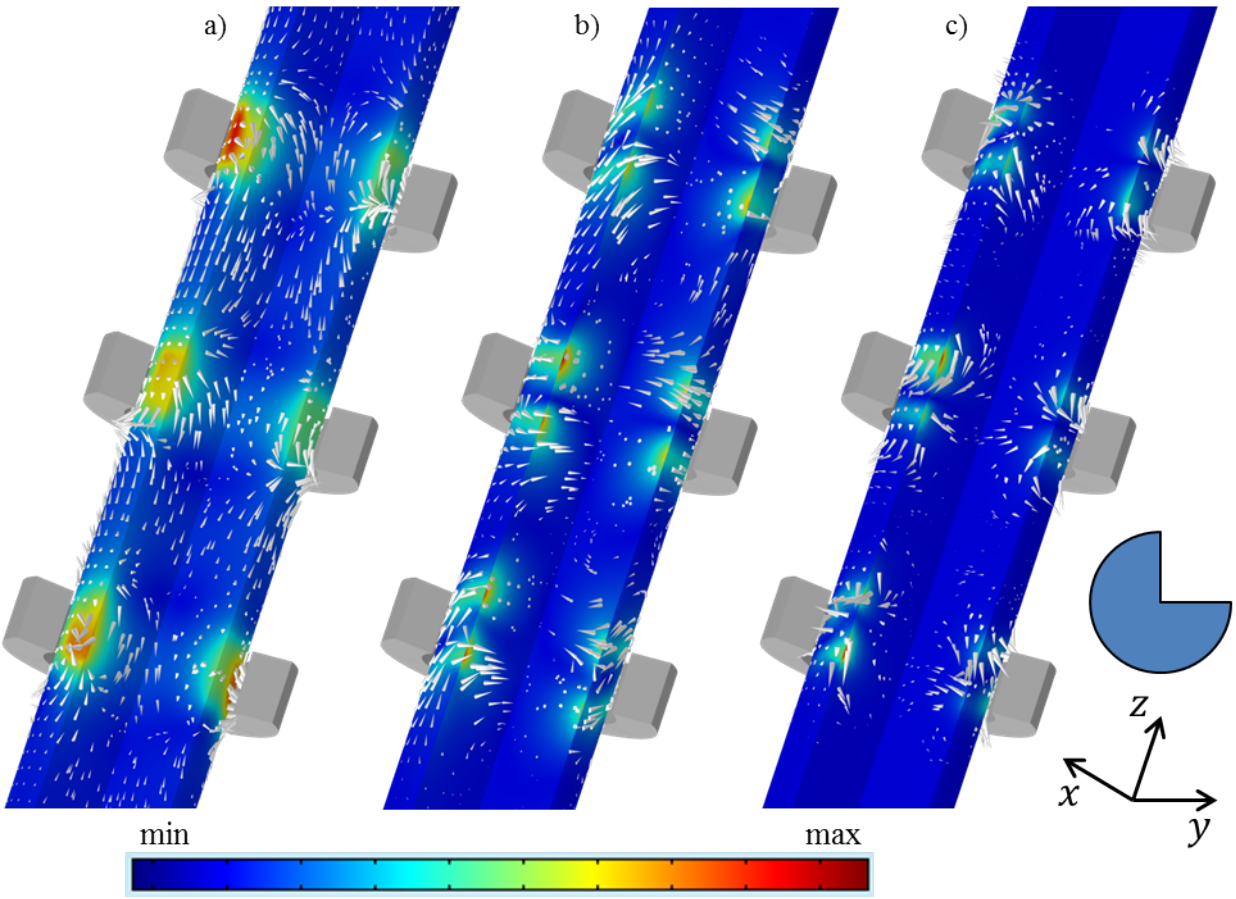

Figure 6.33: Graphical depiction of the vector fields created by the optimized magnet system. One quarter of the cylinder was cut out. The color indicates the magnitude and the arrows point into the direction of a) the magnetic field, b) eddy currents and c) Lorentz force.

in the orientation angles of the magnets.

The optimal values for the magnet rings are $s = 5.39cm$ and $s_t = 1.8cm$. The result for s is rather surprising. The multi dipole ring problems (chapter 6.4) showed that the closer the dipole rings are the stronger the Lorentz force. Here, the optimal distance between dipole ring is rather large with over $5cm$. This might be attributed to the difference between magnets and dipoles. The fast decrease of the magnetic field of a dipole makes the clustering of multiple dipoles more favorable.

The resulting magnetic field (fig. 6.29, 6.30, 6.33a) inside the cylinder alternates direction along the cylinder axis. Moving along the z-direction the magnetic field first points in z-direction. Then it changes sign in the center of each magnet ring and between the two magnet rings. The cuts through the dipole rings show two different magnetic field distributions. The middle ring has a magnetic field that enters on side of the cylinder and exits at the opposite side (fig. 6.30b). The outer magnet rings have multiple entrance and exit points of the magnetic field (fig. 6.30a,c).

The visualization of the eddy currents are not so descriptive in 2D (fig. 6.31, 6.32,

6.33b). In front and behind the magnet rings the eddy currents alternate between a clock and counterclockwise orientation across the diameter of the cylinder. The eddy currents also form loops between the magnet rings to connect the clock and counterclockwise loops.

The Lorentz force (fig. 6.33c) is maximal at the inner corners of the magnet cylinder rings, but varies along the cylinder walls. It diminishes quickly, further away from the magnet rings. The vectors of the Lorentz force form two half loops at each magnet ring. In only relatively small regions opposes the Lorentz force the movement of the cylinder, which is the component used in LFV.

The optimization of the magnet system for LFV illustrates the complex distribution of the respective vector fields and the small volumes in which the Lorentz force actually contributes to the braking force. If a weakly conducting medium is considered this bottleneck constricts further, making it difficult to have a high quality measurement signal. Here, optimization is essential to improve the method for further applications.

Chapter 7

Summary and Outlook

This chapter summarizes and concludes the main results. Additional suggestions for further study concerning practical, numerical and theoretical fields complete this work.

7.1 Summary

The contactless measurement method for conducting media Lorentz force velocimetry was numerically investigated assuming the quasi-static approximation. The goal was to increase the Lorentz force resulting from the interaction between magnet system and measurement medium approximated by a solid body, in this case a cylinder.

The basis of the optimization was an intensive study of an academic dipole problem. A variable number of magnetic dipoles was placed around the cylinder and their orientation and position was optimized. Different methods were applied, a complete analytic formulation of a specific problem was investigated and more general setups were examined with the aid of two FEM software programs and numerically optimized. The FEM software programs are the in-house code PROMETHEUS and the commercial software COMSOL Multiphysics. Their different advantages were utilized to complement and also to verify each other in the optimization.

The optimization of the problem itself is very difficult especially for increasing numbers of variables. It is often not possible to determine the type of maximum reached by the optimization algorithms. However it was always possible to attain improvement configurations compared to the initial setups.

The results of the dipole formulation gave insight into the magnetic field distribution, that can be applied the design of a practical magnet system.

The following objectives were accomplished:

- The results of [8] were reconstruction to verify the applied FEM software programs. The in-house code PROMETHEUS converged satisfyingly, making it suitable for FEM simulations in the framework of LFV.

- The asymptotic approximation was extended of from one dipole [8] to multiple dipoles. The position of the dipoles is limited to a fixed distance and

perpendicular plane with respect to the conducting cylinder axis, forming a dipole ring. This allowed the derivation of an analytic objective function for optimization. The position and orientation of the magnetic dipole moments was optimized in order to maximize the Lorentz force acting on the conductor. The dipoles clustered to one point, when their position was variable. When the dipole positions were equidistantly fixed, their optimized orientations seem to approach a continuous function.

- Different optimization algorithms were tested and compared. The analytic objective function was analytically, via the Hessian matrix, and numerically optimized. The FEM setups were optimized only numerically. The numerical optimization algorithms were a gradient method and direct search methods. The type of the attained optima, i.e. global or local optimum, depend on the number of decision variables. Guaranteed global optima were found only for a small number of variables $n < 3$.

- Conclusions from the results of the dipole problems were drawn and applied to a realistic magnet system. In the multi dipole ring setup was the force for 3 dipole rings twice as high than for 2 dipole rings, even though the number of dipoles was not doubled. Thus, a magnet system with 3 magnet cylinders was constructed, where the thickness of the magnet cylinders and distance between magnet cylinders was optimized. Furthermore, the magnet cylinders consisted of segments whose magnetic orientation also belonged to the decision variables. Here, the optimal symmetries among the multi dipole setup was used to reduce the total number of variables for the magnetic orientations from 48 to 20, significantly reducing the complexity of the optimization.

7.2 Outlook

The results leave open a wide field for further investigations, numerically and practically.

- In the introduction it was pointed out that there are other practical possibilities to improve the measurement of the Lorentz force. One of them is to exchange the magnet system with high temperature superconductors [66]. This is a very promising approach. The results of the optimization of the position of the dipoles show that it is always more favorable to use a single stronger source than multiple weaker ones. Another possible method is to shield the measurement system from outside disturbances. This raises the quality of the measurement signal by decreasing the influence of noise.

- Theoretically the analytic multi dipole problem, which was investigated here with an asymptotic approximation, can be extended to the close approximation [59], [43], where the dipoles are placed very close to the surface of the conductor. Based on the two limiting cases a general formulation can be obtained for multiple dipoles in one plane. Furthermore, an expression for

arbitrary positions might be found, allowing for the dipoles to be placed in the whole space.

- A very interesting aspect is to consider dipoles of varying strength and variable position. A minimal distance between dipoles has to be considered to avoid the clustering of dipoles in one position.

- The optimization algorithms $fminsearch$ and the gradient ascent method are not very sophisticated. Other types of algorithms can be investigated for suitability. The most important ability is the processing of a high number of variables.

Appendix A

Analytic Expression for the Lorentz Force

The components of the magnetic flux density created by a dipole, which are needed for the calculation of the Lorentz force, depend only on $\hat{z}$. The derivation of this goes as follows:

First, the rescaled coordinates (eq. 4.2) are inserted into the magnetic flux density created by a dipole (eq. 4.1).

$$\vec{B}(\vec{r'}) = \frac{\mu_0}{4\pi} \frac{3\vec{r'}(\vec{m} \cdot \vec{r'}) - \vec{m}r'^2}{r'^5}$$

with

$$\begin{aligned} \vec{r'} &= (x - H_x, y - H_y, z - H_z) \\ r' &= ((x - H_x)^2 + (y - H_y)^2 + (z - H_z)^2)^{(1/2)} \\ \vec{m} &= (m_x, m_y, m_z) \end{aligned}$$

leads to:

$$\begin{aligned} B_x(\vec{\hat{r}'}) &= \tfrac{\mu_0}{4\pi} \tfrac{3(\hat{x}-H_x)[m_x(\hat{x}-H_x)+m_y(\hat{y}-H_y)+m_z(\hat{z}-H_z)]-m_x[(\hat{x}-H_x)^2+(\hat{y}-H_y)^2+(\hat{z}-H_z)^2]}{[(\hat{x}-H_x)^2+(\hat{y}-H_y)^2+(\hat{z}-H_z)^2]^{5/2}} \\ B_y(\vec{\hat{r}'}) &= \tfrac{\mu_0}{4\pi} \tfrac{3(\hat{y}-H_y)[m_x(\hat{x}-H_x)+m_y(\hat{y}-H_y)+m_z(\hat{z}-H_z)]-m_y[(\hat{x}-H_x)^2+(\hat{y}-H_y)^2+(\hat{z}-H_z)^2]}{[(\hat{x}-H_x)^2+(\hat{y}-H_y)^2+(\hat{z}-H_z)^2]^{5/2}} \\ B_z(\vec{\hat{r}'}) &= \tfrac{\mu_0}{4\pi} \tfrac{3(\hat{z}-H_z)[m_x(\hat{x}-H_x)+m_y(\hat{y}-H_y)+m_z(\hat{z}-H_z)]-m_z[(\hat{x}-H_x)^2+(\hat{y}-H_y)^2+(\hat{z}-H_z)^2]}{[(\hat{x}-H_x)^2+(\hat{y}-H_y)^2+(\hat{z}-H_z)^2]^{5/2}}. \end{aligned}$$

Then the components of the magnetic flux density are expanded into a Taylor series around $\varepsilon = 0$. The zeroth polynomials of $B_{\hat{x}}$, $B_{\hat{y}}$ and $B_{\hat{z}}$ depend only on the translatory coordinate $\hat{z}$ and not on $\hat{x}$ or $\hat{y}$. The Taylor expansions for $i = 1, 2, ..., n$ dipoles can be expressed in a compact general form, when the vectors of the magnetic dipole moments $\vec{m}_i$ and the dipole locations $\vec{H}_i$ are inserted in polar coordinates, i.e.:

$$\vec{m}_i = \begin{pmatrix} m_{i\hat{x}} \\ m_{i\hat{y}} \\ m_{i\hat{z}} \end{pmatrix} = m \begin{pmatrix} 0 \\ \cos(\mu_i) \\ \sin(\mu_i) \end{pmatrix}, \vec{H} = \begin{pmatrix} H_{i\hat{x}} \\ H_{i\hat{y}} \\ H_{i\hat{z}} \end{pmatrix} = H \begin{pmatrix} 0 \\ \cos(\theta_i) \\ \sin(\theta_i) \end{pmatrix}$$

$$
\begin{aligned}
B_x^{(0)}(\xi_i,\hat{z}) &= \sum_{i=1}^{n} B_{ix}^{(0)}(\xi_i,\hat{z}) \\
&= \frac{\mu_0 m}{4\pi H^3}\frac{[1-2\hat{z}^2-6\hat{z}\cos\theta_i+3\cos(2\theta_i)]\cos\mu_i+3\sin(2\theta_i)\sin\mu_i}{2(1+\hat{z})^{5/2}} \\
B_y^{(0)}(\xi_i,\hat{z}) &= \sum_{i=1}^{n} B_{iy}^{(0)}(\xi_i,\hat{z}) \\
&= -\frac{\mu_0 m}{4\pi H^3}\frac{6(\hat{z}-\cos\theta_i)\sin\theta_i\cos\mu_i+[-1+2\hat{z}^2+3\cos(2\theta_i)]\sin\mu_i}{2(1+\hat{z})^{5/2}} \\
B_z^{(0)}(\xi_i,\hat{z}) &= \sum_{i=1}^{n} B_{iz}^{(0)}(\xi_i,\hat{z}) \\
&= -\frac{\mu_0 m}{4\pi H^3}\frac{[3\hat{z}\cos(\theta_i-\mu_i)+\cos(\mu_i)-2\hat{z}^2\cos(\mu_i)]}{(1+\hat{z})^{5/2}}.
\end{aligned}
\tag{A.1}
$$

With $\xi_i = \mu_0 m \gamma_i \mu_i H$ containing all other parameters. This is the special case when the orientation of the dipoles are only allowed to vary in the xy plane. The optimization in chapter 5 shows, that if the dipoles are located in this plane the optimal azimuth angle is $\nu = 90$, which is exactly here the case. The components of the magnetic flux density are more complex for arbitrary positioning (not shown here).

Only the first three orders in ε are needed for all wanted physical values $\vec{B}$, ϕ, $\vec{J}$ and $\vec{F}$. For the magnetic flux density they are:

$$
\begin{aligned}
&O(\varepsilon^{(0)}) : \vec{B}^{(0)}(\hat{z}) \\
&O(\varepsilon^{(1)}) : \vec{B}^{(1)}(\vec{\hat{r}}) \\
&O(\varepsilon^{(2)}) : \vec{B}^{(2)}(\vec{\hat{r}}).
\end{aligned}
$$

An exact expression like the one for $\vec{B}^{(0)}(\hat{z})$ (eq. A.1) is not needed for the second and third orders of the magnetic flux density. It is sufficient to know the relationship between the terms of the different orders, since the higher order terms are replaceable with $\vec{B}^{(0)}(\hat{z})$. A system of equations that associates the different order terms is gained by inserting (eq. 4.3) into Gauss law (eq. 2.1):

$$
\begin{aligned}
\nabla\cdot\vec{B} =& \frac{1}{R}\begin{pmatrix}\partial_{\hat{x}}\\ \partial_{\hat{y}}\\ \varepsilon\partial_{\hat{z}}\end{pmatrix}\cdot(\vec{B}^{(0)}+\varepsilon\vec{B}^{(1)}+\varepsilon^2\vec{B}^{(2)}+...+\varepsilon^n\vec{B}^{(n)}) \\
=& \frac{1}{R}\left(\begin{pmatrix}\partial_{\hat{x}}\\ \partial_{\hat{y}}\\ \varepsilon\partial_{\hat{z}}\end{pmatrix}\cdot\begin{pmatrix}B_{\hat{x}}^{(0)}\\ B_{\hat{y}}^{(0)}\\ B_{\hat{z}}^{(0)}\end{pmatrix}+\varepsilon\begin{pmatrix}\partial_{\hat{x}}\\ \partial_{\hat{y}}\\ \varepsilon\partial_{\hat{z}}\end{pmatrix}\cdot\begin{pmatrix}B_{\hat{x}}^{(1)}\\ B_{\hat{y}}^{(1)}\\ B_{\hat{z}}^{(1)}\end{pmatrix}+\varepsilon^2\begin{pmatrix}\partial_{\hat{x}}\\ \partial_{\hat{y}}\\ \varepsilon\partial_{\hat{z}}\end{pmatrix}\cdot\begin{pmatrix}B_{\hat{x}}^{(2)}\\ B_{\hat{y}}^{(2)}\\ B_{\hat{z}}^{(2)}\end{pmatrix}\right. \\
&\left.+...+\varepsilon^n\begin{pmatrix}\partial_{\hat{x}}\\ \partial_{\hat{y}}\\ \varepsilon\partial_{\hat{z}}\end{pmatrix}\cdot\begin{pmatrix}B_{\hat{x}}^{(n)}\\ B_{\hat{y}}^{(n)}\\ B_{\hat{z}}^{(n)}\end{pmatrix}\right)=0.
\end{aligned}
$$

Arranging the terms with respect of ε gives:

$$\begin{aligned} O(\varepsilon^{(0)}) : 0 &= \partial_{\hat{x}} B_{\hat{x}}^{(0)} + \partial_{\hat{y}} B_{\hat{y}}^{(0)} \\ O(\varepsilon^{(1)}) : 0 &= \partial_{\hat{z}} B_{\hat{z}}^{(0)} + \partial_{\hat{x}} B_{\hat{x}}^{(1)} + \partial_{\hat{y}} B_{\hat{y}}^{(1)} \\ O(\varepsilon^{(2)}) : 0 &= \partial_{\hat{z}} B_{\hat{z}}^{(1)} + \partial_{\hat{x}} B_{\hat{x}}^{(2)} + \partial_{\hat{y}} B_{\hat{y}}^{(2)}. \end{aligned} \tag{A.2}$$

The electric scalar potential inside the cylinder is derived by inserting (eq. 4.5) into $\Delta\phi = 0$ (eq. 2.20):

$$\begin{aligned} 0 =& \frac{1}{R^2}(\partial_{\hat{x}}^2 + \partial_{\hat{y}}^2 + \varepsilon^2\partial_{\hat{z}}^2)(\phi^{(0)} + \varepsilon\phi^{(1)} + \varepsilon^2\phi^{(2)} + ... + \varepsilon^n\phi^{(n)}) \\ \Rightarrow 0 =& (\partial_{\hat{x}}^2 + \partial_{\hat{y}}^2 + \varepsilon^2\partial_{\hat{z}}^2)(\phi^{(0)} + \varepsilon\phi^{(1)} + \varepsilon^2\phi^{(2)} + ... + \varepsilon^n\phi^{(n)}) \\ =& \partial_{\hat{x}}^2(\phi^{(0)} + \varepsilon\phi^{(1)} + \varepsilon^2\phi^{(2)} + ... + \varepsilon^n\phi^{(n)}) \\ &+ \partial_{\hat{y}}^2(\phi^{(0)} + \varepsilon\phi^{(1)} + \varepsilon^2\phi^{(2)} + ... + \varepsilon^n\phi^{(n)}) \\ &+ \varepsilon^2\partial_{\hat{z}}^2(\phi^{(0)} + \varepsilon\phi^{(1)} + \varepsilon^2\phi^{(2)} + ... + \varepsilon^n\phi^{(n)}) \\ =& \partial_{\hat{x}}^2\phi^{(0)} + \varepsilon\partial_{\hat{x}}^2\phi^{(1)} + \varepsilon^2\partial_{\hat{x}}^2\phi^{(2)} + ... + \varepsilon^n\partial_{\hat{x}}^2\phi^{(n)} \\ &+ \partial_{\hat{y}}^2\phi^{(0)} + \varepsilon\partial_{\hat{y}}^2\phi^{(1)} + \varepsilon^2\partial_{\hat{y}}^2\phi^{(2)} + ... + \varepsilon^n\partial_{\hat{y}}^2\phi^{(n)} \\ &+ \varepsilon^2\partial_{\hat{z}}^2\phi^{(0)} + \varepsilon^3\partial_{\hat{z}}^2\phi^{(1)} + \varepsilon^4\partial_{\hat{z}}^2\phi^{(2)} + ... + \varepsilon^{2+n}\partial_{\hat{z}}^2\phi^{(n)}. \end{aligned}$$

Arranging the terms on the order of magnitude of ε yields:

$$\begin{aligned} O(\varepsilon^{(0)}) : 0 &= \partial_{\hat{x}}^2\phi^{(0)} + \partial_{\hat{y}}^2\phi^{(0)} = (\partial_{\hat{x}}^2 + \partial_{\hat{y}}^2)\phi^{(0)} \\ O(\varepsilon^{(1)}) : 0 &= \partial_{\hat{x}}^2\phi^{(1)} + \partial_{\hat{y}}^2\phi^{(1)} = (\partial_{\hat{x}}^2 + \partial_{\hat{y}}^2)\phi^{(1)} \\ O(\varepsilon^{(2)}) : 0 &= \partial_{\hat{z}}^2\phi^{(0)} + \partial_{\hat{x}}^2\phi^{(2)} + \partial_{\hat{y}}^2\phi^{(2)} = \partial_{\hat{z}}^2\phi^{(0)} + (\partial_{\hat{x}}^2 + \partial_{\hat{y}}^2)\phi^{(2)}. \end{aligned} \tag{A.3}$$

$\phi^{(0)}$ can be determined from the first equation in eq. A.3 with the appropriate boundary conditions (eq. 2.19) when the rescaled coordinates (eq. 4.2) and $r = \hat{r}R$ are considered:

$$\begin{aligned} &\frac{\partial\phi}{\partial r} = \frac{1}{R}\frac{\partial\phi}{\partial\hat{r}} = \frac{v_z}{r}(-xB_y + yB_x) = \frac{v_z}{\hat{r}R}(-R\hat{x}B_y + R\hat{y}B_x) \\ &\Rightarrow \frac{1}{R}\frac{\partial\phi}{\partial\hat{r}} = \frac{v_z}{\hat{r}}(-\hat{x}B_y + \hat{y}B_x) \\ &\Rightarrow \frac{1}{R}\frac{\partial\phi^{(0)}}{\partial\hat{r}} = \frac{v_z}{\hat{r}}(-\hat{x}B_y^{(0)} + \hat{y}B_x^{(0)}). \end{aligned} \tag{A.4}$$

A possible expression for $\phi^{(0)}$ that solves the last equation in eq. A.4 is:

$$\phi^{(0)} = v_z R(-\hat{x}B_y^{(0)}(\hat{z}) + \hat{y}B_x^{(0)}(\hat{z})). \tag{A.5}$$

This satisfies the first equation in eq. A.3:

$$\begin{aligned} 0 &= \partial_{\hat{x}}^2\phi^{(0)} + \partial_{\hat{y}}^2\phi^{(0)} \\ &= \partial_{\hat{x}}^2(v_z R(-\hat{x}B_y^{(0)}(\hat{z}) + \hat{y}B_x^{(0)}(\hat{z}))) + \partial_{\hat{y}}^2(v_z R(-\hat{x}B_y^{(0)}(\hat{z}) + \hat{y}B_x^{(0)}(\hat{z}))) \\ &= v_z R[\partial_{\hat{x}}^2(-\hat{x}B_y^{(0)}(\hat{z}) + \hat{y}B_x^{(0)}(\hat{z})) + \partial_{\hat{y}}^2(-\hat{x}B_y^{(0)}(\hat{z}) + \hat{y}B_x^{(0)}(\hat{z}))] \\ &= v_z R[-\partial_{\hat{x}}B_y^{(0)}(\hat{z}) + \partial_{\hat{y}}B_x^{(0)}(\hat{z})] = 0. \end{aligned}$$

Inserting $\hat{y} = \hat{r}\sin(\beta)$ and $\hat{x} = \hat{r}\cos(\beta)$ and taking the derivative with respect to $\hat{r}$ gives:

$$\begin{aligned}
\frac{\partial \phi^{(0)}}{\partial \hat{r}} &= \partial_{\hat{r}}(v_z R(-\hat{x}B_y^{(0)}(\hat{z}) + \hat{y}B_x^{(0)}(\hat{z})) \\
&= v_z R(-\partial_{\hat{r}}\hat{r}\cos(a)B_y^{(0)}(\hat{z}) + \partial_{\hat{r}}\hat{r}\sin(a)B_x^{(0)}(\hat{z})) \\
&= v_z R(-\cos(a)B_y^{(0)}(\hat{z}) + \sin(a)B_x^{(0)}(\hat{z})) \\
&= v_z R(-\frac{\hat{x}}{\hat{r}}B_y^{(0)}(\hat{z}) + \frac{\hat{y}}{\hat{r}}B_x^{(0)}(\hat{z})) \\
&= \begin{pmatrix} \frac{\hat{x}}{\hat{r}} \\ \frac{\hat{y}}{\hat{r}} \\ 0 \end{pmatrix} \cdot \begin{pmatrix} -v_z B_y^{(0)} \\ v_z B_x^{(0)} \\ 0 \end{pmatrix} = (\vec{e}_x \frac{\hat{x}}{\hat{r}} + \vec{e}_y \frac{\hat{y}}{\hat{r}}) \cdot \begin{pmatrix} -v_z B_y^{(0)} \\ v_z B_x^{(0)} \\ 0 \end{pmatrix} = \vec{e}_{\hat{r}} \cdot \begin{pmatrix} -v_z B_y^{(0)} \\ v_z B_x^{(0)} \\ 0 \end{pmatrix} \\
&= \vec{e}_{\hat{r}} \cdot (\vec{v} \times \vec{B}).
\end{aligned}$$

Since there is now an expression for the zeroth component of ϕ, it can be shown that $\vec{J}^{(0)} = 0$. For this Ohm's law (eq. 2.17) is expanded by inserting eq. 4.4, eq. 4.5 and eq. 4.3:

$$\begin{aligned}
&\begin{pmatrix} J_{\hat{x}}^{(0)} \\ J_{\hat{y}}^{(0)} \\ J_{\hat{z}}^{(0)} \end{pmatrix} + \varepsilon \begin{pmatrix} J_{\hat{x}}^{(1)} \\ J_{\hat{y}}^{(1)} \\ J_{\hat{z}}^{(1)} \end{pmatrix} + \varepsilon^2 \begin{pmatrix} J_{\hat{x}}^{(2)} \\ J_{\hat{y}}^{(2)} \\ J_{\hat{z}}^{(2)} \end{pmatrix} + ... + \varepsilon^{(n)} \begin{pmatrix} J_{\hat{x}}^{(n)} \\ J_{\hat{y}}^{(n)} \\ J_{\hat{z}}^{(n)} \end{pmatrix} \\
&= \sigma \begin{pmatrix} -\frac{1}{R}\partial_{\hat{x}}(\phi^{(0)} + \varepsilon\phi^{(1)} + \varepsilon^2\phi^{(2)} + ... + \varepsilon^n\phi^{(n)}) - v_{\hat{z}}(B_{\hat{y}}^{(0)} + \varepsilon B_{\hat{y}}^{(1)} + \varepsilon^2 B_{\hat{y}}^{(2)} + ... + \varepsilon^n B_{\hat{y}}^{(n)}) \\ -\frac{1}{R}\partial_{\hat{y}}(\phi^{(0)} + \varepsilon\phi^{(1)} + \varepsilon^2\phi^{(2)} + ... + \varepsilon^n\phi^{(n)}) + v_{\hat{z}}(B_{\hat{x}}^{(0)} + \varepsilon B_{\hat{x}}^{(1)} + \varepsilon^2 B_{\hat{x}}^{(2)} + ... + \varepsilon^n B_{\hat{x}}^{(n)}) \\ -\frac{1}{R}\varepsilon\partial_{\hat{z}}(\phi^{(0)} + \varepsilon\phi^{(1)} + \varepsilon^2\phi^{(2)} + ... + \varepsilon^n\phi^{(n)}) \end{pmatrix}.
\end{aligned}$$

Arranging the terms on the order of magnitude of ε gives:

$$\begin{aligned}
O(\varepsilon^{(0)}) : \begin{pmatrix} J_{\hat{x}}^{(0)} \\ J_{\hat{y}}^{(0)} \\ J_{\hat{z}}^{(0)} \end{pmatrix} &= \sigma \begin{pmatrix} -\frac{1}{R}\partial_{\hat{x}}\phi^{(0)} - v_{\hat{z}}B_{\hat{y}}^{(0)} \\ -\frac{1}{R}\partial_{\hat{y}}\phi^{(0)} + v_{\hat{z}}B_{\hat{x}}^{(0)} \\ 0 \end{pmatrix} \\
O(\varepsilon^{(1)}) : \begin{pmatrix} J_{\hat{x}}^{(1)} \\ J_{\hat{y}}^{(1)} \\ J_{\hat{z}}^{(1)} \end{pmatrix} &= \sigma \begin{pmatrix} -\frac{1}{R}\partial_{\hat{x}}\phi^{(1)}) - v_{\hat{z}}B_{\hat{y}}^{(1)} \\ -\frac{1}{R}\partial_{\hat{y}}\phi^{(1)} + v_{\hat{z}}B_{\hat{x}}^{(1)} \\ -\frac{1}{R}\partial_{\hat{z}}\phi^{(0)} \end{pmatrix} \\
O(\varepsilon^{(2)}) : \begin{pmatrix} J_{\hat{x}}^{(2)} \\ J_{\hat{y}}^{(2)} \\ J_{\hat{z}}^{(2)} \end{pmatrix} &= \sigma \begin{pmatrix} -\frac{1}{R}\partial_{\hat{x}}\phi^{(2)} - v_{\hat{z}}B_{\hat{y}}^{(2)} \\ -\frac{1}{R}\partial_{\hat{y}}\phi^{(2)} + v_{\hat{z}}B_{\hat{x}}^{(2)} \\ -\frac{1}{R}\partial_{\hat{z}}\phi^{(1)} \end{pmatrix}.
\end{aligned} \tag{A.6}$$

Eq. A.5 is inserted into the first vector of eq. A.6, confirming that $\vec{J}^{(0)} = 0$:

$$\begin{aligned}
J_{\hat{x}}^{(0)} &= \sigma(-\frac{1}{R}\partial_{\hat{x}}\phi^{(0)} - v_{\hat{z}}B_{\hat{y}}^{(0)}(\hat{z})) \\
&= \sigma(-\frac{1}{R}\partial_{\hat{x}}v_z R(-\hat{x}B_y^{(0)}(\hat{z}) + \hat{y}B_x^{(0)}(\hat{z})) - v_{\hat{z}}B_{\hat{y}}^{(0)}(\hat{z})) \\
&= \sigma(v_z B_y^{(0)}(\hat{z}) - v_{\hat{z}}B_{\hat{y}}^{(0)}(\hat{z})) = 0 \\
J_{\hat{y}}^{(0)} &= \sigma(-\frac{1}{R}\partial_{\hat{y}}\phi^{(0)} + v_{\hat{z}}B_{\hat{x}}^{(0)}(\hat{z})) \\
&= \sigma(-\frac{1}{R}\partial_{\hat{y}}v_z R(-\hat{x}B_y^{(0)}(\hat{z}) + \hat{y}B_x^{(0)}(\hat{z})) + v_{\hat{z}}B_{\hat{x}}^{(0)}(\hat{z})) \\
&= \sigma(-v_z B_x^{(0)}(\hat{z}) + v_{\hat{z}}B_{\hat{x}}^{(0)}(\hat{z})) = 0 \\
J_{\hat{z}}^{(0)} &= \sigma(-\frac{1}{R}\partial_{\hat{z}}\phi^{(0)}) \\
&= \sigma(-\frac{1}{R}\partial_{\hat{z}}v_z R(-\hat{x}B_y^{(0)}(\hat{z}) + \hat{y}B_x^{(0)}(\hat{z}))) = 0.
\end{aligned} \tag{A.7}$$

Now $\vec{J}^{(1)}$ can be derived. For this the divergence-free character of the eddy currents are utilized by inserting eq. 4.4 into eq. 2.7:

$$\begin{aligned}
0 =& \nabla \cdot \vec{J} = \nabla \cdot (\vec{J}^{(0)} + \varepsilon\vec{J}^{(1)} + \varepsilon^2\vec{J}^{(2)} + ... + \varepsilon^n\vec{J}^{(n)}) \\
=& \nabla \cdot \vec{J}^{(0)} + \nabla \cdot \varepsilon\vec{J}^{(1)} + \nabla \cdot \varepsilon^2\vec{J}^{(2)} + ... + \nabla \cdot \varepsilon^n\vec{J}^{(n)} \\
=& \frac{1}{R^2}\begin{pmatrix}\partial_{\hat{x}}\\ \partial_{\hat{y}}\\ \varepsilon\partial_{\hat{z}}\end{pmatrix} \cdot \begin{pmatrix}J_{\hat{x}}^{(0)}\\ J_{\hat{y}}^{(0)}\\ J_{\hat{z}}^{(0)}\end{pmatrix} + \frac{\varepsilon}{R^2}\begin{pmatrix}\partial_{\hat{x}}\\ \partial_{\hat{y}}\\ \varepsilon\partial_{\hat{z}}\end{pmatrix} \cdot \begin{pmatrix}J_{\hat{x}}^{(1)}\\ J_{\hat{y}}^{(1)}\\ J_{\hat{z}}^{(1)}\end{pmatrix} \\
&+ \frac{\varepsilon^2}{R^2}\begin{pmatrix}\partial_{\hat{x}}\\ \partial_{\hat{y}}\\ \varepsilon\partial_{\hat{z}}\end{pmatrix} \cdot \begin{pmatrix}J_{\hat{x}}^{(2)}\\ J_{\hat{y}}^{(2)}\\ J_{\hat{z}}^{(2)}\end{pmatrix} + ... + \frac{\varepsilon^n}{R^2}\begin{pmatrix}\partial_{\hat{x}}\\ \partial_{\hat{y}}\\ \varepsilon\partial_{\hat{z}}\end{pmatrix} \cdot \begin{pmatrix}J_{\hat{x}}^{(n)}\\ J_{\hat{y}}^{(n)}\\ J_{\hat{z}}^{(n)}\end{pmatrix} \\
=& \frac{1}{R^2}(\partial_{\hat{x}}J_{\hat{x}}^{(0)} + \partial_{\hat{y}}J_{\hat{y}}^{(0)} + \varepsilon\partial_{\hat{z}}J_{\hat{z}}^{(0)}) + \frac{\varepsilon}{R^2}(\partial_{\hat{x}}J_{\hat{x}}^{(1)} + \partial_{\hat{y}}J_{\hat{y}}^{(1)} + \varepsilon\partial_{\hat{z}}J_{\hat{z}}^{(1)}) \\
&+ \frac{\varepsilon^2}{R^2}(\partial_{\hat{x}}J_{\hat{x}}^{(2)} + \partial_{\hat{y}}J_{\hat{y}}^{(2)} + \varepsilon\partial_{\hat{z}}J_{\hat{z}}^{(2)}) + ... + \frac{\varepsilon^n}{R^2}(\partial_{\hat{x}}J_{\hat{x}}^{(n)} + \partial_{\hat{y}}J_{\hat{y}}^{(n)} + \varepsilon\partial_{\hat{z}}J_{\hat{z}}^{(n)}).
\end{aligned}$$

Arranging the terms on the order of magnitude of ε gives:

$$\begin{aligned}
O(\varepsilon^{(0)}) : 0 &= \frac{1}{R^2}(\partial_{\hat{x}}J_{\hat{x}}^{(0)} + \partial_{\hat{y}}J_{\hat{y}}^{(0)}) \\
O(\varepsilon^{(1)}) : 0 &= \frac{1}{R^2}(\partial_{\hat{z}}J_{\hat{z}}^{(0)} + \partial_{\hat{x}}J_{\hat{x}}^{(1)} + \partial_{\hat{y}}J_{\hat{y}}^{(1)}) \\
O(\varepsilon^{(2)}) : 0 &= \frac{1}{R^2}(\partial_{\hat{z}}J_{\hat{z}}^{(1)} + \partial_{\hat{x}}J_{\hat{x}}^{(2)} + \partial_{\hat{y}}J_{\hat{y}}^{(2)}).
\end{aligned} \tag{A.8}$$

With $\vec{J}^{(0)} = 0$ the second equation of eq. A.8 reduces to:

$$0 = \partial_{\hat{x}}J_{\hat{x}}^{(1)} + \partial_{\hat{y}}J_{\hat{y}}^{(1)}.$$

In the special case that the current is planar and non-rotational, it can be represented by a scalar stream function Ψ. The stream function are the streamlines which are tangential to the 2D current $\vec{J}^{(1)}_{2D} = (J^{(1)}_{\hat{x}}, J^{(1)}_{\hat{y}})$. The relation between the components $J^{(1)}_{\hat{x}}$, $J^{(1)}_{\hat{y}}$ and Ψ is:

$$J^{(1)}_{\hat{x}} = \frac{\partial \Psi}{\partial \hat{y}} \text{ and } J^{(1)}_{\hat{y}} = -\frac{\partial \Psi}{\partial \hat{x}}. \tag{A.9}$$

Using the expressions for $J^{(1)}_{\hat{x}}$ and $J^{(1)}_{\hat{y}}$ from the second vector in eq. A.6 gives:

$$\begin{aligned} J^{(1)}_{\hat{x}} &= \sigma(-\frac{1}{R}\partial_{\hat{x}}\phi^{(1)} - v_{\hat{z}}B^{(1)}_{\hat{y}}) = \frac{\partial \Psi}{\partial \hat{y}} \\ J^{(1)}_{\hat{y}} &= \sigma(-\frac{1}{R}\partial_{\hat{y}}\phi^{(1)} + v_{\hat{z}}B^{(1)}_{\hat{x}}) = -\frac{\partial \Psi}{\partial \hat{x}}. \end{aligned}$$

Considering the irrotationality of $\vec{J}^{(1)}_{2D}$ and the second equation of eq. A.2 a Poisson equation for the stream function Ψ is derived:

$$\begin{aligned} \nabla_{2D} \times \vec{J}^{(1)}_{2D} &= \partial_{\hat{y}} J^{(1)}_{\hat{x}} - \partial_{\hat{x}} J^{(1)}_{\hat{y}} = \partial^2_{\hat{y}}\Psi + \partial^2_{\hat{x}}\Psi \\ &= \partial_{\hat{y}}\sigma(-\frac{1}{R}\partial_{\hat{x}}\phi^{(1)} - v_{\hat{z}}B^{(1)}_{\hat{y}}) - \partial_{\hat{x}}\sigma(-\frac{1}{R}\partial_{\hat{y}}\phi^{(1)} + v_{\hat{z}}B^{(1)}_{\hat{x}}) \\ &= \sigma(-\frac{1}{R}\partial_{\hat{y}}\partial_{\hat{x}}\phi^{(1)} - \partial_{\hat{y}}v_{\hat{z}}B^{(1)}_{\hat{y}} + \frac{1}{R}\partial_{\hat{x}}\partial_{\hat{y}}\phi^{(1)} - \partial_{\hat{x}}v_{\hat{z}}B^{(1)}_{\hat{x}}) \\ &= \sigma(\frac{1}{R}(-\partial^2_{\hat{y}\hat{x}}\phi^{(1)} + \partial^2_{\hat{x}\hat{y}}\phi^{(1)}) - v_{\hat{z}}\partial_{\hat{y}}B^{(1)}_{\hat{y}} - v_{\hat{z}}\partial_{\hat{x}}B^{(1)}_{\hat{x}}) \\ &= -\sigma v_{\hat{z}}(\partial_{\hat{y}}B^{(1)}_{\hat{y}} + \partial_{\hat{x}}B^{(1)}_{\hat{x}}) \\ &= \sigma v_{\hat{z}}(\partial_{\hat{z}}B^{(0)}_{\hat{z}}) \\ \Rightarrow \Delta_{2D}\Psi &= \sigma v_{\hat{z}}(\partial_{\hat{z}}B^{(0)}_{\hat{z}}). \end{aligned}$$

The Laplacian in 2D in polar coordinates is:

$$\Delta_{2D} = \frac{1}{\hat{r}}\partial_{\hat{r}}(\hat{r}\partial_{\hat{r}}) + \frac{1}{\hat{r}^2}\partial^2_{\hat{\phi}}$$

since the symmetry of the cylinder implies that Ψ depends only in the radial coordinate $\hat{r}$, i.e. $\Psi = \Psi(\hat{r})$. The terms of the Poisson equation for Ψ can then be separated by the variables $\hat{r}$ and $\hat{z}$ where each term is equal to the separation constant C. The integration leads to an expression for Ψ depending on the integration

constants a and b:

$$\begin{aligned}
&\frac{1}{\hat{r}}\partial_{\hat{r}}(\hat{r}\partial_{\hat{r}}\Psi) = \sigma v_{\hat{z}}(\partial_{\hat{z}}B_{\hat{z}}^{(0)}) =: C \\
\Rightarrow\ &\frac{1}{\hat{r}}\partial_{\hat{r}}(\hat{r}\partial_{\hat{r}}\Psi) = C \\
\Rightarrow\ &\int d(\hat{r}\partial_{\hat{r}}\Psi) = C\int \hat{r}d\hat{r} \\
&\Rightarrow \hat{r}\partial_{\hat{r}}\Psi = C\frac{1}{2}\hat{r}^2 + a \\
&\Rightarrow \int d\Psi = \int C\frac{1}{2}\hat{r} + a\frac{1}{\hat{r}}d\hat{r} \\
&\Rightarrow \Psi = C\frac{1}{4}\hat{r}^2 + a\ln\hat{r} + b.
\end{aligned}$$

The term $a\ln\hat{r} = 0$ in order to avoid singularity.

The boundary condition $\Psi(\hat{r}=1) = 0$ at the surface of the cylinder specifies the integration b:

$$\Psi(\hat{r}=1) = C\frac{1}{4} + b = 0 \Rightarrow b = -\frac{C}{4}.$$

Thus, the whole expression for Ψ is:

$$\Psi = \frac{A}{4}\hat{r}^2 - \frac{A}{4} = \frac{A}{4}(\hat{r}^2-1) = \frac{\sigma v_{\hat{z}}}{4}(\hat{r}^2-1)\partial_{\hat{z}}B_{\hat{z}}^{(0)}.$$

Ψ can now be reinserted into eq. A.9 to derive $J_{\hat{x}}^{(1)}$ and $J_{\hat{y}}^{(1)}$ and eq. A.5 to derive $J_{\hat{z}}^{(1)}$:

$$\begin{aligned}
J_{\hat{x}}^{(1)} =&\partial_{\hat{y}}\Psi \\
=&\partial_{\hat{y}}\frac{\sigma v_{\hat{z}}}{4}(\hat{r}^2-1)\partial_{\hat{z}}B_{\hat{z}}^{(0)} \\
=&\frac{\sigma v_{\hat{z}}}{4}\partial_{\hat{z}}B_{\hat{z}}^{(0)}\partial_{\hat{y}}(\hat{r}^2-1) \\
J_{\hat{y}}^{(1)} =&-\partial_{\hat{x}}\Psi \\
=&\partial_{\hat{x}}\frac{\sigma v_{\hat{z}}}{4}(\hat{r}^2-1)\partial_{\hat{z}}B_{\hat{z}}^{(0)} \\
=&\frac{\sigma v_{\hat{z}}}{4}\partial_{\hat{z}}B_{\hat{z}}^{(0)}\partial_{\hat{x}}(\hat{r}^2-1) \\
J_{\hat{z}}^{(1)} =&-\frac{\sigma}{R}\partial_{\hat{z}}\phi^{(0)} \\
=&-\frac{\sigma}{R}\partial_{\hat{z}}v_z R(-\hat{x}B_y^{(0)}(\hat{z}) + \hat{y}B_x^{(0)}(\hat{z})) \\
=&\sigma v_z\partial_{\hat{z}}(\hat{x}B_y^{(0)}(\hat{z}) - \hat{y}B_x^{(0)}(\hat{z})).
\end{aligned} \tag{A.10}$$

The calculation of $\vec{J}^{(2)}$ requires the gradient in cylinder coordinates:

$$\nabla_{cyl}\cdot = (\frac{1}{\hat{r}}\partial_{\hat{r}}\hat{r}, \frac{1}{\hat{r}}\partial_{\hat{\phi}}, \partial_{\hat{z}})\cdot .$$

The divergence of $\vec{J}^{(2)}$ in Cartesian and polar coordinates is:

$$\begin{aligned}
\nabla \cdot \vec{J}^{(2)} &= \begin{pmatrix} \partial_{\hat{x}} \\ \partial_{\hat{y}} \\ \partial_{\hat{z}} \end{pmatrix} \cdot \begin{pmatrix} J^{(2)}_{\hat{x}} \\ J^{(2)}_{\hat{y}} \\ J^{(2)}_{\hat{z}} \end{pmatrix} = \begin{pmatrix} \frac{1}{\hat{r}} \partial_{\hat{r}} \hat{r} \\ \frac{1}{\hat{r}} \partial_{\hat{\phi}} \\ \partial_{\hat{z}} \end{pmatrix} \cdot \begin{pmatrix} J^{(2)}_{\hat{r}} \\ J^{(2)}_{\hat{\phi}} \\ J^{(2)}_{\hat{z}} \end{pmatrix} \\
\Rightarrow \partial_{\hat{x}} J^{(2)}_{\hat{x}} + \partial_{\hat{y}} J^{(2)}_{\hat{y}} + \partial_{\hat{z}} J^{(2)}_{\hat{z}} &= \frac{1}{\hat{r}} \partial_{\hat{r}} (\hat{r} J^{(2)}_{\hat{r}}) + \frac{1}{\hat{r}} \partial_{\hat{\phi}} J^{(2)}_{\hat{\phi}} + \partial_{\hat{z}} J^{(2)}_{\hat{z}} \\
\Rightarrow \partial_{\hat{x}} J^{(2)}_{\hat{x}} + \partial_{\hat{y}} J^{(2)}_{\hat{y}} &= \frac{1}{\hat{r}} \partial_{\hat{r}} (\hat{r} J^{(2)}_{\hat{r}}) + \frac{1}{\hat{r}} \partial_{\hat{\phi}} J^{(2)}_{\hat{\phi}}.
\end{aligned}$$

An expression for $J^{(2)}_{\phi}$ is now obtained, assuming that $\vec{J}^{(2)}$ has no radial component (eq. 2.18) with the third equation of eq. A.8 and eq. A.10, followed by an integration:

$$\begin{aligned}
\Rightarrow \partial_{\hat{x}} J^{(2)}_{\hat{x}} + \partial_{\hat{y}} J^{(2)}_{\hat{y}} = \frac{1}{\hat{r}} \partial_{\phi} J^{(2)}_{\phi} &= -\partial_{\hat{z}} J^{(1)}_{\hat{z}} \\
&= \partial_{\hat{z}} \frac{\sigma}{R} \partial_{\hat{z}} \phi^{(0)} \\
&= \frac{\sigma}{R} \partial^2_{\hat{z}} v_z R(-\hat{x} B^{(0)}_{\hat{y}}(\hat{z}) + \hat{y} B^{(0)}_{\hat{x}}(\hat{z})) \\
&= -\sigma v_z (\hat{r} \cos\phi \partial^2_{\hat{z}} B^{(0)}_{\hat{y}}(\hat{z}) - \hat{r} \sin\phi \partial^2_{\hat{z}} B^{(0)}_{\hat{x}}(\hat{z})) \\
\Rightarrow \partial_{\phi} J^{(2)}_{\phi} &= -\sigma v_z \hat{r}^2 (\cos\phi \partial^2_{\hat{z}} B^{(0)}_{\hat{y}}(\hat{z}) - \sin\phi \partial^2_{\hat{z}} B^{(0)}_{\hat{x}}(\hat{z})) \\
\Rightarrow J^{(2)}_{\phi} &= -\sigma v_z \hat{r}^2 (\sin\phi \partial^2_{\hat{z}} B^{(0)}_{\hat{y}}(\hat{z}) + \cos\phi \partial^2_{\hat{z}} B^{(0)}_{\hat{x}}(\hat{z})).
\end{aligned}$$

The angular component of $\vec{J}^{(2)}$ can be converted into the $\hat{x}$ and $\hat{y}$ components with the unit vectors $\vec{e}_{\phi}$, $\vec{e}_{\hat{x}}$ and $\vec{e}_{\hat{y}}$:

$$\begin{aligned}
\vec{e}_{\phi} &= -\sin\phi \vec{e}_{\hat{x}} + \cos\phi \vec{e}_{\hat{y}} \\
J^{(2)}_{\phi} \vec{e}_{\phi} &= J^{(2)}_{\hat{x}} \vec{e}_{\hat{x}} + J^{(2)}_{\hat{y}} \vec{e}_{\hat{y}} = -\sin\phi J^{(2)}_{\phi} \vec{e}_{\hat{x}} + \cos\phi J^{(2)}_{\phi} \vec{e}_{\hat{y}}
\end{aligned}$$

to:

$$\begin{aligned}
J^{(2)}_{\hat{x}} &= -\sin\phi J^{(2)}_{\phi} \\
&= \sigma v_z \hat{r}^2 (\sin^2\phi \partial^2_{\hat{z}} B^{(0)}_{\hat{y}}(\hat{z}) + \sin\phi\cos\phi \partial^2_{\hat{z}} B^{(0)}_{\hat{x}}(\hat{z})) \\
J^{(2)}_{y} &= \cos\phi J^{(2)}_{\phi} \\
&= -\sigma v_z \hat{r}^2 (\sin\phi\cos\phi \partial^2_{\hat{z}} B^{(0)}_{\hat{y}}(\hat{z}) + \cos^2\phi \partial^2_{\hat{z}} B^{(0)}_{\hat{x}}(\hat{z})).
\end{aligned} \tag{A.11}$$

These are all the required components to finally derive the Lorentz force. Eq. 2.14 specifies only the z component of the Lorentz force to be necessary, which depends on the $\hat{x}$ and $\hat{y}$ components of $\vec{J}$ and $\vec{B}$:

$$F = \int (J_x B_y - J_y B_x) d\Omega. \tag{A.12}$$

The components of the eddy current density and the magnetic flux density are expanded according to eq. 4.3 and eq. 4.4, which shows the dependence of the Lorentz

force on ε:

$$\begin{aligned}
F =&F^{(0)} + \varepsilon F^{(1)} + \varepsilon^2 F^{(2)} + ... + \varepsilon^n F^{(n)} \\
=&\int (J_{\hat{x}} B_{\hat{y}} - J_{\hat{y}} B_{\hat{x}}) d\Omega \\
=&\int ((J_{\hat{x}}^{(0)} + \varepsilon J_{\hat{x}}^{(1)} + \varepsilon^2 J_{\hat{x}}^{(2)} + ... + \varepsilon^n J_{\hat{x}}^{(n)})(B_{\hat{y}}^{(0)} + \varepsilon B_{\hat{y}}^{(1)} + \varepsilon^2 B_{\hat{y}}^{(2)} + ... + \varepsilon^n B_{\hat{y}}^{(n)})) \\
&- (J_{\hat{y}}^{(0)} + \varepsilon J_{\hat{y}}^{(1)} + \varepsilon^2 J_{\hat{y}}^{(2)} + ... + \varepsilon^n J_{\hat{y}}^{(n)})(B_{\hat{x}}^{(0)} + \varepsilon B_{\hat{x}}^{(1)} + \varepsilon^2 B_{\hat{x}}^{(2)} + ... + \varepsilon^n B_{\hat{x}}^{(n)}) d\Omega \\
=&\int (J_{\hat{x}}^{(0)}(B_{\hat{y}}^{(0)} + \varepsilon B_{\hat{y}}^{(1)} + \varepsilon^2 B_{\hat{y}}^{(2)} + ... + \varepsilon^n B_{\hat{y}}^{(n)}) \\
&+ \varepsilon J_{\hat{x}}^{(1)}(B_{\hat{y}}^{(0)} + \varepsilon B_{\hat{y}}^{(1)} + \varepsilon^2 B_{\hat{y}}^{(2)} + ... + \varepsilon^n B_{\hat{y}}^{(n)}) \\
&+ \varepsilon^2 J_{\hat{x}}^{(2)}(B_{\hat{y}}^{(0)} + \varepsilon B_{\hat{y}}^{(1)} + \varepsilon^2 B_{\hat{y}}^{(2)} + ... + \varepsilon^n B_{\hat{y}}^{(n)}) \\
&+ ... + \varepsilon^n J_{\hat{x}}^{(n)}(B_{\hat{y}}^{(0)} + \varepsilon B_{\hat{y}}^{(1)} + \varepsilon^2 B_{\hat{y}}^{(2)} + ... + \varepsilon^n B_{\hat{y}}^{(n)}) \\
&- J_{\hat{y}}^{(0)}(B_{\hat{x}}^{(0)} + \varepsilon B_{\hat{x}}^{(1)} + \varepsilon^2 B_{\hat{x}}^{(2)} + ... + \varepsilon^n B_{\hat{x}}^{(n)}) \\
&+ \varepsilon J_{\hat{y}}^{(1)}(B_{\hat{x}}^{(0)} + \varepsilon B_{\hat{x}}^{(1)} + \varepsilon^2 B_{\hat{x}}^{(2)} + ... + \varepsilon^n B_{\hat{x}}^{(n)}) \\
&+ \varepsilon^2 J_{\hat{y}}^{(2)}(B_{\hat{x}}^{(0)} + \varepsilon B_{\hat{x}}^{(1)} + \varepsilon^2 B_{\hat{x}}^{(2)} + ... + \varepsilon^n B_{\hat{x}}^{(n)}) \\
&+ ... + \varepsilon^n J_{\hat{y}}^{(n)}(B_{\hat{x}}^{(0)} + \varepsilon B_{\hat{x}}^{(1)} + \varepsilon^2 B_{\hat{x}}^{(2)} + ... + \varepsilon^n B_{\hat{x}}^{(n)})) d\Omega.
\end{aligned}$$

Arranging the terms on the order of magnitude of ε and considering that $\vec{J}^{(0)} = (0,0,0)$ (eq. A.7) gives:

$$\begin{aligned}
O(\varepsilon^{(0)}) : F^{(0)} =& \int J_{\hat{x}}^{(0)} B_{\hat{y}}^{(0)} - J_{\hat{y}}^{(0)} B_{\hat{x}}^{(0)} d\Omega \\
=&0 \\
O(\varepsilon^{(1)}) : F^{(1)} =& \int J_{\hat{x}}^{(0)} B_{\hat{y}}^{(1)} + J_{\hat{x}}^{(1)} B_{\hat{y}}^{(0)} - J_{\hat{y}}^{(0)} B_{\hat{x}}^{(1)} - J_{\hat{y}}^{(1)} B_{\hat{x}}^{(0)} d\Omega \\
=& \int J_{\hat{x}}^{(1)} B_{\hat{y}}^{(0)} - J_{\hat{y}}^{(1)} B_{\hat{x}}^{(0)} d\Omega \qquad \text{(A.13)} \\
O(\varepsilon^{(2)}) : F^{(2)} =& \int J_{\hat{x}}^{(0)} B_{\hat{y}}^{(2)} + J_{\hat{x}}^{(1)} B_{\hat{y}}^{(1)} + J_{\hat{x}}^{(2)} B_{\hat{y}}^{(0)} \\
&- J_{\hat{y}}^{(0)} B_{\hat{x}}^{(2)} - J_{\hat{y}}^{(1)} B_{\hat{x}}^{(1)} - J_{\hat{y}}^{(2)} B_{\hat{x}}^{(0)} d\Omega \\
=& \int J_{\hat{x}}^{(1)} B_{\hat{y}}^{(1)} - J_{\hat{y}}^{(1)} B_{\hat{x}}^{(1)} + J_{\hat{x}}^{(2)} B_{\hat{y}}^{(0)} - J_{\hat{y}}^{(2)} B_{\hat{x}}^{(0)} d\Omega.
\end{aligned}$$

The second eq. of A.13 reduces further to $F^{(1)} = 0$, since:

$$\iint J_y^{(1)} dxdy = 0 \text{ and } \iint J_x^{(1)} dxdy = 0 \text{ for } z = \text{ const}$$

because $\nabla \cdot \vec{J} = \partial_x J_x + \partial_y J_y + \partial_z J_z = 0$ (eq. 2.7)[1].

Thus, only the $F^{(2)}$ term contributes to the Lorentz force:

$$\begin{aligned}
F^{(2)} =& \int J_{\hat{x}}^{(1)} B_{\hat{y}}^{(1)} - J_{\hat{y}}^{(1)} B_{\hat{x}}^{(1)} + J_{\hat{x}}^{(2)} B_{\hat{y}}^{(0)} - J_{\hat{y}}^{(2)} B_{\hat{x}}^{(0)} d\Omega \\
=& \int J_{\hat{x}}^{(1)} B_{\hat{y}}^{(1)} - J_{\hat{y}}^{(1)} B_{\hat{x}}^{(1)} d\Omega + \int J_{\hat{x}}^{(2)} B_{\hat{y}}^{(0)} - J_{\hat{y}}^{(2)} B_{\hat{x}}^{(0)} d\Omega.
\end{aligned}$$

[1]The component of the current density can be replaced with the stream function Ψ. The integration is along a line with the same start and endpoint and thus is zero.

The stream function (eq. A.9) is inserted in the first integral on the right hand side:

$$\begin{aligned} F^{(2)a} &= \int J_{\hat{x}}^{(1)} B_{\hat{y}}^{(1)} - J_{\hat{y}}^{(1)} B_{\hat{x}}^{(1)} d\Omega \\ &= \int (\partial_{\hat{y}} \Psi) B_{\hat{y}}^{(1)} + (\partial_{\hat{x}} \Psi) B_{\hat{x}}^{(1)} d\Omega. \end{aligned} \tag{A.14}$$

The integrand is rearranged:

$$\begin{aligned} \partial_{\hat{x}}(\Psi B_{\hat{x}}^{(1)}) + \partial_{\hat{y}}(\Psi B_{\hat{y}}^{(1)}) &= B_{\hat{x}}^{(1)} \partial_{\hat{x}} \Psi + \Psi \partial_{\hat{x}} B_{\hat{x}}^{(1)} + B_{\hat{y}}^{(1)} \partial_{\hat{y}} \Psi + \Psi \partial_{\hat{y}} B_{\hat{y}}^{(1)} \\ \Rightarrow (\partial_{\hat{y}} \Psi) B_{\hat{y}}^{(1)} + (\partial_{\hat{x}} \Psi) B_{\hat{x}}^{(1)} &= \partial_{\hat{x}}(\Psi B_{\hat{x}}^{(1)}) + \partial_{\hat{y}}(\Psi B_{\hat{y}}^{(1)}) - \Psi \partial_{\hat{x}} B_{\hat{x}}^{(1)} - \Psi \partial_{\hat{y}} B_{\hat{y}}^{(1)}. \end{aligned}$$

Using eq. A.2:

$$\begin{aligned} F^{(2)a} &= \int (\partial_{\hat{y}} \Psi) B_{\hat{y}}^{(1)} + (\partial_{\hat{x}} \Psi) B_{\hat{x}}^{(1)} d\Omega \\ &= \int \partial_{\hat{x}}(\Psi B_{\hat{x}}^{(1)}) + \partial_{\hat{y}}(\Psi B_{\hat{y}}^{(1)}) - \Psi \partial_{\hat{x}} B_{\hat{x}}^{(1)} - \Psi \partial_{\hat{y}} B_{\hat{y}}^{(1)} d\Omega \\ &= \int \partial_{\hat{x}}(\Psi B_{\hat{x}}^{(1)}) + \partial_{\hat{y}}(\Psi B_{\hat{y}}^{(1)}) - \Psi (\partial_{\hat{x}} B_{\hat{y}}^{(1)} + \partial_{\hat{y}} B_{\hat{x}}^{(1)}) d\Omega \\ &= \int \partial_{\hat{x}}(\Psi B_{\hat{x}}^{(1)}) + \partial_{\hat{y}}(\Psi B_{\hat{y}}^{(1)}) + \Psi (\partial_{\hat{z}} B_{\hat{z}}^{(0)}) d\Omega. \end{aligned} \tag{A.15}$$

The integral of the first two terms can be considered as the z component of a curve. Then, Stokes' theorem can be applied on a plane $z = \text{const}$:

$$\int_{\Sigma} \nabla \times \vec{\mathcal{X}} \cdot d\Sigma = \oint_{\partial\Sigma} \vec{\mathcal{X}} \cdot d\vec{r}. \tag{A.16}$$

The right hand side of eq. A.16 can be rewritten:

$$\begin{aligned} \iint_{\Sigma} \nabla \times \vec{\mathcal{X}} \cdot d\Sigma &= \int_{\Sigma} \begin{pmatrix} \partial_x \\ \partial_y \\ \partial_z \end{pmatrix} \times \begin{pmatrix} \mathcal{X}_x \\ \mathcal{X}_y \\ \mathcal{X}_z \end{pmatrix} \cdot \begin{pmatrix} dydz \\ dzdx \\ dxdy \end{pmatrix} \\ &= \iint_{\Sigma} \begin{pmatrix} \partial_y \mathcal{X}_z - \partial_z \mathcal{X}_y \\ \partial_z \mathcal{X}_x - \partial_x \mathcal{X}_z \\ \partial_x \mathcal{X}_y - \partial_y \mathcal{X}_x \end{pmatrix} \cdot \begin{pmatrix} dydz \\ dzdx \\ dxdy \end{pmatrix} \\ &= \iint_{\Sigma, z=\text{const.}} \begin{pmatrix} \partial_y \mathcal{X}_z - \partial_z \mathcal{X}_y \\ \partial_z \mathcal{X}_x - \partial_x \mathcal{X}_z \\ \partial_x \mathcal{X}_y - \partial_y \mathcal{X}_x \end{pmatrix} \cdot \begin{pmatrix} 0 \\ 0 \\ dxdy \end{pmatrix} \\ &= \iint_{\Sigma} \partial_x \mathcal{X}_y - \partial_y \mathcal{X}_x dxdy. \end{aligned}$$

The left hand side of eq. A.16 can be rewritten:

$$\oint_{\partial\Sigma} \vec{\mathcal{X}} \cdot d\vec{r} = \oint_{\partial\Sigma} \begin{pmatrix} \mathcal{X}_x \\ \mathcal{X}_y \\ \mathcal{X}_z \end{pmatrix} \cdot \begin{pmatrix} dx \\ dy \\ dz \end{pmatrix} = \oint_{\partial\Sigma, z=\text{const.}} \begin{pmatrix} \mathcal{X}_x \\ \mathcal{X}_y \\ 0 \end{pmatrix} \cdot \begin{pmatrix} dx \\ dy \\ 0 \end{pmatrix} = \oint_{\partial\Sigma} \mathcal{X}_x dx + \mathcal{X}_y dy.$$

Thus, in the plane where $z = \text{const.}$ Stokes' theorem is:

$$\iint_\Sigma \partial_x \mathcal{X}_y - \partial_y \mathcal{X}_x dxdy = \oint_{\partial\Sigma} \mathcal{X}_x dx + \mathcal{X}_y dy.$$

For $\mathcal{X}_x = \Psi B_{\hat{x}}$ and $\mathcal{X}_y = \Psi B_{\hat{y}}$ follows:

$$\iint_\Sigma \partial_x(\Psi B_{\hat{y}}) - \partial_y(\Psi B_{\hat{x}})dxdy = \oint_{\partial\Sigma} \Psi B_{\hat{x}} dx + \Psi B_{\hat{y}} dy = 0$$

because $\partial\Sigma$ is the surface of the cylinder, where $\Psi = 0$.

The stream function Ψ (eq. A.15) is inserted into the third term on the right hand side of (eq. A.15):

$$\begin{aligned}
\int \Psi(\partial_{\hat{z}} B_{\hat{z}}^{(0)}) d\Omega &= \iiint \Psi(\partial_{\hat{z}} B_{\hat{z}}^{(0)}) dxdydz = \int \partial_{\hat{z}} B_{\hat{z}}^{(0)} (\iint \Psi dxdy) dz \\
&= \int \partial_{\hat{z}} B_{\hat{z}}^{(0)} (\iint \Psi r dr d\beta) dz = \int \partial_{\hat{z}} B_{\hat{z}}^{(0)} (\int_0^{2\pi} \int_0^1 \Psi R^2 \hat{r} d\hat{r} d\beta) dz \\
&= \int \partial_{\hat{z}} B_{\hat{z}}^{(0)} (R^2 \int_0^{2\pi} \int_0^1 \frac{\sigma v_{\hat{z}}}{4} (\hat{r}^2 - 1) \partial_{\hat{z}} B_{\hat{z}}^{(0)} \hat{r} d\hat{r} d\beta) dz \\
&= \int \partial_{\hat{z}} B_{\hat{z}}^{(0)} (\frac{\sigma v_{\hat{z}} R^2}{4} \partial_{\hat{z}} B_{\hat{z}}^{(0)} \int_0^1 \hat{r}^3 - \hat{r} d\hat{r} \int_0^{2\pi} d\beta) dz \\
&= \int \partial_{\hat{z}} B_{\hat{z}}^{(0)} (\frac{\sigma v_{\hat{z}} R^2}{4} \partial_{\hat{z}} B_{\hat{z}}^{(0)} (\frac{1}{4}\hat{r}^4 - \frac{1}{2}\hat{r}^2)\Big|_0^1 \beta\Big|_0^{2\pi}) dz \\
&= \int \partial_{\hat{z}} B_{\hat{z}}^{(0)} (\frac{\sigma v_{\hat{z}} R^2}{4} \partial_{\hat{z}} B_{\hat{z}}^{(0)} (\frac{1}{4} - \frac{1}{2}) 2\pi) dz \\
&= -\frac{\pi \sigma v_{\hat{z}} R^2}{8} \int (\partial_{\hat{z}} B_{\hat{z}}^{(0)})^2 dz.
\end{aligned}$$

Reinserting this into eq. (A.14) together with the rescaled coordinate $z = h\hat{z}$ leads to the first part of the integral for the force:

$$\begin{aligned}
F^{(2)a} &= \int J_{\hat{x}}^{(1)} B_{\hat{y}}^{(1)} - J_{\hat{y}}^{(1)} B_{\hat{x}}^{(1)} d\Omega \\
&= -\frac{\pi \sigma v_{\hat{z}} R^2}{8} \int (\partial_{\hat{z}} B_{\hat{z}}^{(0)})^2 dz \\
&= -\frac{\pi \sigma v_{\hat{z}} R^2 h}{8} \int_{-\infty}^{\infty} (\partial_{\hat{z}} B_{\hat{z}}^{(0)})^2 d\hat{z}.
\end{aligned} \tag{A.17}$$

For the second part on the right hand side of the force integral (eq. A.15) the x and y components of $\vec{J}$ are taken form (eq. A.11) and the differential is replaced with $d\Omega = r dr d\beta dz = R^2 h \hat{r} d\hat{r} d\hat{\beta} d\hat{z}$. The integrals not depending on $\hat{z}$ can be directly

calculated[2]:

$$
\begin{aligned}
F^{(2)b} =& \int J^{(2)}_{\hat{x}} B^{(0)}_{\hat{y}} - J^{(2)}_{\hat{y}} B^{(0)}_{\hat{x}} d\Omega \\
=& \int \sigma v_z \hat{r}^2 (\sin^2\beta \partial^2_{\hat{z}} B^{(0)}_{\hat{y}}(\hat{z}) + \sin\beta\cos\beta \partial^2_{\hat{z}} B^{(0)}_{\hat{x}}(\hat{z})) B^{(0)}_{\hat{y}} \\
&+ \sigma v_z \hat{r}^2 (\sin\beta\cos\beta \partial^2_{\hat{z}} B^{(0)}_{\hat{y}}(\hat{z}) + \cos^2\beta \partial^2_{\hat{z}} B^{(0)}_{\hat{x}}(\hat{z})) B^{(0)}_{\hat{x}} R^2 h \hat{r} d\hat{r} d\hat{\beta} d\hat{z} \\
=& \sigma v_z R^2 \int_{-\infty}^{+\infty} d\hat{z} h \int_{\phi=0}^{\phi=2\pi} d\hat{\beta} \int_{\hat{r}=0}^{\hat{r}=1} d\hat{r}\hat{r}^3 (\sin^2\beta \partial^2_{\hat{z}} B^{(0)}_{\hat{y}}(\hat{z}) + \sin\beta\cos\beta \partial^2_{\hat{z}} B^{(0)}_{\hat{x}}(\hat{z})) B^{(0)}_{\hat{y}} \\
&+ (\sin\beta\cos\beta \partial^2_{\hat{z}} B^{(0)}_{\hat{y}}(\hat{z}) + \cos^2\beta \partial^2_{\hat{z}} B^{(0)}_{\hat{x}}(\hat{z})) B^{(0)}_{\hat{x}} \\
=& \sigma v_z R^2 \pi \int_{-\infty}^{+\infty} d\hat{z} h \int_{\beta=0}^{\beta=2\pi} d\hat{\beta} \int_{\hat{r}=0}^{\hat{r}=1} d\hat{r}\hat{r}^3 (B^{(0)}_{\hat{y}} \partial^2_{\hat{z}} B^{(0)}_{\hat{y}}(\hat{z}) + B^{(0)}_{\hat{x}} \partial^2_{\hat{z}} B^{(0)}_{\hat{x}}(\hat{z})) \\
=& \frac{1}{4} \sigma v_z R^2 \pi h \int_{-\infty}^{+\infty} d\hat{z} (B^{(0)}_{\hat{y}} \partial^2_{\hat{z}} B^{(0)}_{\hat{y}}(\hat{z}) + B^{(0)}_{\hat{x}} \partial^2_{\hat{z}} B^{(0)}_{\hat{x}}(\hat{z})).
\end{aligned}
$$

The integrands may be rearranged for $i = \hat{x}, \hat{y}$:

$$
\begin{aligned}
\partial_{\hat{z}} (B^{(0)}_i \partial_{\hat{z}} B^{(0)}_i) &= \partial_{\hat{z}} B^{(0)}_i \partial_{\hat{z}} B^{(0)}_i + B^{(0)}_i \partial^2_{\hat{z}} B^{(0)}_i \\
\Rightarrow B^{(0)}_i \partial^2_{\hat{z}} B^{(0)}_i &= \partial_{\hat{z}} (B^{(0)}_i \partial_{\hat{z}} B^{(0)}_i) - (\partial_{\hat{z}} B^{(0)}_i)^2.
\end{aligned}
$$

The integral $\int_{-\infty}^{+\infty} d\hat{z} \partial_{\hat{z}} (B^{(0)}_i \partial_{\hat{z}} B^{(0)}_i) = 0$ on the boundaries. Then:

$$
F^{(2)b} = -\frac{1}{4} \sigma v_z R^2 \pi h \int_{-\infty}^{+\infty} d\hat{z} [(\partial_{\hat{z}} B^{(0)}_{\hat{x}})^2 + (\partial_{\hat{z}} B^{(0)}_{\hat{y}})^2]. \tag{A.18}
$$

Putting the two parts of the Lorentz force (eq. A.17) and eq. A.18 together delivers the analytic expression for the asymptotic dipole approximation:

$$
F^{(2)} = -\frac{\pi \sigma v_{\hat{z}} R^4}{8H} \int_{-\infty}^{+\infty} 2[(\partial_{\hat{z}} B^{(0)}_x)^2 + (\partial_{\hat{z}} B^{(0)}_y)^2] + (\partial_{\hat{z}} B^{(0)}_z)^2 d\hat{z}. \tag{A.19}
$$

[2] $\int_0^{2\pi} \sin^2\beta d\beta = \int_0^{2\pi} \cos^2\beta d\beta = \pi$, $\int_0^1 \hat{r}^3 d\hat{r} = 1/4$ and $\int_0^{2\pi} \sin\beta\cos\beta = 0$

Bibliography

[1] A. Alferenok, A. Pothérat, and U. Luedtke. Optimal magnet configurations for lorentz force velocimetry in low conductivity fluids. *Measurement Science and Technology*, 24(6):065303, 2013.

[2] T. Arens. *Mathematik*. Spektrum, Akad. Verl, Heidelberg, 2008.

[3] C. Audet. A survey on direct search methods for blackbox optimization and their applications. In P. M. Pardalos and T. M. Rassias, editors, *Mathematics Without Boundaries*, pages 31–56. Springer New York, 2014.

[4] C. Audet and J. E. Dennis. Mesh adaptive direct search algorithms for constrained optimization. *SIAM Journal of Optimization*, 17(1):188–217, jan 2006.

[5] R. C. Baker. Turbine flowmeters: II. theoretical and experimental published information. *Flow Measurement and Instrumentation*, 4(3):123–144, jan 1993.

[6] J. Banks. *Discrete-event system simulation*. Prentice Hall, Upper Saddle River, N.J. Singapore, 2010.

[7] J. Bladel. *Electromagnetic fields*. IEEE, Piscataway, N.J, 2007.

[8] T. Boeck, M. Zec, and A. Thess. Electromagnetic drag on a magnetic dipole caused by a translating and rotating conducting cylinder. *Journal of Engineering Mathematics*, 88(1):177–195, feb 2014.

[9] S. Brenner. *The mathematical theory of finite element methods*. Springer, New York, NY, 2008.

[10] COMSOL, Inc., Cambridge. *COMSOL Multiphysics Reference Guide version 5.0*, 2014.

[11] P. A. Davidson. *An introduction to magnetohydrodynamics*. Cambridge University Press, Cambridge New York, 2001.

[12] R. Ebert, S. Vasilyan, and A. Wiederhold. Flow velocimetry for weakly conducting electrolytes based on high resolution lorentzforce measurement. *International Journal of Modern Physics: Conference Series*, 24:1360015, jan 2013.

[13] G. Eichfelder, T. Gerlach, and S. Sumi. A modification of the alphabb method for box-constrained optimization and an application to inverse kinematics. *Preprint / Technische Universität Ilmenau, Institut für Mathematik*, 15-04, May 2015.

[14] A. Einstein. Zur Elektrodynamik bewegter Körper. *Annals of Physics*, 322(10):891–921, 1905.

[15] R. Fourer and D. Orban. Drampl: a meta solver for optimization problem analysis. *Computational Management Science*, 7(4):437–463, 2010.

[16] D. Friedrich, E. Mangano, and S. Brandani. Automatic estimation of kinetic and isotherm parameters from ZLC experiments. *Chemical Engineering Science*, 126:616–624, apr 2015.

[17] E. Gabriel, G. E. Fagg, G. Bosilca, T. Angskun, J. J. Dongarra, J. M. Squyres, V. Sahay, P. Kambadur, B. Barrett, A. Lumsdaine, R. H. Castain, D. J. Daniel, R. L. Graham, and T. S. Woodall. Open MPI: Goals, concept, and design of a next generation MPI implementation. In *Proceedings, 11th European PVM/MPI Users' Group Meeting*, pages 97–104, Budapest, Hungary, September 2004.

[18] F. Gao and L. Han. Implementing the nelder-mead simplex algorithm with adaptive parameters. *Computational Optimization and Applications*, 51(1):259–277, may 2010.

[19] C. Geiger. *Numerische Verfahren zur Lösung unrestringierter Optimierungsaufgaben*. Springer, Berlin, 1999.

[20] M. Gen. *Genetic algorithms and engineering optimization*. Wiley, New York, 2000.

[21] K. Halbach. Design of permanent multipole magnets with oriented rare earth cobalt material. *Nuclear Instruments and Methods*, 169(1):1–10, feb 1980.

[22] A. Henderson. *ParaView Guide, A Parallel Visualization Application*. Kitware Inc., 2007.

[23] R. Horst. *Introduction to global optimization*. Kluwer Academic Publishers, Dordrecht Boston, 2000.

[24] J. Jackson. *Klassische Elektrodynamik*. De Gruyter, Berlin u.a, 2002.

[25] G. W. C. Kaye. *Tables of physical and chemical constants and some mathematical functions*. London: Longmans, Green, 1911.

[26] M. Kirpo, S. Tympel, T. Boeck, D. Krasnov, and A. Thess. Electromagnetic drag on a magnetic dipole near a translating conducting bar. *Journal of Applied Physics*, 109(11):113921, 2011.

[27] T. G. Kolda, R. M. Lewis, and V. Torczon. Optimization by direct search: New perspectives on some classical and modern methods. *SIAM Review*, 45(3):385–482, jan 2003.

[28] Krohne. Flow measurement. Brochure, 2015.

[29] J. C. Lagarias, B. Poonen, and M. H. Wright. Convergence of the restricted nelder–mead algorithm in two dimensions. *SIAM Journal on Optimization*, 22(2):501–532, jan 2012.

[30] J. C. Lagarias, J. A. Reeds, M. H. Wright, and P. E. Wright. Convergence properties of the nelder-mead simplex method in low dimensions. *SIAM Journal of Optimization*, 9:112–147, 1998.

[31] S. Le Digabel. Algorithm 909: NOMAD: Nonlinear optimization with the MADS algorithm. *ACM Transactions on Mathematical Software*, 37(4):1–15, 2011.

[32] E. Lenz. *Über die Bestimmung der Richtung der durch elektrodynamische Vertheilung erregten galvanischen Ströme*. Number Bd. 107 in Annalen der Physik. Wiley-VCH, 1834.

[33] R. M. Lewis, V. Torczon, and M. W. Trosset. Direct search methods: then and now. *Journal of Computational and Applied Mathematics*, 124(1-2):191–207, dec 2000.

[34] H. A. Lorentz. La théorie électromagnétique de maxwell et son application aux corps mouvants. In *Collected Papers*, pages 164–343. Springer Science + Business Media, 1936.

[35] U. Lüdtke. *Numerische Simulation gekoppelter Felder in der Elektroprozesstechnik*. habilitation, Technische Universität Ilmenau, Fakultät für Elektrotechnik und Informationstechnik, 2014.

[36] M. A. Luersen and R. L. Riche. Globalized nelder–mead method for engineering optimization. *Computers & Structures*, 82(23-26):2251–2260, sep 2004.

[37] J. H. Mathews and K. K. Fink. *Numerical Methods Using Matlab (4th Edition)*. Pearson, 4 edition, 1 2004.

[38] MATLAB. *version 8.0.0.783 (R2012b)*. The MathWorks Inc., Natick, Massachusetts, 2012.

[39] K. I. M. McKinnon. Convergence of the nelder–mead simplex method to a nonstationary point. *SIAM Journal on Optimization*, 9(1):148–158, jan 1998.

[40] J. A. Nelder and R. Mead. A simplex method for function minimization. *The Computer Journal*, 7(4):308–313, jan 1965.

[41] I. Newton. *The Principia: mathematical principles of natural philosophy*. University of California Press, Berkeley, 1999.

[42] J. Nocedal and S. J. Wright. *Numerical optimization*. Springer, New York, 2006.

[43] J. Priede, D. Buchenau, and G. Gerbeth. Single-magnet rotary flowmeter for liquid metals. *Journal of Applied Physics*, 110(3):034512, 2011.

[44] S. Rao. *Engineering optimization theory and practice*. John Wiley & Sons, Hoboken, N.J, 2009.

[45] A. Ravindran. *Engineering optimization: methods and applications*. John Wiley & Sons, Hoboken, N.J, 2006.

[46] J. N. Reddy. *An introduction to the finite element method*. McGraw-Hill Higher Education, New York, NY, 2006.

[47] J. Reitz. *Foundations of electromagnetic theory*. Addison-Wesley Pub. Co, Reading, Mass, 1993.

[48] D. Rowe. *Thermoelectrics handbook: macro to nano*. CRC/Taylor & Francis, Boca Raton, 2006.

[49] V. Rudnev. *Handbook of induction heating*. Marcel Dekker, New York, 2003.

[50] Y. Saad. *Iterative methods for sparse linear systems*. The Society for Industrial and Applied Mathematics, Philadelphia, 2003.

[51] R. G. Sargent. Verification and validation of simulation models. In *Proceedings of the Winter Simulation Conference*, WSC '11, pages 183–198. Winter Simulation Conference, 2011.

[52] W. Schroeder. *The visualization toolkit: an object-oriented approach to 3D graphics*. Kitware, Clifton Park, N.Y, 2006.

[53] N. Sharma, N. Arun, and V. Ravi. An ant colony optimisation and nelder-mead simplex hybrid algorithm for training neural networks: an application to bankruptcy prediction in banks. *International Journal of Information and Decision Sciences*, 5(2):188, 2013.

[54] J. A. Shercliff. *The theory of electromagnetic flow-measurement*. Cambridge University Press, Cambridge Cambridgeshire New York, NY, USA, 1987.

[55] J. Snyman. *Practical mathematical optimization : an introduction to basic optimization theory and classical and new gradient-based algorithms*. Springer, New York, 2005.

[56] J. Sobieski. *Multidisciplinary design optimization supported by knowledge based engineering*. John Wiley & Sons, Ltd, Chichester, West Sussex, United Kingdom, 2015.

[57] D. Spitzer. *Industrial flow measurement*. ISA-The Instrumentation, Systems, and Automation Society, Raleigh, 2005.

[58] Y. Takeda. Velocity profile measurement by ultrasonic doppler method. *Experimental Thermal and Fluid Science*, 10(4):444–453, may 1995.

[59] A. Thess, E. V. Votyakov, B. Knaepen, and O. Zikanov. Theory of the lorentz force flowmeter. *New Journal of Physics*, 9(8):299, 2007.

[60] A. Thess, E. V. Votyakov, and Y. Kolesnikov. Lorentz force velocimetry. *Physical Review Letters*, 96(16), apr 2006.

[61] S. Tympel, D. Krasnov, T. Boeck, and J. Schumacher. Distortion of liquid metal flow in a square duct due to the influence of a magnetic point dipole. *Proceedings in Applied Mathematics and Mechanics*, 12(1):567–568, dec 2012.

[62] G. Venter. *Review of Optimization Techniques*. John Wiley & Sons, Ltd, 2010.

[63] Z. Watral, J. Jakubowski, and A. Michalski. Electromagnetic flow meters for open channels: Current state and development prospects. *Flow Measurement and Instrumentation*, 42:16–25, apr 2015.

[64] A. Wegfraß. *Experimentelle Untersuchungen zur Anwendbarkeit der Lorentzkraft-Anemometrie auf schwach leitfähige Fluide*. PhD thesis, TU Ilmenau, 2013.

[65] C. Weidermann, R. Klein, A. Thess, D. Lieftucht, and M. Reifferscheid. New technology for flow measurement of liquid steel in continuous casting. European Continuous Casting Conference, Graz, 2014.

[66] M. Weidner and B. Halbedel. High Tc superconducting bulk materials for the lorentz force velocimetry in low conducting and slow flowing fluids. In *Proceedings of the 13th Cryogenics*.

[67] W. Wiesel. *Modern astrodynamics*. Createspace, 2010.

[68] Wolfram Research, Inc. *Mathematica*. Wolfram Research, Inc., Champaign, Illinois, version 9 edition, 2012.

[69] O. C. Zienkiewicz. *The finite element method*. Elsevier/Butterworth-Heinemann, Oxford New York, 2005.

List of Figures

2.1 Working principle of Lorentz force velocimetry. Magnets create a primary magnetic field which acts on a moving electrically conducting fluid and gives rise to eddy currents. The interaction between magnetic field and eddy currents produce the Lorentz force, which breaks the fluid. An equal but opposite force pulls the magnets along the fluids direction. 6

2.2 xy plane of the dipole problem setup. The position of the dipoles $\vec{m}_i$ is fixed to a specific distance $\vec{H}_i$ in the $z = 0$ plane. The orientation of the magnetic moments are given by the spherical coordinates μ_i and ν_i. The magnetic field created by $\vec{m}_i$ at $\vec{r'}_i$ is expressed with eq. 4.1. 8

2.3 3D setup of the cylinder surrounded by a dipole. The cylinder domain Ω with boundary Γ and normal vector to the surface $\vec{n}$ moves with a velocity $\vec{v}$ and has an electrical conductivity σ. 8

3.1 Mesh of the model in PROMETHEUS for $\zeta_f = 1mm$ and $\zeta_c = 4mm$. 22

3.2 Comparison of analytic to numerical results of the Lorentz force for different grids (h=0.005R) in Prometheus. 22

3.3 Typical structure of a mesh used for numerical simulations in [8] with small distances between dipole and cylinder surface; a)cross-section view, b) top view. The cylinder axis is oriented along the x-axis, which differs in this work. 23

3.4 COMSOL mesh for the convergence study. The outer middle region is more sensitive because of its closeness to the dipole and needs to be meshed finer. 24

3.5 Convergence plot for mesh refinement study in COMSOL for one dipole for the close approximation. Second-order elements are used. . 25

4.1 Geometrical dimensions of the dipole problem setup with the sensitive region which is meshed finer to better resolve field gradients and cross section view of the xy plane. The position of the dipoles $\vec{m}_i$ is fixed to a specific distance $\vec{H}_i$ in the $z = 0$ plane. The orientation of the magnetic moments are given by the spherical coordinates μ_i and ν_i. The magnetic field created by $\vec{m}_i$ at $\vec{r'}_i$ is expressed with eq. 4.1. h is the distance of the dipole from the surface of the cylinder and H the distance from the dipole to the origin. The cylinder has the radius R, length l, conductivity σ and velocity $\vec{v}$ 29

4.2 Nondimensionalized Lorentz force as a function of the distance h between one dipole oriented in $|m|$ direction and the cylinder surface of a moving pipe. 29
4.3 Relative error ΔF between analytic results and numerical results from PROMETHEUS. 30

5.1 Generation of a new iterate x^* in the Nelder-Mead simplex direct search method with a 2D simplex: a) reflection, b) expansion, c) contraction based on [19]. 37

6.1 Lorentz force for one dipole depending on the azimuthal (μ_1) and polar (ν_1) angles of the orientation vector of the magnetic moment. . 44
6.2 Magnitude of the magnetic field inside the cross section of the cylinder directly underneath the dipole. The cylinder is divided vertically in the middle. The left hand shows the optimized magnetic field for $n = 1$ dipole and the right hand side the optimized magnetic field for $n = 4$ dipoles. 44
6.3 Lorentz force for two dipole depending on the azimuthal angles μ_1 and μ_2 of the orientation vector of the magnetic moments. 46
6.4 Depiction of the azimuthal angles μ_i and the resulting magnetic field (color and contour plots) in the xy cross section of the cylinder for the numerically optimized analytic problems. 49
6.5 Magnitude of the magnetic field inside the cross section of the cylinder directly underneath the dipole. The cylinder is divided vertically in the middle. It shows the optimized magnetic field for $n = 2$ dipoles for case 3 (left hand side) and case 2/case 1 (right hand side). The magnetic field reaching the cylinder is stronger when the dipoles cluster together in one position, than when the dipoles on opposite sides of the cylinder. 52
6.6 Best values of the nondimensionalized force $\mathcal{F}$ for the first 100 starting points for $n = 1$ dipole, optimized by: a) $fminunc$, b) $fmincon$, c) $fminsearch$. 53
6.7 Best values of the nondimensionalized force $\mathcal{F}$ for the first 100 starting points for $n = 2$ dipole, optimized by: a) $fmincon$, b) $fminsearch$, for case 3 (red) and case 1 (black). 54
6.8 Best values of the nondimensionalized force $\mathcal{F}$ for the first 100 starting points for $n = 3$ dipole, optimized by: a) $fmincon$, b) $fminsearch$, for case 3 (red) and case 1 (black). 55
6.9 Best values of the nondimensionalized force $\mathcal{F}$ for the first 100 starting points for $n = 4$ dipole, optimized by: a) $fmincon$, b) $fminsearch$. . 56
6.10 Best values of the nondimensionalized force $\mathcal{F}$ for the first 100 starting points for $n = 5$ dipole, optimized by: a) $fmincon$, b) $fminsearch$. . 57
6.11 Best values of the nondimensionalized force $\mathcal{F}$ for the first 100 starting points for $n = 6$ dipole, optimized by: a) $fmincon$, b) $fminsearch$. . 58

6.12 Best values of the nondimensionalized force $\mathcal{F}$ for the first 100 starting points for $n = 8$ dipole, optimized by: a) $fmincon$, b) $fminsearch$. . 59
6.13 Best values of the nondimensionalized force $\mathcal{F}$ for the first 100 starting points for $n = 16$ dipole, optimized by: a) $fmincon$, b) $fminsearch$. 60
6.14 Graphical depiction of the vector fields created by the optimized magnetic dipole moments for $n = 16$ dipoles indicated by the orange dots. One quarter of the cylinder was cut out. The color indicates the magnitude and the arrows point into the direction of a) the magnetic field, b) eddy currents and c) Lorentz force. 61
6.15 Azimuthal angles μ_i for the numerical optimization of the analytic problems for $n = 1, 2, ..., 16$ dipoles. μ_i is separated into position angle γ_i and deflection angle $\omega_i = \mu_i - \gamma_i$. 62
6.16 Convergence of the objective function in PROMETHEUS optimized by $fminsearch$ for a coarse (black) and fine (red) mesh for a) $n = 1$, b) $n = 2$, c) $n = 3$, d) $n = 4$, e) $n = 5$, f) $n = 6$, g) $n = 8$, h) $n = 16$. . 63
6.17 Best objective function values (nondimensionalized force $\mathcal{F}$) from the numerical optimization. 67
6.18 Geometric parameters of the multi dipole ring setups for 2 and 3 dipole rings. 68
6.19 Lorentz force depending on the distance s between the respective dipole rings: a) 2 dipole rings, b) 3 dipole rings with 8 dipoles in each ring. 69
6.20 Qualitative depiction of the symmetry among the dipole orientation angles. Filled out dots represent the respective μ_i and the thicker contours to ν_i. 71
6.21 Qualitative depiction of the symmetry among the dipole orientation angles. Filled out dots represent the respective μ_i and the thicker contours to ν_i. 72
6.22 Convergence plot of the 11 dipole rings problem optimized with the gradient-ascent method in PROMETHEUS. 73
6.23 Geometrical setup of the 11 dipole rings problem. The dipoles are indicated by the small cubes. 74
6.24 Optimized magnetic flux density in T of the 11 dipole rings problem. 74
6.25 Resulting eddy current density in A/m^2 of the 11 dipole rings problem. 75
6.26 Resulting Lorentz force density in N/m^3 of the 11 dipole rings problem. 75
6.27 Geometry of the setup with three successive magnet rings composed of eight individual segments (units in cm). 76
6.28 Optimization of the magnet system with the NOMAD algorithm. . . 77
6.29 2D plots of the magnetic field in $Tesla$ created by the optimized 3 magnet ring setup: a) cut through the xz plane and b) the zy plane. . 78
6.30 2D plots of the magnetic field in $Tesla$ created by the optimized 3 magnet ring setup: cut through the middle of the a) first ring, b) the second ring, c) the third ring. 79

6.31 2D plots of the eddy currents in A/m^2 created by the optimized 3 magnet ring setup: a) cut through the xz plane and b) the zy plane. . 80
6.32 2D plots of the eddy currents in A/m^2 created by the optimized 3 magnet ring setup: cut through the middle of the a) first ring, b) the second ring, c) the third ring. 81
6.33 Graphical depiction of the vector fields created by the optimized magnet system. One quarter of the cylinder was cut out. The color indicates the magnitude and the arrows point into the direction of a) the magnetic field, b) eddy currents and c) Lorentz force. 82

List of Tables

3.1 Summary of the physics interfaces of COMSOL Multiphysics, which are used for the simulations. 20
3.2 Parameters for the nonuniform meshes in PROMETHEUS. ζ_f, ζ_c are the numbers of mesh finesness. 21
3.3 Parameter study for the length of the cylinder. 23
3.4 Parameters for the grid in COMSOL for one dipole placed very close to the cylinder surface. 25

4.1 Lorentz force depending on the distance to the cylinder surface h. . . 31

5.1 Summary of the different κ_j values and the respective decision variables. The three κ_j represent optimization cases with varying degree of complexity for the analytic dipole formulation. γ_i is the angles of the positioning vector of each dipole and μ_i and ν_i are the polar and azimuthal angles of the magnetization vectors. 40

6.1 Summary of suitable MATLAB optimization algorithms. 47
6.2 Success rates of the algorithms $fminunc$, $fmincon$ and $fminsearch$. 50
6.3 Overview of the optimized polar angles μ_i and nondimensionalized force $\mathcal{F}$ of the analytic dipole problem for case 1. 51
6.4 Overview of the optimized polar angles μ_i and nondimensionalized force $\mathcal{F}$ of the numerical FEM dipole problems simulated with PROMETHEUS and optimized by the inbuilt gradient method. 64
6.5 Overview of the optimized polar angles μ_i and nondimensionalized force $\mathcal{F}$ of the numerical FEM dipole problems simulated with PROMETHEUS and optimized by $fminsearch$ from the MATLAB optimization toolbox [38]. 65
6.6 Overview of the best objective function values (nondimensionalized force $\mathcal{F}$) from the numerical optimization. 66

List of Symbols

$\vec{A}$ magnetic vector potential
$\vec{B}$ magnetic flux density
- B_n normal component
- B_t tangential component
- B_p primary
- B_s secondary
- B_i ith component
- B typical value of $\vec{B}$
- $\vec{B}^*$ nondimensional value of $\vec{B}$

$\mathcal{B}$ ball around x^b
c speed of light
$\vec{D}$ displacement field
$\vec{E}$ electric field
- E typical value of $\vec{E}$

$\vec{e_x}$, $\vec{e_y}$, $\vec{e_z}$ Cartesian unit vectors
$\vec{e_r}$ radial unit vector
$\vec{F}$ Lorentz force
- F_0 reference value
- $F = F_z$ component
- $\mathcal{F}$ nondimensionalized force

$f(x)$ objective function
$\vec{H}$ magnetizing field
- H_n normal component
- H_t tangential component

$\mathcal{H}$ hessian matrix
i, j counting variable
$\vec{J}$ current density
- J_s surface current

k dimension of decision variable space
l length
- L typical value of l

$\vec{m}$ magnetization vector
$\vec{n}$ normal vector on surface Γ
n number of dipoles in one dipole ring
o number of dipole rings
p_c search direction (gradient-ascent)
$\mathbb{R}$ set of real numbers
R cylinder radius
R_m magnetic Reynolds number
s distance between dipole rings
t time
- τ typical value of t
- t^* nondimensional value of t

T Temperature
$\vec{v}$ velocity
- v typical value of $\vec{v}$
- $\vec{v}^*$ nondimensional value of $\vec{v}$

x, y, z Cartesian coordinates
$\hat{x}$, $\hat{y}$, $\hat{z}$ rescaled Cartesian coordinates
x^0 starting point
x^c kth iterate
α_c step size (gradient-ascent)
Γ cylinder surface
$\gamma = \vec{v} \times \vec{B}$
$\epsilon_0 = 8.854 \cdot 10^{-12} F/m$ permittivity of free space
ϵ_r relative permittivity
$\varepsilon = R/H$ small parameter
ζ Prometheus meshing parameter
- ζ_f fine mesh
- ζ_c coarse mesh

$\eta = \mu_0 \sigma$ magnetic diffusivity
θ anlge belonging to $\vec{H}$
$\mu_0 = 4\pi \cdot 10^{-7} N/A^2$ permeability of free space
μ_r relative permeability
μ polar angle of $\vec{m}$
ν azumuthal angle of $\vec{m}$
ρ charge carrier
- ρ_s surface charges

σ electric conductivity

ϕ electric scalar potential
$\vec{\chi}$ arbitrary vector
Ψ stream function
ψ magnetic scalar potential
Ω cylinder domain
$\omega = \mu - \gamma$ deflection angle
$\partial/\partial x = \partial_x$ partial derivative with respect to x
$\nabla = (\partial_x, \partial_y, \partial_z)$ differential operator
∇_{2D} differential operator in 2D
∇_{cyl} differential operator in cylinder coordinates
∇^* nondimensional value of ∇
$\Delta = (\partial_x^2 + \partial_y^2 + \partial_z^2)$ Laplace operator